DOE/ET-0065/1

WIFFEN

Damage Analysis and Fundamental Studies

Quarterly Progress Report
January-March, 1978

August 1978

U.S. Department of Energy
Assistant Secretary for Energy Technology
Office of Fusion Energy

136 - Dual Beam on Fe-15Cr-20Ni
V-15Cr

Available from:

National Technical Information Service (NTIS)
U.S. Department of Commerce
5285 Port Royal Road
Springfield, Virginia 22161

Price: Printed copy: $10.75
Microfiche: $3.00

DOE/ ET-006511
UC-20, 20c

Damage Analysis and Fundamental Studies

Quarterly Progress Report
January-March 1978

August 1978

U.S. Department of Energy
Assistant Secretary for Energy Technology
Office of Fusion Energy
Washington, D.C. 20545

FOREWORD

This report is the first in a series of Quarterly Technical Progress Reports on "Damage Analysis and Fundamental Studies" (DAFS) which is one element of the Fusion Reactor Materials Program, conducted in support of the Magnetic Fusion Energy Program of the U. S. Department of Energy. Other elements of the Materials Program are:

- Alloy Development for Irradiation Performance (ADIP)
- Plasma-Materials Interaction (PMI)
- Special Purpose Materials (SPM)

The DAFS program element is a national effort composed of contributions from a number of National Laboratories and other government laboratories, universities, and industrial laboratories. It was organized by the Materials and Radiation Effects Branch, Office of Fusion Energy, DOE, and a Task Group on Damage Analysis and Fundamental Studies which operates under the auspices of that Branch. The purpose of this series of reports is to provide a working technical record of that effort for the use of the program participants, for the fusion energy program in general, and for the Department of Energy.

This report is organized along topical lines in parallel to a Program Plan of the same title (to be published) so that activities and accomplishments may be followed readily relative to that Program Plan. Thus, the work of a given laboratory may appear throughout the report. Chapters 1 and 2 report topics which are generic to all of the DAFS Program: DAFS Task Group Activities and Irradiation Test Facilities, respectively. Chapters 3, 4, and 5 report the work that is specific to each of the subtasks around which the program is structured: A. Environmental Characterization, B. Damage Production, and C. Damage Microstructure Evolution and Mechanical Behavior. The Table of Contents is annotated for the convenience of the reader.

This report has been compiled and edited under the guidance of the Chairman of the Task Group on Damage Analysis and Fundamental Studies, D. G. Doran, Hanford Engineering Development Laboratory, and his efforts, those of the supporting staff of HEDL and the many persons who made technical contributions are gratefully acknowledged. T. C. Reuther, Materials and Radiation Effects Branch, is the Department of Energy counterpart to the Task Group Chairman and has responsibility for the DAFS Program within DOE.

Klaus M. Zwilsky, Chief
Materials and Radiation
Effects Branch
Office of Fusion Energy

CONTENTS

	Page
Foreword	iii
Figures	xiii
Tables	xix
CHAPTER 1. DAFS TASK GROUP ACTIVITIES	1

Task Group activities have included review of environmental characterization plans for the Fusion Materials Irradiation Test Facility (FMIT), assessment of computer needs, and design of fission reactor irradiation experiments.

CHAPTER 2. IRRADIATION TEST FACILITIES	7

A national program is being developed for the utilization of RTNS-11 and other high energy neutron sources in the fusion materials program.

CHAPTER 3. SUBTASK A: ENVIRONMENTAL CHARACTERIZATION	13
1. Experiments Planned at ORR (ANL)	15

Experiments have been initiated to determine the spectra in the Oak Ridge Reactor (ORR) and to provide flux-spectral data for three planned MFE irradiations.

2. Helium Accumulation Fluence Dosimetry for Irradiations MFE-1 and MFE-2 at the Oak Ridge Research Reactor (AI)	22

Three sets of energy-dependent helium accumulation fluence monitors have been designed and prepared for incorporation in the MFE-1, MFE-2, and spectral characterization irradiations in the Oak Ridge Research Reactor.

CONTENTS (Cont'd)

Page

3. Inclusion of Self-shielding and Cadmium Cover Effects in SAND II (ANL) 29

Self-shielding and cadmium cover corrections, computed directly from ENDF/B-IV resonance data for wires and foils in both beam and isotropic flux geometries, have been included in SAND II.

4. Be(d,n) Irradiation at U.C. Davis, E_d = 30 MeV (ANL) 33

Results are presented for close-geometry irradiations at the University of California at Davis using Be(d,n) at E_d = 30 MeV. A complete error analysis is included. Positional dosimetry effects are seen to be severe.

5. Flux-Spectral Definition in FMIT (BNL) 39

The 3-D neutron transport code MORSE is being used to calculate the spatial. dependence of the neutron flux-spectrum in FMIT for application to damage analysis in insulators.

6. FMIT Damage Parameter Sensitivity Study (HEDL) 43

Initial results of a sensitivity study of the FMIT neutron field show little variation of the spectral-averaged damage energy cross section with position in the test region with flux > 10^{14} n/cm^2-s.

CONTENTS (Cont'd)

Page

7. Helium Generation Cross Section Results from the First AI RTNS-I Irradiation (AI) 58

Total heliwn production cross sections for 14.8-MeV neutrons have been determined experimentally for twelve pure elements and Type 316 stainless steel using the T(d,n) neutron spectrum of the RTNS-I facility.

8. Detailed Fluence Map for the Rotating Target Neutron Source (RTNS-I) (AI) 68

The use of heliwn accumulation fluence dosimetry for high-energy neutron irradiations has been clearly demonstrated in the detailed mapping of the RTNS-I fluence profile from *radiometric and helium accumulation dosimeter data.*

CHAPTER 4. SUBTASK B: DAMAGE PRODUCTION 79

1. Transport Theoretical Studies of Damage Production (ORNL) 82

Neutral particle transport codes are being applied to damage production descriptions. Studies are continuing of the reflection of hydrogen isotopes from solid surfaces using MARLOWE (recently improved and adapted to CDC hard-ware).

2. Computer Simulation of Replacement Sequences in Copper (HEDL, California State University, Northridge) 88

Results of computer simulations of <100>, <110>, and <111> replacement sequences in copper are presented for *six inter-atomic potentials. Comparisons of results from ADDES, a*

CONTENTS (Cont'd)

Page

quasi-dynamical code, and COMENT, a dynamical code, show excellent agreement. Upper limits on <100>, <110>, and <111> replacement sequences were found to be about 10, 30, and 14 replacements, respectively.

3. Displacement Functions for Multicomponent Systems (LASL, University of Alabama) 113

A computer code, DISPLCA, has been written to calculate displacement functions for multicomponent systems.

CHAPTER 5. SUBTASK C: DAMAGE MICROSTRUCTURE EVOLUTION AND MECHANICAL BEHAVIOR 119

1. DAFS Experiment in the ORR MFE-1 Test (HEDL, UCSB) 121

A test matrix was defined for the DAFS portion of the MFE-1 ORR irradiation.

2. The Effect of Irradiation on the Nucleation of Incoherent Si Precipitates in A1-Si Alloys (MIT) 128

A computer simulation has shown that irradiation has a profound effect on the nucleation of incoherent precipitates.

3. Microstructure of Irradiated Fusion Reactor First-Wall Materials (ANL) 136

The status of studies of the dose and temperature dependence of the microstructure of single and dual-ion irradiated Fe-20Ni-15Cr, V-15Cr, and selected Ti alloys is summarized.

CONTENTS (Cont'd)

4. Helium Mobility and Distribution (W-R&D) 159

Experiments characterizing helium distributions in ion-bombarded bcc metals using the elastic scattering of alpha particles are scheduled to start soon.

5. Microstructural Modeling (ANL) 161

The development of the low dose (≤ 1 dpa) microstructure in nickel has been calculated using a time-dependent nucleation and growth model that includes both interstitia.? and vacancy clustering.

6. Numerical Simulation of Void Nucleation in Irradiated Stainless Steel and Nimonic PE-16 (MIT) 165

A first principle calculation has given void number densities vs temperature which agree well with experiment in 316 SS and PE-16.

7. Light Ion and Fusion Neutron Damage Studies (PNL) 176

Sixteen MeV protons produced hardening in nickel that was equivalent, per particle, to that produced by 14 MeV neutrons; the protons produced 20% more hardening per particle in niobiwn. Cluster sizes are equivalent but cluster densities are larger for proton-irradiated material.

8. 14 MeV Neutron Damage (LLL) 187

The radiation-induced increases in the yield strengths of copper, vanadium, and niobium irradiated with 14.8 MeV

CONTENTS (Cont'd)

Page

neutrons are the same, per unit damage energy, as observed after irradiation with Be(30MeV d,n) neutrons. They are twice as great, per unit damage energy, as observed after irradiation in the Livermore Pool-Type Reactor (LPTR).

9. In-Situ HVEM Tensile Tests of Irradiated and Unirradiated Stainless Steel (UV) 204

In-situ HVEM tensile tests of unirradiated 316 stainless steel and EBR-11 irradiated 304 stainless steel, performed at room temperature and at 600°C, showed brittle failure of the irradiated material but no strong evidence of heliwn embrittted grain boundary cracking.

10. Light Particle Irradiations (W-R&D) 211

Scaling studies are being performed in uniaxial tensile specimens to determine the effects of specimen size, geometry, and microstructure on the stress-strain response.

11. Damage Coorelation (ANL) 213

The Torsional Creep Apparatus developed at HEDL is being installed at the ANL Cyclotron.

12. Effects of Irradiation and Irradiation Microstructure on Mechanical Behavior (ANL) 215

Preparations are under way for experiments on the effects of Cyclotron-injected helium on the mechanical behavior of Type 316 stainless steel.

CONTENTS (Cont'd)

13. **Dual-Ion Irradiations** (W-R&D) 217

Calibration experiments were completed and dual-ion irradiations of 20% cold-worked stainless steel were initiated.

FIGURES

CHAPTER 3 | Page

Be(d,n) Irradiation at U.C. Davis, E_d = 30 MeV

FIGURE 1. Positional Dosimetry Results for Be(d,n) Field at U.C. Davis 37

FIGURE 2. Unfolded Spectrum for ^{9}Be(d,n) at E_d = 30 MeV, 4mm from the Source. 38

FMIT Damage Parameter Sensitivity Study

FIGURE 1. Calculated FMIT Neutron Spectra for Deuteron Energies of 35 (- - - -), 30 (– - – -),and 15 (– – –) MeV, and a Beam Current of 0.1 amp, Compared with a 0-T Fusion Reactor First Wall Spectrum (———). 40

FIGURE 2. Flux Contour Maps for a Uniform Source Distribution. The Deuteron Energy is 35 MeV and the Beam Current Is 0.1 amp. The Irradiation Volumes within the Given Contours Are Listed. 49

FIGURE 3. Flux Versus Distance Normal to the Source Surface for Y-coordinates of 0.50 (-------), 2.50 (———), 4.50 (– - – -), and 5.50 (– – –) cm on an X-Y Plane with a Z-coordinate of 0.1 cm. 50

FIGURE 4. Flux Versus Distance Normal to the Source Surface for Y-coordinates of 0.50 (-------), 2.50 (———), 4.50 (– - – -), and 5.50 (– – –) cm on an X-Y Plane with a Z-coordinate of 0.5 cm. 51

FIGURE 5. Flux Versus Distance Normal to the Source Surface for Y-coordinates of 0.50 (-------), 2.50 (———), 4.50 (– - – -), and 5.50 (– – –) cm on an X-Y Plane with a Z-coordinate of 0.9 cm. 52

FIGURES

Page

CHAPTER 3 (Cont'd)

FIGURE 6. Positions within the Test Region at which Neutron Spectra Were Calculated. 53

FIGURE 7. Calculated Neutron Spectra at Positions 2(- — - —) and 10 (———) in the Test Region, as Shown in Figure 6. The Deuteron Energy Is 35 MeV, the Beam Current Is 0.1 amp, and the Mean neutron Energies Are 13.7 and 12.3 MeV, Respectively. 54

FIGURE 8. Percent Response Versus Neutron Energy for 35 (-------) and 15 (———) MeV Deuterons. 55

Detailed Fluence Map for the Rotating Target Neutron Source (RTNS-I)

FIGURE 1. Helium Generation Results and Neutron Fluence Calculations for Four Dosimetry Rings Irradiated in RTNS-I. 75

FIGURE 2. Contours of Constant Fluence for Mid-plane of Al Assembly Irradiated in RTNS-I (Units of 10^{17} n-cm^{-2}). 77

CHAPTER 4

Computer Simulation of Replacement Sequences in Copper

FIGURE 1. Plots of the Interatomic Potentials 738M (— —), 780M (———), and BM (- - -) Versus Interatomic Distance. 94

FIGURE 2. Plots of the Interatomic Potentials 738 M-E (— —), 780 M-E (———), and BM-J (- - -), and Their Corresponding Interatomic Forces, Versus Interatomic Distance. r_0 Is the Equilibrium Distance Between Nearest Neighbors in the Ideal Lattice and a Is Lattice Parameter. 97

FIGURE 3. Variation in Focusing Parameter With Energy for the 780M Potential Near the <100> Direction. The Symbols A, □, and ○ Refer to Data from PKA's Initiated at Angular Deviations from the <100> Direction of Less Than 2°, Between 2" and 4°, and Greater Than 4°, Respectively. 108

CHAPTER 5

Page

The Effect of Irradiation on the Nucleation of Incoherent Si Precipitates in Al-Si Alloys

FIGURE 1. The Steady State Nucleation Rate $J_s(m^{-3}s^{-1})$ for Si-A1 at 25 °C, as a Function of the Biasing Ratio β_i/β_v), and Solute and Vacancy Supersaturations. 131

Microstructure of Irradiated Fusion Reactor First-Wall Materials

FIGURE 1. Schematic of ANL Dual-Ion Irradiation System. 138

FIGURE 2. Temperature Dependence of Swelling and Cavity Size in FE-20Ni-15Cr (Dose Rate = 3×10^{-3} dpa $\cdot s^{-1}$). 139

FIGURE 3. Temperature Dependence of the Dislocation and Cavity Number Densities in Fe-20Ni-15Cr (Dose Rate = 3×10^{-3} dpa $\cdot s^{-1}$). 140

FIGURE 4. Dose Dependence of Cavity Size in Fe-20Ni-15Cr (Dose Rate = 3×10^{-3} dpa $\cdot s^{-1}$, Temperature = 700°C). 141

FIGURE 5. Dose Dependence of Cavity Number Density in Fe-20Ni-15Cr (Dose Rate = 3×10^{-3} dpa $\cdot s^{-1}$, Temperature = 700°C). 142

FIGURE 6. Dose Dependence of Dislocation Density in Fe-20Ni-15Cr (Dose Rate = 3×10^{-3} dpa $\cdot s^{-1}$, Temperature = 700°C).

FIGURE 7. Dose Dependence of Swelling in Fe-20Ni-15Cr (Dose Rate = 3×10^{-3} dpa $\cdot s^{-1}$, Temperature = 700°C). 145

FIGURE 8. Absorption Contrast Micrographs of V-15Cr Specimens Irradiated at 650°C to Different Dose Levels. (a) 5 dpa, (b) 11 dpa, (c) 27 dpa, and (d) 55 dpa. 147

FIGURE 9. Dislocation Contrast Micrographs of V-15Cr Specimens Irradiated at 650°C to Different Dose Levels. (a) 5 dpa, (b) 27 dpa, and (c) 55 dpa. 148

CHAPTER 5 (Cont'd)

Page

FIGURE 10. The Same Area of the 27-dpa Specimen Shown in Figure 2 Imaged Under Strong Dislocation Contrast (Upper Micrograph) and Absorption Contrast (Lower Micrograph). 149

FIGURE 11. Average Void Size Observed in V-15Cr as a Function of Total Dose. 150

FIGURE 12. Void Number Density and Calculated Total Swelling for V-15Cr as a Function of Total Dose. The Total Swelling of the Unalloyed V Stock Is Also Shown. 151

FIGURE 13. Cr Concentration vs Depth Profiles for an Unirradiated Control (0 dpa) and Two Irradiated Specimens (15 and 60 dpa Peak Dose). 153

Numerical Simulation of Void Nucleation in Irradiated Stainless Steel and Nimonic PE-16

FIGURE 1. Comparison of Measured and Calculated Void Number Densities in Type 316 SS. 170

FIGURE 2. Comparison of Measured and Calculated Void Number Densities in PE-16. 171

Light Ion and Fusion Neutron Damage Studies

FIGURE 1. Yield Strength Versus Particle Fluence for 16 MeV Proton and 14 MeV Neutron Irradiated Nickel. 178

FIGURE 2. Yield Strength Increase Versus Particle Fluence for 16 MeV Proton and 14 MeV Neutron Irradiated Niobium. 179

FIGURE 3. Yield Strength Increase Versus Damage Energy for 16 MeV Proton and 14 MeV Irradiated (a) Nickel, (b) Niobium. 180

FIGURE 4. Preliminary Results Showing Point Defect Cluster Density Versus Size for 16 MeV Proton and 14 MeV Neutron Irradiated Nickel. Curve C Is LL Data and D Is ORNL Data. 181

Page

CHAPTER 5 (Cont'd)

FIGURE 5. Ultimate Tensile Strength and Total Elongation Versus Particle Fluence for 16 MeV Proton and 14 MeV Neutron Irradiated Nickel. 183

FIGURE 6. Ultimate Tensile Strength and Total Elongation Versus Particle Fluence for 16 MeV Proton and 14 MeV Neutron Irradiated Niobium. 184

14 MeV Neutron Damage

FIGURE 1. Increase in 0.2%-Offset Yield Stress Vs. Neutron Fluence for RTNS, Be (D,n), and LPTR Irradiations of Copper. 191

FIGURE 2. Increase in 0.2%-Offset Yield Stress Vs. Neutron Fluence for RTNS, Be (D,n), and LPTR Irradiations of Niobium. 192

FIGURE 3. Increase in 0.2%-Offset Yield Stress Vs. Neutron Fluence for RTNS, Be (D,n) and LPTR Irradiations of Vanadium. 193

FIGURE 4. Increase in 0.2%-Offset Yield Stress Vs. Damage Energy for Neutron-Irradiated Copper. 194

FIGURE 5. Increase in 0.2%-Offset Yield Stress Vs. Damage Energy for Neutron-Irradiated Niobium. 196

In-Situ HVEM Tensile Tests of Irradiated and Unirradiated Stainless Steel

FIGURE 1. 400 kV Electron Micrograph of Unirradiated 316 SS Fractured at Room Temperature. 209

FIGURE 2. 400 kV Electron Micrograph of Neutron Irradiated 304 SS Fractured at 600 °C. 209

FIGURES (Cont'd)

Page

CHAPTER 5 (Cont'd)

Dual-Ion Irradiations

FIGURE 1. Schematic Depicting Sequence of Operations in Preparing 316 SS for Dual-Ion Bombardment. 230

FIGURE 2. Apparatus Designed for Copper Plating 316 SS/MO Target Assemblies to Obtain Optimum Thermal Contact Prior to Dual-Ion Bombardment. 231

FIGURE 3. Calibration Curves for Ion Milling of 316 SS and 304 SS Targets. 232

FIGURE 4. Calculated Damage Energy Profile for 28 MeV Si^{+6} Ions in 316 SS and Schematic Concentration Profiles for Implanted Helium and Silicon. 233

FIGURE 5. Proposed Scheme for a Residual Gas Analysis System Compatible with Dual-Ion Beam Bombardment Requirements. 234

TABLES

Page

CHAPTER 3

Experiments Planned at ORR

TABLE 1. Dosimetry Reactions for MFE Irradiations: Fluence Monitor Gradient Wires in 6061 Aluminum Tube 17

TABLE 2. Dosimetry Reactions for ORR Spectral Mapping: Wires and Foils in 6061 Aluminum Capsule 18

Helium Accumulation Fluence Dosimetry for Irradiations MFE-1 and MFE-2 at the Oak Ridge Research Reactor

TABLE 1. Helium Generation Dosimeters Provided by Atomics International for the ORR Low Power MFE Dosimetry Characterization Irradiation 23

TABLE 2. Helium Generation Dosimeters Provided by Atomics International for the Long-Term ORR Irradiation MFE-1 25

TABLE 3. Helium Generation Dosimeters Prepared by Atomics International for the Long-Term ORR Irradiation MFE-2 26

Be(d,n) Irradiation at U.C. Davis, E_d = 30MeV

TABLE 1. Flux Measurements for Styris 2(PNL) 35

FMIT Damage Parameter Sensitivity Study

TABLE 1. Spectral-Averaged Damage Energy Cross Sections for Copper 47

Helium Generation Cross Section Results from the First Al RTNS-I Irradiation

TABLE 1. Helium Concentrations in Pure Elemental Specimens from First RTNS-I Irradiation 59

TABLE 2. Concentrations of ^{4}He in Unirradiated and 3He in RTNS-I Irradiated Materials 61

TABLE 3. Helium Generation Cross Sections for 14.8-MeV Neutrons 63

TABLES (Cont'd)

Page

CHAPTER 3 (Cont'd)

Detailed Fluence Map for the Rotating Target Neutron Source (RTNS-I)

TABLE 1. Helium Concentrations in Copper Dosimetry Ring from the First RTNS-I Irradiation 70

TABLE 2. Helium Concentrations in Outer Aluminum Dosimetry Ring from the First RTNS-I Irradiation 71

TABLE 3. Helium Concentrations in Iron and Inner Aluminum Dosimetry Rings from the First RTNS-I Irradiation 72

CHAPTER 4

Computer Simulation of Replacement Sequences in Copper

TABLE 1. Potential Parameters 95

TABLE 2. Threshold Energies, E_T and Corresponding ADDES Parameter Settings, E_M, P_M, T_F 96

TABLE 3. ADDES Parameter Settings 100

TABLE 4. Replacement Sequence Characteristics from COMENT(C) and ADDES(A) Runs 102

TABLE 5. Maximum Replacement Sequence Lengths N_{max} as obtained with ADDES 106

TABLE 6. Average Focusing Energy $\hat{E}_F$(eV) as Obtained with ADOES 107

Displacement Functions for Multicomponent Systems

TABLE 1. Displacement Functions for Copper with E_d = 22eV 116

TABLE 2. Displacement Functions in Al_2O_3 for Aluminum Atoms Having Initial Energy E, $E_d(Al)$ = 40eV and $E_d(O)$ = 70eV 117

TABLE 3. Displacement Functions in Al_2O_3 for Oxygen Atoms Having Initial Energy E, $E_d(Al)$ = 40eV and $E_d(O)$ = 70eV 118

TABLES (Cont'd)

Page

CHAFTER 5

DAFS Experiment in the ORR MFE-1 Test

TABLE 1. DAFS MFE-1 Text Matrix 124

14 MeV Neutron Damage

TABLE 1. Chemical Analysis of Impurity Elements in Cominco Copper 189

TABLE 2. Chemical Analysis of Interstitial Impurities in Niobium and Vanadium 190

TABLE 3. Tensile Tests on Nb 200

TABLE 4. Tensile Tests on Nb-1%Zr 201

CHAPTER 1

DAFS TASK GROUP ACTIVITIES

I. PROGRAM

Title: Irradiation Effects Analysis
Principal Investigator: D. G. Doran
Affiliation: Hanford Engineering Development Laboratory

II. OBJECTIVE

The objective of this work is to coordinate the activities of the DAFS Task Group.

III. RELEVANT DAFS PROGRAM PLAN TASK/SUBTASK

All tasks

IV. SUMMARY

DAFS Task Group activities have included 1) a review of the initial plans for characterizing the neutron environment of the Fusion Materials Irradiation Test facility to be built at HEDL, 2) an assessment of computer needs, resulting in a request for 322 hours (equivalent CDC 7600) on the National MFE Computer Network, and 3) the development of test matrices for irradiations in the Oak Ridge Research Reactor.

V. ACCOMPLISHMENTS AND STATUS

The principal Task Group efforts during this reporting period were expended on completing the DAFS Program Plan and on participating in the Program Workshop for Materials and Radiation Effects Programs held at Germantown on January 18-20, 1978. Other activities, by Subtask Group, were as follows:

A. Subtask Group A - Environmental Characterization (L. R. Greenwood, ANL, Chairman)

The Fusion Materials Irradiation Test facility (FMIT), currently in an early design phase, is to be built at HEDL for operation beginning in 1983. The FMIT facility will use a 0.1 amp beam of deuterons of maximum energy 35 MeV striking a flowing lithium target to produce a high flux of high energy neutrons. In keeping with the scope of the DAFS Task Group, the FMIT project requested that the task group review the initial plans for characterizing the environment of FMIT. This was done at a meeting held at ANL on March 9-10, 1978. Attending were D. G. Doran (HEDL), H. Farrar, (AI), A. N. Goland (BNL), L. R. Greenwood (ANL - Chairman), R. R. Heinrich (ANL), D. M. Parkin (LASL), P. J. Persiani (ANL), T. C. Reuther (DOE), M. J. Saltmarsh (ORNL), A. B. Smith (ANL), and D. L. Smith (ANL). Not attending but also participating were N. D. Dudey (EXXON), M. L. Grossbeck (ORNL), G. R. Odette (UCSB), M. T. Robinson (ORNL), F. A. Smidt (DOE), and L. Stewart (LASL). The review focused on those issues that had an impact on the design.

B. Subtask Group B - Damage Production (M. T. Robinson, ORNL, Chairman)

Some programs under this subtask area, especially those engaged in atomistic modeling and Monte Carlo neutronic5 studies, are medium-to-heavy users of computers. An assessment of computer needs in the damage analysis community was carried out by the Subtask Group Chairman to aid in preparing a request for time on the National Magnetic Fusion Energy Computer Network. The estimates for FY 1979 totaled 322 equivalent CDC 7600 hours.

C. Subtask Group C - Damage Microstructure Evolution and Mechanical Behavior (Correlation Methodology) (G. R. Odette, UCSB, Chairman)

A concentrated effort by the Subtask Group Chairman, aided materially by HEDL metallurgists, resulted in the definition of a test matrix for inclusion in the first MFE DRR irradiation (MFE-1). More detail is given in a contribution to this report which references Tasks II.C.l and II.C.2.

Plans for a second DAFS irradiation test were formulated at a meeting in Chicago on January 18, 1978. Attendees were E. E. Bloom (ORNL), D. G. Doran (HEDL), F. Nolfi (ANL), K. Russell (MIT), J. A. Sprague (NRL), H. Wiedersich (ANL), W. Wolfer (UW), J. A. Spitznagel (West. R&D Ctr.), J. Swanks (ORNL), R. W. Powell (HEDL), and T. C. Reuther (DOE).

CHAPTER 2

IRRADIATION TEST FACILITIES

I. PROGRAM

Title: Irradiation Effects Analysis
Prinicipal Investigator: D. G. Doran
Affiliation: Hanford Engineering Development Laboratory

II. OBJECTIVE

Develop a national program plan for the effective utilization of the RTNS-II and other high energy neutron facilities.

III. RELEVANT DAFS PROGRAM PLAN TASK

All tasks are relevant in that the utilization of high energy neutron sources is an integral part of the DAFS Program strategy. The tasks expected to be affected most directly are:

TASK II.A.2 High Energy Neutron Dosimetry
II.A.4 Gas Generation Rates
II.A.5 Dosimetry Technique Development
11.6.3 Experimental Characterization of Primary Damage State
II.B.4 Damage Production in Insulators
II.C.l Effect of Material Parameters on Microstructure
II.C.2 Effect of Helium on Microstructure
II.C.3 Effect of Hydrogen on Microstructure
II.C.4 Effect of Solid Transmutation Products on Microstructure
II.C.6 Effect of Damage Rate and Cascade Structure on Microstructure
II.C.18 Relating Low and High Exposure Microstructures

IV. SUMMARY

A national program is being developed for the utilization of RTNS-II and other high energy neutron sources in the fusion materials program.

V. ACCOMPLISHMENTS AND STATUS

A. RTNS-II Utilization Plan - R. W. Powell and D. G. Doran

1. Introduction

Experiments have been performed by several laboratories over the past few years to assess the effects of high energy neutron irradiation on materials. The major facility for these studies has been the Rotating Target Neutron Source-I (RTNS-I) at the Lawrence Livermore Laboratory (LLL), which produces approximately 15 MeV neutrons from the D-T reaction. Cyclotrons at the Crocker Nuclear Laboratory of UC-Davis and at Oak Ridge National Laboratory have also been used to produce broad spectrum neutrons through the stripping of deuterons by a beryllium target. A new, higher flux facility, funded by the Office of Fusion Energy, is currently under construction at LLL. To be known as RTNS-II, full power operation is expected in January 1979. At the request of the Office of Fusion Energy, a program plan for the utilization of RTNS-II and other high energy sources is being prepared.

2. Status

The objective of the plan is the efficient utilization of the RTNS-II for fusion materials research. The plan describes the major problems facing the fusion materials program for which the RTNS-II and other high energy neutron facilities have relevance, the impact of past high energy neutron studies on these problems and the strategy proposed for utilizing the RTNS-II, in particular, to aid in solving these problems. Also included in the report is a compilation of other potential uses of this important national facility.

More than 120 individuals have been contacted either in person, by telephone or by questionnaire in an effort to poll the community on the effective use of the RTNS-II. Over *two* dozen completed questionnaires

have been returned to HEDL with projected uses ranging from mechanical properties studies to basic research in nuclear structure.

VI. REFERENCES

None.

VII. FUTURE WORK

A first draft of the plan is nearing completion. It will be distributed to the task groups for review during the next reporting period.

VIII. PUBLICATIONS

None.

CHAPTER 3

SUBTASK A: ENVIRONMENTAL CHARACTERIZATION

I. PROGRAM

Title: Dosimetry and Damage Analysis
Principal Investigator: L. R. Greenwood
Affiliation: Argonne National Laboratory

II. OBJECTIVE

The objective of this work is to measure the flux-spectrum at various locations in the Oak Ridge Reactor (ORR) and to provide dosimetry and damage analysis for MFE irradiation effects experiments.

III. RELEVANT DAFS PROGRAM PLAN TASK/SUBTASK

SUBTASK II.A.l.l Flux-spectral definition in a tailored fission reactor.

IV. SUMMARY

A major new effort has been initiated at ORR including three year-long irradiations for specimens from Argonne National Laboratory (ANL), Hanford Engineering Development Laboratory (HEDL), Oak Ridge National Laboratory (ORNL), and Naval Research Laboratory (NRL). A low power spectral study has also been planned. The dosimetry effort includes multiple foil activation materials and helium accumulation fluence monitors (HAFM) prepared by Atomics International (AI).

V. ACCOMPLISHMENTS AND STATUS

A. Experiments Planned at ORR -- L. R. Greenwood and R. R. Heinrich (ANL)

The Oak Ridge Reactor (ORR) has been designated as a primary DMFE irradiation facility. Consequently, we have undertaken a major new effort to characterize the neutron environment. Three year-long irradiations, designated ORR-MFE-I thru ORR-MFE-3, are planned for starts in February, June, and October of 1978, respectively. E. E. Bloom (ORNL) will coordinate the program which includes ANL, HEDL, ORNL, and NRL. We are responsible for dosimetry and damage analysis for each irradiation.

ORR-MFE-1, now being loaded in the reactor, will contain heaters to keep samples at temperatures up to 550°C. We placed four dosimetry wires, 24" in length, in each of the four quadrants of the irradiation assembly. The materials and expected reactions are listed in Table 1. In one quadrant we also loaded 107 helium accumulation fluence monitors (HAFM) prepared by H. Farrar IV (Atomics International). This will allow us to directly compare our He gas rate calculations with experiment for Be, Al, K, Si, Ti, Fe, Cu, Ni, and Pb.

Since we have not studied ORR previously and since the reactor has a mixed thermal/fast spectrum, we have also planned a low power (1.3 MW) spectral run. This will allow us to study reactions with short half-lives, to use cadmium covers to reduce the thermal flux on selected samples, and to use fission monitors with high heat generation rates. Two 24" long aluminum capsules were fabricated at ANL. One contained five spectral dosimetry sets and the other contained three sets. The contents of each set is listed in Table 2. The sets were separated by aluminum spacers. The capsule with five sets also contained 26 HAFM materials from Al including ^{10}B, ^{6}Li, Al, B, Li, and Ni. The capsules were leak checked and welded. Wires, as listed in Table 1, were placed in the two remaining quadrants of the dummy capsule.

TABLE 1

DOSIMETRY REACTIONS FOR MFE IRRADIATIONS: FLUENCE MONITOR GRADIENT WIRES IN 6061 ALUMINUM TUBE

Wire	Reaction	Half-life
Fe (10 mil)	$^{54}Fe(n,p)^{54}Mn$	312.5 D
	$^{54}Fe(n,\alpha)^{51}Cr$	27.7 D
	$^{58}Fe(n,\gamma)^{59}Fe$	44.7 D
Co-A1 (20 mil)*	$^{59}Co(n,\gamma)^{60}Co$	5.27 Y
	$^{59}Co(n,p)^{59}Fe$	44.7 D
	$^{59}Co(n,2n)^{58}Co$	70.85 D
Ni (10 mil)	$^{58}Ni(n,p)^{58}Co$	70.85 D
	$^{60}Ni(n,p)^{60}Co$	5.27 Y
Ti (10 mil)	$^{46}Ti(n,p)^{46}Sc$	88.9 D
	$^{47}Ti(n,p)^{47}Sc$	3.4 D
	$^{48}Ti(n,p)^{48}Sc$	1.8 D

HAFM materials from AI are also included

*NBS alloy, 0.116 wt. % cobalt

This low power spectral run will be conducted in the same reactor location as ORR-MFE-2 and the samples will be returned *to* ANL as soon as possible following irradiation *to* facilitate counting. The dummy capsule has been loaded at ORNL and is scheduled for irradiation in May of 1978.

VI. REFERENCES

None

VII. FUTURE WORK

Following the low power spectral run in May 1978 irradiated foils will be returned to ANL for gamma counting and HAFM materials will be

TABLE 2

DOSIMETRY REACTIONS FOR ORR SPECTRAL MAPPING: WIRES AND FOILS IN 6061 ALUMINUM CAPSULE

Material	Reaction	Half-life		Cadmium‡ Cover
$^{37}Np(n,f)$*	^{95}Zr	64.1	D	Yes
$^{235}U(n,f)$*	^{103}Ru	39.4	D	Yes
	^{131}I	8.0	D	
$^{238}U(n,f)$*	^{140}Ba	12.8	D	
^{238}U	$^{238}U(n,2n)^{237}U$	6.75	D	
	$(n,\gamma)^{239}Np$	2.36	D	Yes
Ni (wire)	$^{58}Ni(n,p)^{58}Co$	70.85	D	
	$(n,2n)^{57}Ni$	36	H	
Co (wire)	$^{59}Co(n,\gamma)^{60}Co$	5.27	Y	Yes
	$(n,p)^{59}Fe$	44.6	D	
	$(n,2n)^{58}Co$	70.85	D	
Fe (wire)	$^{54}Fe(n,p)^{54}Mn$	312.5	D	
	$(n,\alpha)^{51}Cr$	27.7	D	
	$^{58}Fe(n,\gamma)^{59}Fe$	44.6	D	
Au	$^{197}Au(n,y)^{198}Au$	2.7	D	Yes
	$(n,2n)^{196}Au$	6.1	D	
Ti	$^{46}Ti(n,p)^{46}Sc$	83.9	D	
	$^{47}Ti(n,p)^{47}Sc$	3.4	D	
	$^{48}Ti(n,p)^{48}Sc$	1.8	D	
sc*	$Sc(n,\gamma)^{46}Sc$	83.9	D	Yes
	$(n,2n)^{44m}Sc$	2.44	D	

HAFM materials from Al are also included

*In ORNL vanadium capsules

‡Yes means that both covered and uncovered samples were included

sent to AI for helium analysis. The SAND II code will be used to unfold the spectrum using detailed neutronics calculations from ORNL as input. Future work will depend on the agreement between the experiment and calculations. It is hoped that calculations can be validated so that the higher fluence measurements can be tied to calculated spectra in order to compute damage rates. Further fluence measurements are now being planned for ORR-MFE 2 and 3 and are expected to continue well into the future. Samples will be received and analyzed in 1979 and 1980.

I. PROGRAM

Title: Helium Generation in Fusion Reactor Materials

Principal Investigators: D. W. Kneff, H. Farrar IV

Affiliation: Rockwell International. Atomics International Division

II. OBJECTIVE

The objective of this work is to develop and apply helium accumulation fluence dosimetry to the measurement of neutron fluences and energy spectra in mixed-spectrum fission reactors utilized for fusion materials testing.

III. RELEVANT OAFS PROGRAM PLAN TASK/SUBTASK

TASK II.A.l	Fission Reactor Dosimetry
SUBTASK II.A.l.l	Flux-Spectral Definition in a Tailored Fission Reactor
SUBTASK II.A.1.2	Enhance Technique

IV. SUMMARY

Three sets of helium accumulation fluence monitors have been designed and prepared for inclusion as neutron dosimeters in three Magnetic Fusion Energy (MFE) irradiation experiments in the Oak Ridge Research Reactor (ORR). These sets include several different monitor materials with varying neutron energy sensitivities, and are intended both for development and for application of helium accumulation dosimetry in mixed-spectrum fission reactor neutron environments. Two of the sets have been included with Argonne National Laboratory (ANL) activation materials in the long-term ORR MFE-1 irradiation and in the short-term spectral characterization irradiation.

V. ACCOMPLISHMENTS AND STATUS

Helium Accumulation Fluence Dosimetry for Irradiations MFE-1 and MFE-2 at the Oak Ridge Research Reactor -- D. W. Kneff and H. Farrar IV (Atomics International)

Three sets of helium accumulation fluence monitors (HAFM's) were prepared during the report period for inclusion in the first and second MFE irradiations and in a short-term spectral characterization irradiation in ORR. These HAFM's will complement the ANL activation materials that constitute the primary dosimetry for these irradiations. The HAFM's were prepared with consideration both for providing dosimetry for these experiments, and for characterizing and evaluating various monitor materials for potential routine dosimetry use in future mixed-spectrum fission irradiations.

Each HAFM consists basically of a small quantity of crystalline, powder, or metal wire monitor material, sealed by electron-beam welding in a miniature (~1.3-mm diam, 6.4-mm long) vanadium capsule. The HAFM's are irradiated in the neutron environment of interest and subsequently analyzed in a high-sensitivity gas mass spectrometer to determine the total amount of helium generated by neutron interactions with the contained material. The several different materials being studied were chosen on the basis of their adequately-large energy-dependent reaction cross sections for helium generation in the energy ranges of interest. The differing energy sensitivities of these materials provide neutron energy-dependent fluence information that will be improved as the energy-dependent helium generation cross sections become better defined.

The helium accumulation materials prepared for the short-term low-power spectral characterization irradiation in ORR are listed in Table 1. In all the materials, the helium production is based on the two high (n,α) cross section isotopes ^{6}Li and ^{10}B, which are expected to generate enough

TABLE 1

HELIUM GENERATION DOSIMETERS PROVIDED BY ATOMICS INTERNATIONAL FOR THE ORR LOW POWER MFE DOSIMETRY CHARACTERIZATION IRRADIATION

Material	Number of Specimens	Form*	Reactions of Interest
LiF (natural)	3	Encapsulated crystal	$^{6}Li(n,\alpha)^{3}H$
Al-0.6% ^{6}Li	3	Unencapsulated wire	$^{6}Li(n,\alpha)^{3}H$
Al	3	Unencapsulated wire	background
B (natural)	3	Encapsulated crystal	$^{10}B(n,\alpha)7Li$
^{11}B	3	Encapsulated crystal	$^{10}B(n,\alpha)^{7}Li$ (^{10}B = 1.5%)
Ni-0.13% ^{10}B	2 3	Encapsulated alloy Unencapsulated wire	$^{10}B(n,\alpha)^{7}Li$
Ni	3	Unencapsulated wire	background
V	3	Empty V capsule	background

*The capsules are made of vanadium, electron-beam welded in vacuum.

helium for accurate measurement. This irradiation also included complete spectral sets of activation materials provided by Argonne National Laboratory.

The HAFM sets prepared for the long-term irradiations MFE-1 and FIFE-2 are listed in Tables 2 and 3, respectively, and consist primarily of developmental HAFM's encompassing a large range of energy sensitivities. In these two irradiations, the boron and ^{6}LiF HAFM's that have been developed for Breeder Reactor (BR) applications could not be used effectively because the ^{10}B or ^{6}Li would be burned up in the soft ORR neutron spectrum in the first few days. All three HAFM dosimetry sets included a few unencapsulated wire specimens with dimensions approximating the vanadium capsules.

The HAFM sets prepared for the MFE-1 and short-term irradiations were shipped to ANL, where they were loaded into the ANL dosimetry tubes. The HAFM set prepared for MFE-2 will also be shipped to ANL, as soon as the final irradiation geometry has been defined.

VII. FUTURE WORK

The irradiation of the ORR HAFM's will be followed by helium analysis in the high-sensitivity gas mass spectrometer at Atomics International. The results, which will complement the ANL activation dosimetry data, will be combined with data from irradiations of similar sets of materials in Breeder Reactor and Light Water Reactor (LWR) neutron spectra, to develop energy-dependent HAFM's for mixed-spectrum fission reactors.

VIII. PUBLICATIONS

1. H. Farrar IV (AI) and E. P. Lippincott (HEDL), "Helium Production Measurements for Neutron Dosimetry and Damaoe Correlations," Proc. Second ASTM-EURATOM Symposium on Reactor Dosimetry: Dosimetry Methods for Fuels, Cladding, and Structural Materials, W. C. Morgan, ed., Palo Alto, CA, October 1977.

TABLE 2

HELIUM GENERATION DOSIMETERS PROVIDED BY ATOMICS INTERNATIONAL FOR THE LONG-TERM ORR IRRADIATION MFE-1

Material	Number of Specimens	Form*	Energyt (MeV)	Primary Reactions of Interest
Ni	8 5	Encapsulated wire Unencapsulated wire	0	$^{58}Ni(n,\gamma)59Ni(n,\alpha)56Fe$
TiN	8	Encapsulated powder	1.3	$^{14}N(n,a)^{11}B$
Ti	6 5	Encapsulated wire Unencapsulated wire	-	for TiN$^{\pm}$
PbS	3	Encapsulated powder	1.5	$^{32}S(n,\alpha)29Si$
Be	6	Encapsulated crystals	2	$^{9}Be(n,\alpha)^{6}He$
KI	6	Encapsulated crystals	2.5	$^{39}K(n,\alpha)^{36}Cl$; for KCl$^{\pm}$
Si	6	Encapsulated crystals	2.7	$^{29}Si(n,\alpha)26Mg$; for $SiO_2^{\pm}$
^{54}Fe	3	Encapsulated chunks	3	$^{54}Fe(n,\alpha)51Cr$
Fe	6 5	Encapsulated wire Unencapsulated wire	3	$^{54}Fe(n,\alpha)51Cr$; for $FeF_2^{\pm}$
FeF_2	3	Encapsulated crystals	3	$^{19}F(n,\alpha)^{16}N$
KCl	4	Encapsulated crystals	3	$^{35}Cl(n,\alpha)^{32}P$; $^{39}K(n,\alpha)^{36}Cl$
SiO_2	6	Encapsulated powder	3.9	$^{16}O(n,\alpha)^{13}C$
cu	6 5	Encapsulated wire Unencapsulated wire	6	$^{63}Cu(n,\alpha)^{60}Co$
Al	6 5	Encapsulated wire Unencapsulated wire	6.5	$^{27}Al(n,\alpha)^{24}Na$
V	5	Empty V capsules	-	background

*The capsules were made of vanadium, electron-beam welded in vacuum.
†Approximate lower bound of neutron energy response.
*Several materials were included so that their helium contributions to the listed compounds could be measured.

TABLE 3

HELIUM GENERATION DOSIMETERS PREPARED BY ATOMICS INTERNATIONAL FOR THE LONG-TERM ORR IRRADIATION MFE-2

Material	Number of* Specimens	Form†	Energy‡ (MeV)	Primary Reactions of Interest
Ni	3 3	Encapsulated wire Unencapsulated wire	0	$^{58}Ni(n,\gamma)^{59}Ni(n,\alpha)^{56}Fe$
TiN	3	Encapsulated powder	1.3	$^{14}N(n,a)^{11}B$
Ti	3	Unencapsulated wire	-	background for TiN
PbS	3	Encapsulated powder	1.5	$^{32}S(n,\alpha)29Si$
KCl	3	Encapsulated crystals	2.5	$^{39}K(n,\alpha)^{36}Cl$; $^{35}Cl(n,\alpha)^{32}P$
CaF_2	6	Encapsulated crystals	2.7	$^{40}Ca(n,\alpha)37Ar$
Fe	3	Encapsulated wire	3	$^{54}Fe(n,\alpha)^{51}Cr$; background for FeF_2
FeF_2	3	Encapsulated crystals	3	$^{19}F(n,a)^{16}N$
V_2O_5	3	Encapsulated crystals	3.9	$^{16}O(n,\alpha)^{13}C$
Al	3	Encapsulated wire	6.5	$^{27}Al(n,\alpha)^{24}Na$
V	3 3	Empty capsule Unencapsulated wire	-	background
Nb	3	Unencapsulated wire	-	test as encapsulating material
Pt	3	Unencapsulated wire	-	test as encapsulating materia1

*Subject to change for compatibility with MFE-2 experiment design changes.

†The capsules were made of vanadium, electron-beam welded in vacuum.

*Approximate lower bound of neutron energy response.

2. A. Fabry (CEN/SCK), J. A. Grundl (NBS), W. N. McElroy (HEDL), E. P. Lippincott (HEDL), and H. Farrar IV (AI), "Status Report on Dosimetry Benchmark Neutron Field Development, Characterization and Application," Proc. Second ASTM Symposium on Reactor Dosimetry: Dosimetry Methods for Fuels, Cladding, and Structural Materials, W. C. Morgan, ed., Palo Alto, CA, October 1977.

I. PROGRAM

Title: Dosimetry and Damage Analysis
Principal Investigator: L. R. Greenwood
Affiliation: Argonne National Laboratory

II. OBJECTIVE

The objective of this work is to improve spectral unfolding techniques for fission reactor dosimetry, especially in tailored spectra such as the Oak Ridge Reactor (ORR).

III. RELEVANT DAFS PROGRAM PLAN TASK/SUBTASK

SUBTASK II.A.1.2 Enhance Technique

IV. SUMMARY

The SAND II spectrum unfolding code has been modified to include self-shielding and cadmium cover effects for foils and wires in both beam flux and isotropic flux geometries. Such effects may be very large and must be included in mixed-spectrum environments such as encountered in ORR.

V. ACCOMPLISHMENTS AND STATUS

A. Inclusion of Self-shielding and Cadmium Cover Effects in SAND II -- L. R. Greenwood (ANL)

The SAND II spectral unfolding code has been modified to include self-shielding and cadmium cover effects exactly. These corrections will be required at ORR and other mixed-spectrum facilities where resonance effects predominate. For example, in thin foils at least 50%

of the activation *of* $^{197}Au(n,\gamma)$ ^{198}Au is due to a single narrow resonance at 4.9 eV which has a peak cross section near 40,000 barns! However, thick foils (*e.g.*, ∿ 1 mil) will not fully indicate this effect since the neutrons near the resonance energy will be totally absorbed near the surface of the foils and will not penetrate to the inside atoms. This effect is called self-shielding and must be allowed for with all reactions which have high resonance or thermal cross-sections.

Unfortunately, self-shielding factors can not be determined unless one knows the spectrum which is being measured. This problem can be avoided by lumping the self-shielding and cadmium cover effects into the cross-sections used by SAND II. New self-shielding effects are then automatically calculated with each iteration.

A code RESATN has been written which corrects the SAND II cross-section library tor each case of self-shielding with or without cadmium cover by making very detailed calculations over each narrow resonance for each material. The calculations are based on formulas derived by K. M. Case, *et. al.*[1] Wires and foils can be used with either a beam or isotopic flux geometry. End effects are also considered to first order by replacing the actual foil thickness or wire diameter by the mean chord given by xyz/(xy + xz + yz) for a foil of length x, width y, and thickness z, or 2dl/(d + 21) for a wire of diameter d and length 1.

The code RESANTN is thus supplied with the types of materials, flux geometries, and mean chord dimensions. It then directly reads the ENDF/B-IV cross section tapes and computes corrected activation cross section factors. The SAND II program has been modified to read these correction factors and applies them to its cross-section library before any unfolding is attempted. Calculations appear to agree well with values in the literature[2] and are now being tested experimentally at ANL.

VI. REFEKENCES

1. K. M. Case, F. de Hoffmann, G. Placzek, Introduction to the Theory of Neutron Diffusion, Los Alamos Scientific Laboratory, 1953.

2. S. Pearlstein and E. V. Weinstock, Nuclear Science and Engineering 29, 28 (1967).

VII. FUTURE WORK

We plan to continue experimental tests of the calculated corrections for several reactions using the CP5 reactor at ANL and other facilities. Problems have been reported by other researchers for reactions with high elastic scattering cross sections on resonance such as $^{59}Co(n,\gamma)$. We thus plan to include scattering corrections in our code for these cases.

VIII. PUBLICATIONS

An ANL report is now being drafted.

I. PROGRAM

Title: Dosimetry and Damage Analysis
Principal Investigator: L. R. Greenwood
Affiliation: Argonne National Laboratory

II OBJECTIVE

The objective of this work is to develop dosimetry techniques and to provide routine dosimetry for DMFE experimenters using Be(d,n) irradiation facilities.

III. RELEVANT OAFS PROGRAM PLAN TASK/SUBTASK

SUBTASK II.A.2.1 Flux-spectral definition in Be(d,n) field

IV. SUMMARY

Dosimetry has been provided for experiments at the University of California at Davis Cyclotron using the $^{9}Be(d,n)$ reaction at E_d = 30 and 40 MeV. Results are presented for the irradiation of tensile specimens at E_d = 30 MeV placed only 4 mm from the neutron source. Positional effects are seen to be severe.

V. ACCOMPLISHMENTS AND STATUS

A. Be(d,n) Irradiation at U. C. Davis, E_d = 30 MeV - - L. R. Greenwood and R. R. Heinrich (ANL)

Dosimetry was provided for D. Styris (PNL) during May 1977 for the irradiation of tensile specimens (wires). Samples were placed immediately behind the beryllium target at an average distance of 4 mm from the source. The dosimetry package was placed immediately behind the

samples and consisted of 2" long by ¼" wide strips of Al, Fe, Ni, Co, Nb, In, and Au giving us thirteen independent reactions to monitor for spectral unfolding. Short-lived activities were counted at Lawrence Livermore Laboratory (LLL) and the others were counted at ANL. The dosimetry strips were cut into ten subsections in order to map flux and spectral gradients. The results for the four center cuts in the location of the tensile specimens are given in Table 1. A complete activity map for $^{93}Nb(n,2n)\ ^{92m}Nb$ is shown in Figure 1. (The highest four center points correspond to Table 1.) As can be seen, the gradients are very steep making accurate positional dosimetry a necessity.

An unfolded spectrum is shown for the small region of highest intensity in Figure 2. The top and bottom dashed curves indicate plus or minus one standard deviation limits in the unfolded flux. Errors are derived from the Monte Carlo code SANDANL using assumed errors in cross-sections, activation integrals, and starting spectrum. Error information' and starting spectra[2] were based on previous work in Be(d,n) fields. Integral errors in damage rates are much less than shown for the differential flux in various energy groups since covariance effects are very large. A complete covariance matrix is thus computed for the calculation of errors in damage rates. Relative errors are believed to be quite accurate, however absolute errors are somewhat uncertain since exact errors in cross-sections are not available.

VI. REFERENCES

1. L. R. Greenwood and R. R. Heinrich, Integral Testing of Neutron Activation Cross-Sections Using the $^{9}Be(d,n)$ Reaction at 14-16 MeV, Proceedings of tne Symposium on Neutron Cross-Sections from 10-40 MeV, BNL-NCS 50681, p. 391, July 1977.

2. D. R. Nethaway, R. A. Van Konynenburg, M. W. Guinan, and L. R. Greenwood, Neutron Spectra from 30-MeV Ueuterons on a Thick Beryllium Target, Proceedings of the Symposium on Neutron Cross-Sections from 10-40 MeV, BNL-NCS 50681, p. 135, July 1977.

TABLE 1

FLUX MEASUREMENTS FOR STYRIS 2 (PNL)
$^{9}Be(d,n)$ - E_d = 30 MeV
4 mm from source, current = 23.8 μA

Neutron Flux (x 10^{12} n/-cm^2-sec)

Sample Width (mm):	1.2		1.5		1.8		0.9	
Angular Range*:	-40° -28°		-28" -8°		-8° + 17"		+17° + 28"	
	Flux	± %	Flux	± %	Flux	± %	Flux	± %
Total Flux	5.23	13	5.77	11	6.37	12	5.40	12
< 1 MeV	0.48	30	0.48	38	0.61	34	0.52	45
> 1 MeV	4.75	12	5.29	9	5.76	11	4.88	9
> 4 MeV	3.36	5	4.01	5	4.27	5	3.79	6
>10 MeV	2.11	6	2.83	6	3.15	6	2.71	5
>14 MeV	1.47	9	1.90	9	2.06	9	1.78	8
>20 MeV	0.60	12	0.76	12	0.84	12	0.78	15
>25 MeV	0.23	62	0.28	49	0.31	46	0.31	51

*Estimated; t and - refer to degrees above or below the beam axis, respectively. The horizontal range covered was ±40° corresponding to wire sizes.

VII. FUTURE WORK

Two additional irradiations were conducted at E_d = 40 MeV in February 1978 and the data are now being analyzed. Errors are expected to be somewhat larger than in the present results since cross sections are less well-known at higher neutron energies. However, we have conducted integral cross section tests at the Oak Ridge Cyclotron at E_d = 40 MeV and expect to rely on these tests to guide the unfolding process.

VIII. PUBLICATIONS

L. R. Greenwood, R. R. Heinrich, R. J. Kennerley, and R. Medrzychowski, Development and Testing of Neutron Dosimetry Techniques for Accelerator Based Irradiation Facilities, Submitted to Nuclear Technology.

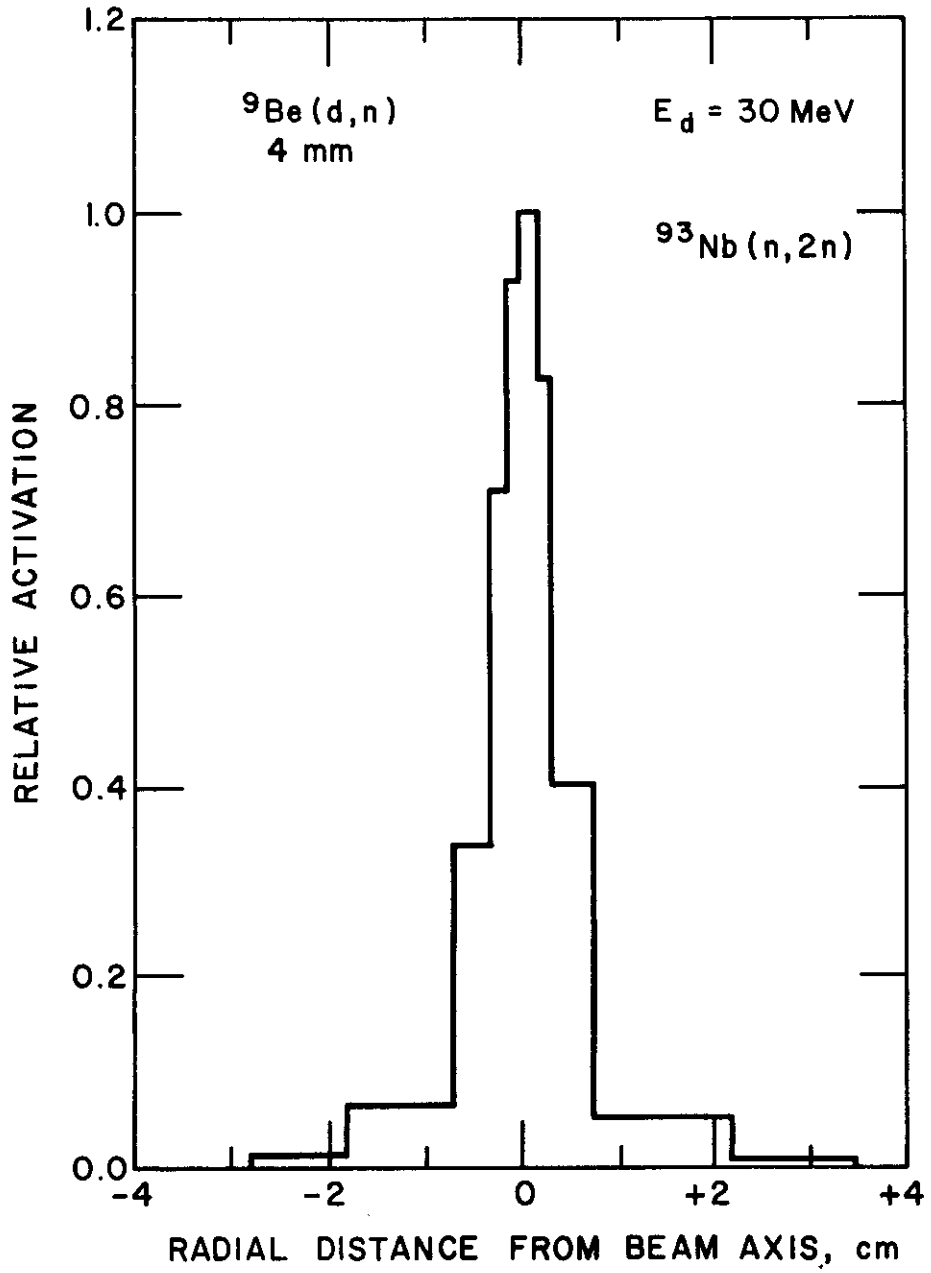

FIGURE 1. Positional Dosimetry Results for Be(d,n) Field at U.C. Davis.

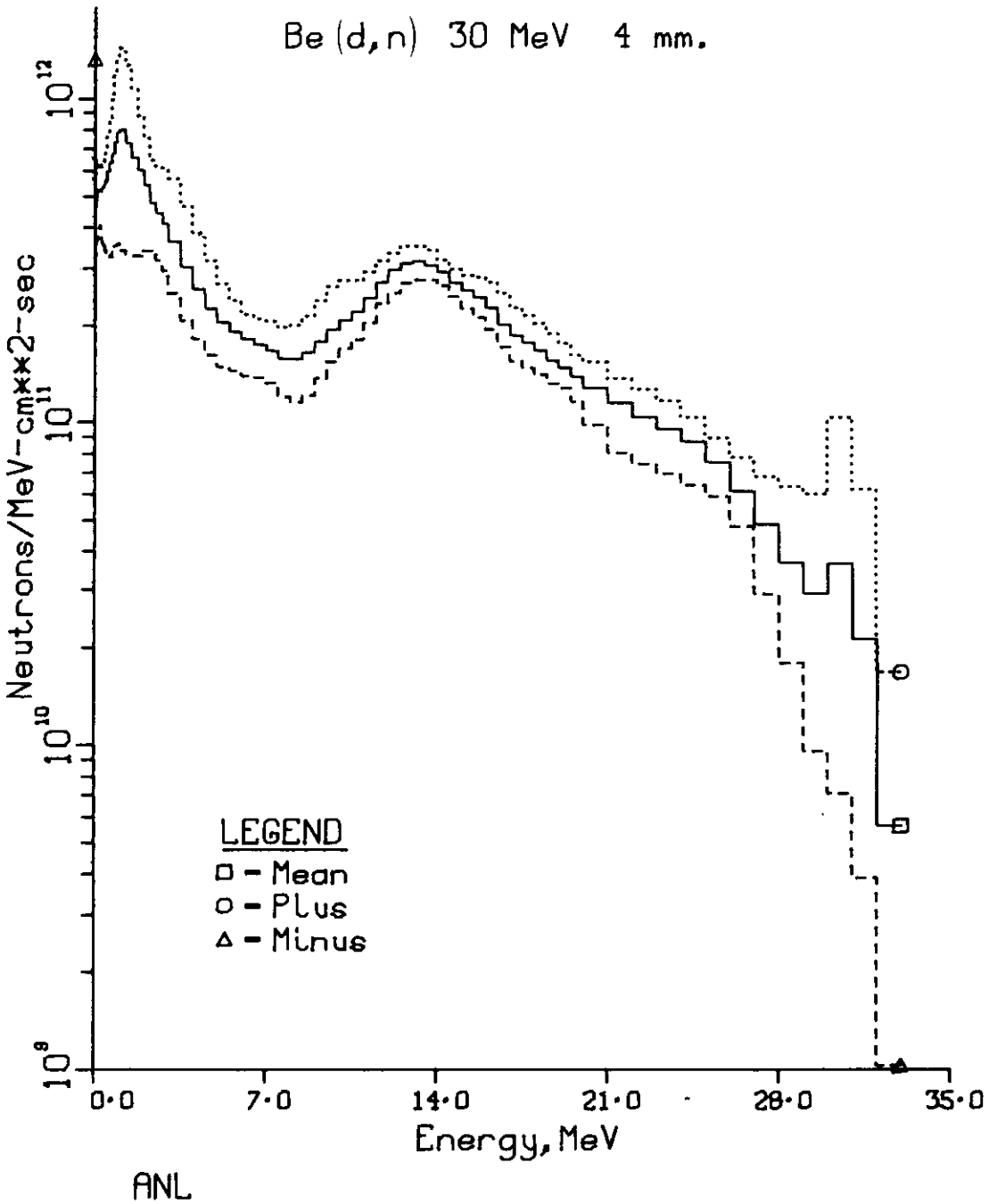

FIGURE 2. Unfolded Spectrum for $^{9}Be(d,n)$ at E_d = 30 MeV, 4mm from the Source. The Dashed Lines Indicate Plus and Minus One Standard Deviation Based on a Monte Carlo Error Analysis.

I. PROGRAM

Title: Damage Analysis and Dosimetry Radiation Damage Analysis
Principal Investigator: A. N. Goland
Affiliation: Erookhaven National Laboratory

II. OBJECTIVE

Radiation damage analysis studies associated with the use of electrical insulators in fusion reactors.

III. RELEVANT DAFS PROGRAM PLAN TASK/SUBTASK

SUETASK II.A.2.4 Flux Spectral Definition in FMIT

SUETASK II.B.1 Calculation of Displacement Cross Sections.

IV. SUMMARY

Analysis of possible radiation damage to insulators in critical regions of a fusion reactor will be emphasized. As the initial step in this task, the 3-D neutron transport code MORSE[1] (Multigroup Oak Ridge Stochastic Experiment) has been adapted for use on the BNL CDC-7600 computer.[**]) A subroutine based upon the stripping and evaporation models has been written to generate neutrons with energy and angular distributions consistent with experimental data from thick targets. Initial runs have been made toward determining the spatial dependence of the neutron flux spectrum in an irradiation cave.

V. ACCOMPLISHMENTS AND STATUS

As a first step in radiation damage studies leading to the identification of likely insulator candidate materials:

1. the 3-D neutron transport code, MORSE, has been adapted for use on the BNL CDC-7600 computer using large core memory,

2. a source routine for generating neutrons with energy and angular distributions consistent with experimental data[3] from thick targets has been written for use with MORSE,

3. a cross-section tape containing information for several nuclides of interest has been written in ANISN format from the ENDF/B data files, and

4. initial runs of MORSE to determine the spatial dependence of the neutron flux spectra inside an irradiation cave are in progress.

VI. REFERENCES

1. RSIC Computer Code' Collection: MORSE-CG, CCC-203A&B. Radiation Shielding Information Center, Oak Ridge National Laboratory, Oak Ridge, Tenn.

2. M. M. Ragheb and C. W. Maynard, "A Version of the MORSE Multigroup Transport Code for Fusion Reactor Blankets and Shields Studies", BNL-20376, August 30, 1975.

3. P. Grand and A. N. Goland, "An Intense Neutron Source Based Upon the Deuteron-Stripping Reaction", Nuclear Instruments and Methods, 145, p. 49 (1977).

VII. FUTURE WORK

The next steps in the task will include:

1. completion of the characterization of the neutron environment in an irradiation cave,

2. compilation of a cross-section file for neutron energies above 14 MeV,

3. reduction of the number of energy groups of the cross-section file to enable handling realistic problems,

4. formulation of a method of calculating meaningful damage parameters as they apply to insulators in the various regions of proposed prototype fusion reactors,

5. development of equivalent data for gamma rays in cases where ionizing radiation is expected to play an important role in the damage process, and

6. compilation of an appropriate neutron damage cross-section file for use as input to radiation effects calculation.

VIII. PUBLICATIONS

None.

I. PROGRAM

Title: Irradiation Effects Analysis
Principal Investigator: D. G. Doran
Affiliation: Hanford Engineering Development Laboratory

II OBJECTIVE

The objective of this work is to predict the spatial variations of radiation damage parameters within the test volume of the Fusion Materials Irradiation Test (FMIT) facility, and the sensitivity of these parameters to cross section and spectrum uncertainties.

III. RELEVANT DAFS PROGRAM PLAN TASK/SUBTASK

SUBTASK II.A.2.4 Flux Spectrum Definition In FMIT
SUBTASK II.B.1.5 Calculation of Displacement Cross Sections

IV. SUMMARY

Initial results indicate that for a uniform (1 x 10 cm) source there is little variation in the neutron spectrum throughout the test region where the flux is greater than 10^{14} n/cm^2 s. For each of the deuteron energies considered (15, 30, and 35 MeV), the spectral-averaged damage energy cross section for copper varies by less than 10% throughout the region; however, these cross sections decrease by as much as 40 percent in going from 35 to 15 MeV deuterons.

V. ACCOMPLISHMENTS AND STATUS

A. FMIT Damage Parameter Sensitivity Study - J. O. Schiffgens, R. L. Simons, and F. M. Mann.

1. Introduction

An integral part of the DAFS program strategy is the use of the FMIT facility to verify and caiibrate damage correlation models. It is as a damage analysis tool that the greatest demands will be placed on neutron field characterization. An initial step in this characterization is the determination of needed accuracies through studies of the spatial variation of damage parameters in the test region and the sensitivity of these parameters to cross section and spectrum uncertainties. This information is needed also in the development of appropriate experimental test assemblies Both characterization and test assembly needs must be reflected in the design of the facility.

A sensitivity study has begun using damage energy and helium production cross sections as the initial damage parameters of interest.

2. Initial Results

FMIT is to be an accelerator-based high energy neutron irradiation facility utilizing the d-Li breakup reaction to provide a high flux of neutrons $>10^{14}$ n/cm^2 s) within a reasonable test volume (>500 cm^3). The deuteron energy range is to be 15-35 MeV and the beam current 0.1 amp. Deuteron breakup is characterized by a neutron spectrum which is broadly distributed in energy compared with a fusion first wall spectrum. Fig. 1 shows several calculated FMIT neutron spectra'') compared with a d-T fusion reactor first wall spectrum.▼▼) The first wall flux-spectrum corresponds to a neutron wall loading of 1.25 MW/m^2. The FMIT flux-spectra correspond to the highest flux positions for deuteron energies of 35, 30, and 15 MeV, and a beam current of 0.1 amp. The FMIT spectra peak near neutron energies of 13, 11, and 6 MeV, respectively, showing that the facility has considerable spectrum flexibility with satisfactory total neutron fluxes.

In FMIT, neutrons will be produced as deuterons are slowed down in a lithium target. Since the neutron yield has not been measured for all deuteron energies and neutron emission angles of interest at this time, calculated spectra are being used in this study. The d-Li interaction model used in these calculations includes neutron stripping and compound nucleus formation.[3] The method described by Serber[3] is used to model the stripping process, while an evaporation model is used to treat compound nucleus formation. With cross sections derived from these models the neutron flux and spectrum is calculated throughout the test region behind the lithium target.

FMIT conceptual design calls for a flowing lithium target 2 cm thick backed by a 0.32 cm thick stainless steel plate. Although the source geometry is expected to be a parallelepiped 10 cm wide, 1 cm high, and R cm deep, where R is the deuteron range in lithium (1.4 cm for 35 MeV deuterons), the height of the beam is not treated explicitly at this time. For this study, the spatial distribution of deuterium ions striking the lithium is assumed to be either uniform or Gaussian along the width of the target with an edge intensity 1/100 that of the center. The neutron flux contour maps in Fig. 2 show, for the uniform source case, the dimensions and magnitude of the test volume within which the flux is greater than the stated amount.

The rate at which the test volume shrinks with increasing flux is demonstrated in Figs. 3, 4, and 5. These figures show plots of flux versus distance normal to the source surface for various y-coordinates on an x-y plane for which the z-coordinate is 0.1, 0.5, 0.9 cm, respectively. As shown in these figures, the flux in the x-direction changes fastest near the x-y midplane where the flux is highest.

Fig. 6 defines a test region, within the irradiation cell, by a coordinate system superposed on the source volume. Neutron spectra for deuteron energies of 35, 30, and 15 MeV have been calculated at the twelve positions shown. Fig. 8 shows the hardest and softest of these spectra for

35 MeV deuterons (positions 2 and 10 in Fig. 6). With these data, spectral averaged damage energy cross sections have been calculated using the copper damage energy cross section of Roberto and Robinson.[4] The mean neutron energies and corresponding averaged cross sections for each of the twelve positions shown in Fig. 6 are presented in Table 1. For each given deuteron energy, the spectral-averaged cross section varies by less than 10% throughout the specified region. However, the spectral averaged cross sections decrease by as much as 40 percent in going from 35 to 15 MeV deuterons. This decrease is further illustrated by the histograms presented in Fig. 8. These show the percent response, i.e., the percentage of the reactions which occur within a given neutron energy range, versus energy. Note that, for 35 MeV deuterons, 95 percent of the displacements are produced by neutrons with energies less than 31 MeV, while, for 15 MeV deuterons, 95 percent are produced by neutrons with energies less than 19 MeV. Similarly, for 35 MeV deuterons, 50 percent of the displacements occur in the neutron energy range 10 to 20 MeV, while the corresponding range for 15 MeV deuterons is 4 to 10 MeV.

VI. REFERENCES

1. For a discussion of the method employed in calculating these spectra see F. M. Mann, "Neutron Environment in d-Li Facilities," HEDL-SA-1464, 1978.

2. G. L. Kulcinski, ed., "A Wisconsin Toroidal Fusion Reactor Design," University of Wisconsin, 1, UWFDM 68, March 1974.

3. R. Serber, Phys. Rev., 72, pg. 1008 (1947).

4. J. B. Roberto and M. T. Robinson, J. Nucl. Mat., 61, p. 149 (1976).

VII. FUTURE WORK

Calculations to define the effect of data uncertainties for FMIT will be continued, including analyses of spectral-averaged helium production cross sections.

TABLE 1

SPECTRAL-AVERAGED DAMAGE ENERGY CROSS SECTIONS FOR COPPER

No.	x (cm)	y (cm)	z (cm)	E_d = 35 MeV ϕ (10^{+14}n/cm^{2}s)	$\bar{E}_n$ (MeV)	σ_{dam} (10^{+4}eV b)	E_d = 30 MeV ϕ (10^{+14}n/cm^{2}s)	$\bar{E}_n$ (MeV)	σ_{dam} (10^{+4}eV b)	E_d = 15 MeV ϕ (10^{+14}n/cm^{2}s)	$\bar{E}_n$ (MeV)	σ_{dam} (10^{+4}eV b)
1	0.0	0.0	0.0	17.40	13.6	27.0	9.97	11.6	24.6	1.71	6.39	17.1
2	0.0	3.5	0.0	17.70	13.7	27.2	9.87	11.7	24.7	1.59	6.42	17.1
3	6.0	0.0	0.0	2.34	13.2	26.5	1.63	11.5	24.4	.345	6.45	17.2
4	6.0	3.0	0.0	2.12	13.2	26.5	1.46	11.5	24.4	.302	6.45	17.2
5	6.0	6.0	0.0	.75	12.6	25.7	.562	11.0	23.7	.148	6.29	16.9
6	12.0	0.0	0.0	1.07	13.3	26.6	.745	11.6	24.5	.153	6.51	17.3
7	12.0	5.0	0.0	.65	13.1	26.3	.642	11.4	24.3	.104	6.43	17.2
8	6.0	0.0	2.0	1.19	12.5	25.6	.900	11.0	23.7	.242	6.31	16.9
9	6.0	3.0	2.0	1.04	12.6	25.6	.784	11.0	23.7	.211	6.31	16.9
10	6.0	6.0	2.0	.51	12.3	25.2	.397	10.8	23.3	.117	6.20	16.7
11	12.0	0.0	2.5	.68	12.9	26.0	.500	11.3	24.0	.121	6.41	17.1
12	12.0	5.0	2.5	.44	12.7	25.8	.330	11.1	23.9	.0851	6.34	17.0

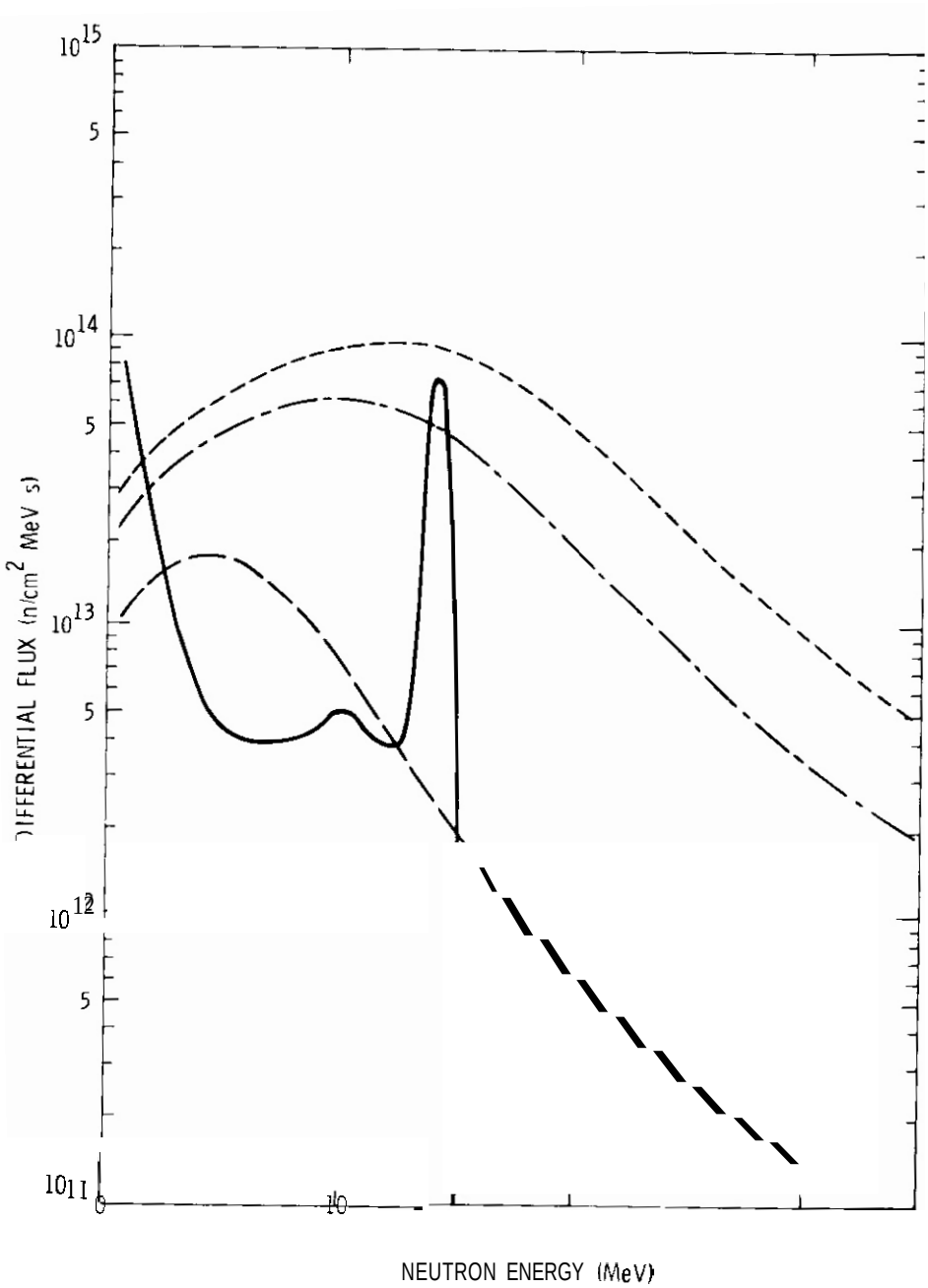

HEDL 7804-242.3

FIGURE 1. Calculated FMIT Neutron Spectra for Deuteron Energies of 35 (- - - -), 30 (— - — -), and 15 (— — —) MeV, and a Beam Current of 0.1 amp, Compared with a D-T Fusion Reactor First Wall Spectrum (———).

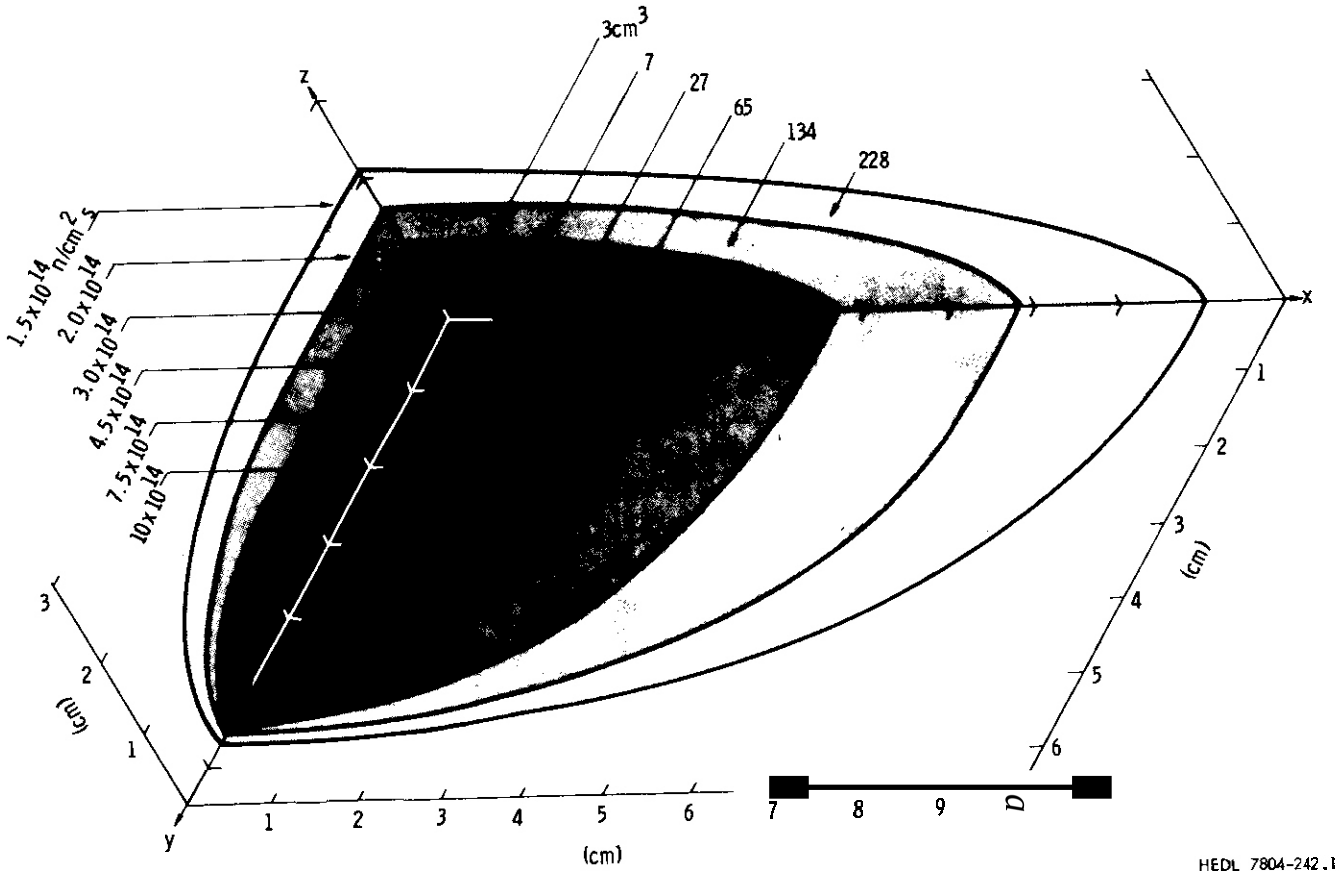

FIGURE 2 Flux Contour Maps for a Uniform Source Distribution. The Deuteron Energy is 35 MeV and the Beam Current Is 0.1 amp. The Irradiation Volumes within the Given Contours are Listed.

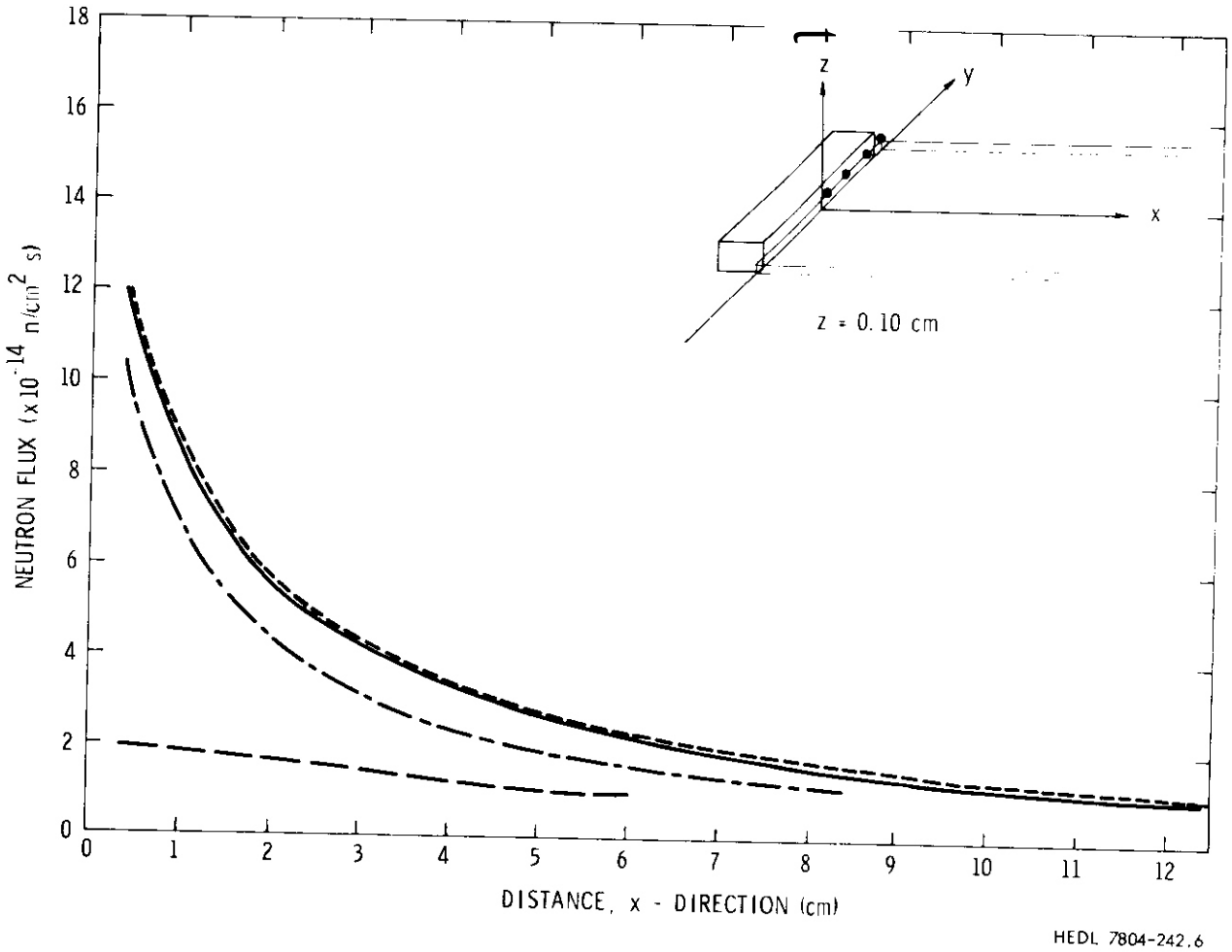

FIGURE 3 Flux Versus Distance Normal to the Source Surface for Y-Coordinates of 0.50 (-------), 2.50 (———), 4.50 (– - – -), and 5.50 (— — —) cm on an X-Y Plane with a Z-Coordinate of 0.1 cm.

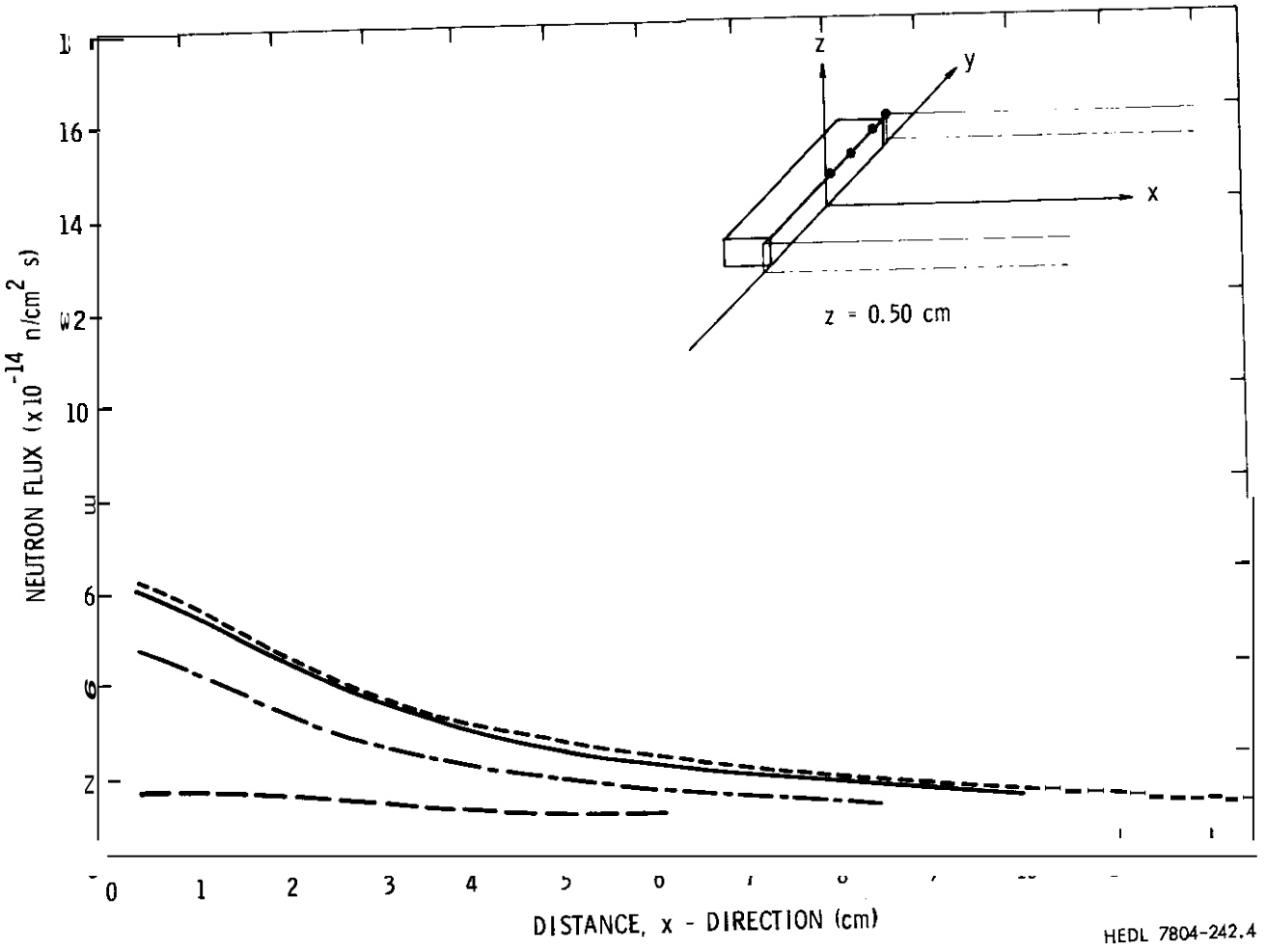

FIGURE 4. Flux Versus Distance Normal to the Source Surface for Y-Coordinates of 0.50 (-------), 2.50 (————), 4.50 (– - – -), and 5.50 (— — —) cm on an X-Y Plane with a Z-Coordinate of 0.5 cm.

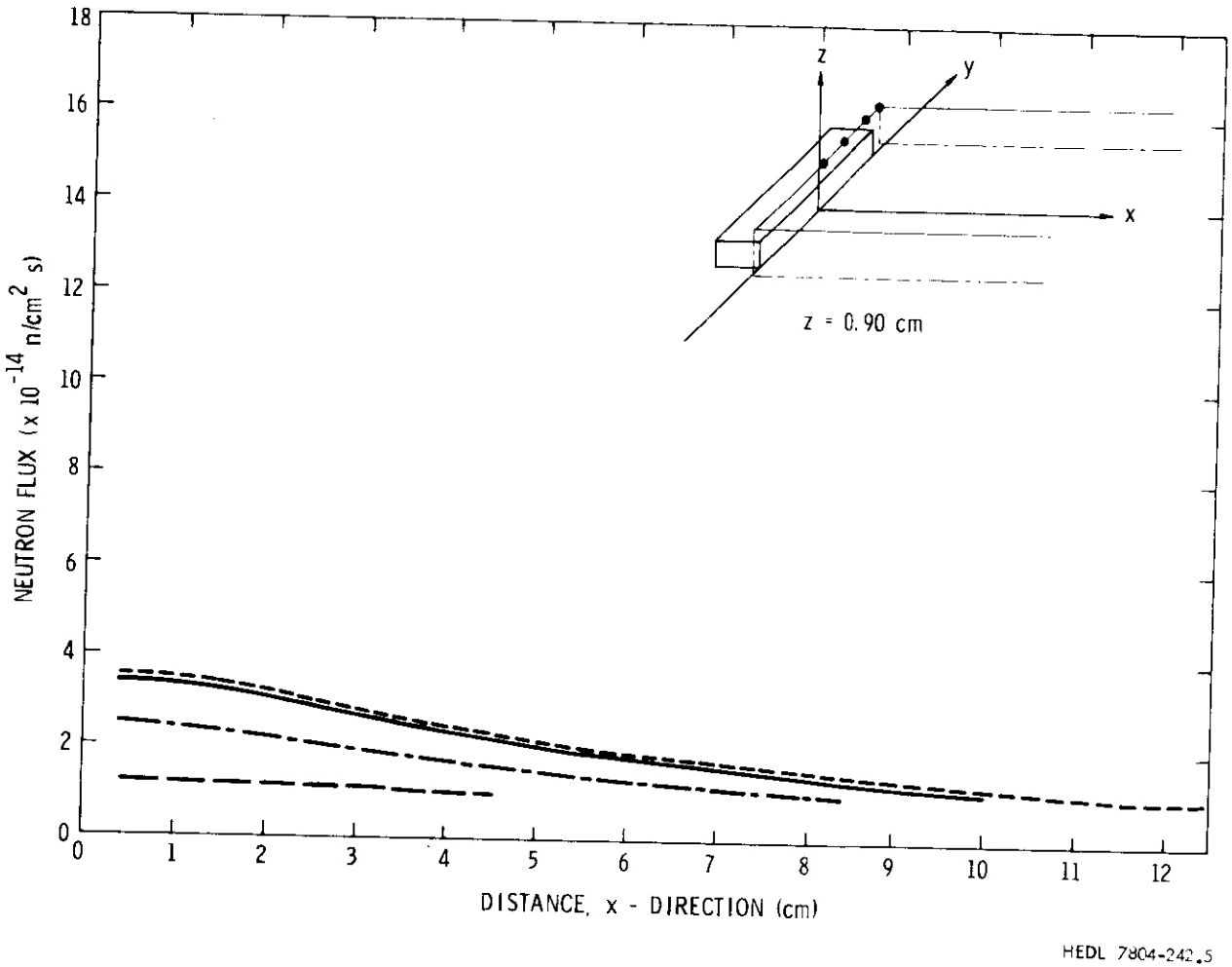

HEDL 7804-242.5

FIGURE 5. Flux Versus Distance Normal to the Source Surface for Y-Coordinates of 0.50 (-------), 2.50 (————), 4.50 (— - — -I, and 5.50 (— — —) cm on an X-Y Plane with a Z-Coordinate of 0.9 cm.

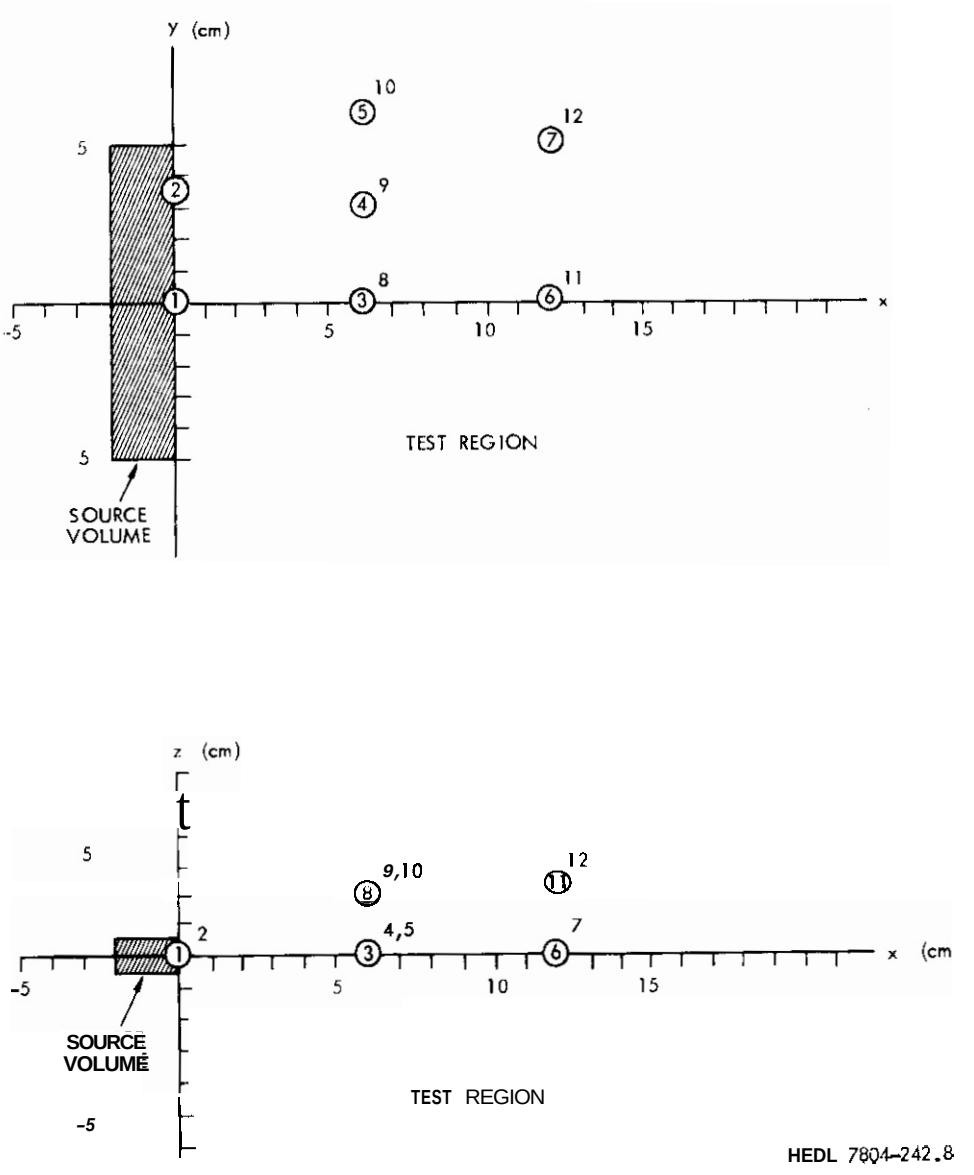

FIGURE 6. Positions within the Test Region at which Neutron Spectra Were Calculated.

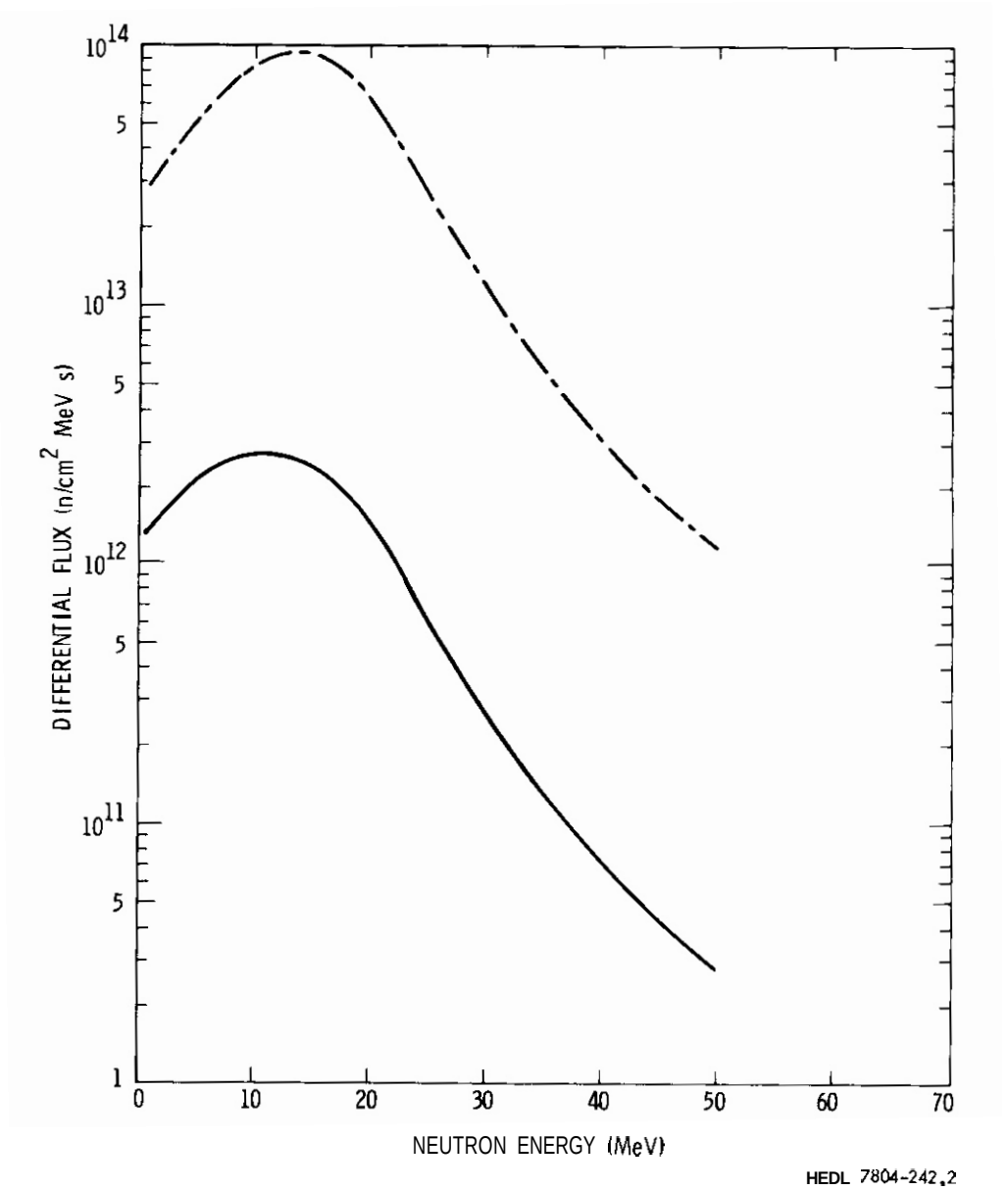

FIGURE 7. Calculated Neutron Spectra at Positions 2(— - — -) and 10 (———) in the Test Region, As Shown in Figure 6. The Deuteron Energy-Is 35 MeV, The Beam Current Is 0.1 amp, and the Mean Neutron Energies Are 13.7 and 12.3 MeV, Respectively.

I. PROGRAM

Title: Helium Generation in Fusion Reactor Materials

Principal Investigators: D. W. Kneff, H. Farrar IV

Affiliation: Rockwell International, Atomics International Division

II. OBJECTIVE

The objective of this work is to measure helium generation rates of materials for Magnetic Fusion Reactor applications in a 14.8-MeV T(d,n) neutron environment.

III. RELEVANT DAFS PROGRAM PLAN TASK/SUBTASK

SUBTASK II.A.4.2 T(d,n) Helium Gas Production Data

IV. SUMMARY

The total helium generation cross sections of twelve pure elements and Type 316 stainless steel have been determined experimentally for the 14.8- MeV neutron environment of the Rotating Target Neutron Source (RTNS-I) at Lawrence Livermore Laboratory (LLL). The results were obtained by measuring the total helium production in irradiated specimens using Atomics International's high-sensitivity gas mass spectrometer, and determining the neutron fluence received by each specimen from a fluence map constructed from radiometric foil and helium accumulation dosimetry information.

The results show that 80% of the helium generated in Type 316 stainless steel can be accounted for by the four elements Fe, Ni, C, and Mo.

V. ACCOMPLISHMENTS AND STATUS

Helium Generation Cross Section Results from the First AI RTNS-I Irradiation -- H. Farrar IV and D. W. Kneff (Atomics International)

A. Introduction

The Atomics International (AI) program to measure helium generation cross sections of materials of Magnetic Fusion Reactor (MFR) interest in high-energy neutron environments is based on irradiating those materials in an appropriate neutron field, and subsequently analyzing them for total helium by high-sensitivity gas mass spectrometry. The results are combined with the neutron fluence received by each sample to determine the total helium generation cross sections. The specific fluence information is derived from the same experiment by mapping radiometric foil fluence dosimetry information and relative helium generation concentrations in helium accumulation wires over the irradiation volume.

During this report period the final helium analyses have been completed for all materials irradiated in the first AI RTNS-I irradiation. These materials include twelve pure elements and Type 316 stainless steel. The geometry of the experiment has been described in detail elsewhere,[1] and is summarized briefly in the description of the final RTNS-I fluence map for this irradiation (Subtask II.A.5.1 of this report). This map was used to deduce the helium generation cross sections from the present helium analysis data.

B. Helium Generation Analysis Results

The results for the helium concentration analyses of the materials irradiated in this experiment are given in Tables 1 and 2. These tables omit the 59 segments comprising the four Al, Cu, and Fe helium accumulation fluence dosimetry wire rings, as those results are presented

TABLE 1

HELIUM CONCENTRATIONS IN PURE ELEMENTAL SPECIMENS
FROM FIRST RTNS-I IRRADIATION**

Element	Specimen	Mass After Etching (mg)	Number of 4He Atoms Released	^{4}He Concentration (appb)
C	EC-1	2.3813	1.886×10^{13}	158.0
	EC-3	1.0577	8.240×10^{12}	155.37
Ti	ETi-1	2.1165*	2.048×10^{11}	7.697
	ETi-2	1.6807*	1.610×10^{11}	7.616
	ETi-3A	1.6806*	1.539×10^{11}	7.285
	ETi-36	1.3799*	1.199×10^{11}	6.910†
V	EV-1A	5.1852*	1.776×10^{11}	2.898
	EV-18	2.6179*	9.648×10^{10}	3.117
	EV-2	7.5115*	3.266×10^{11}	3.678
Fe	EFe-1A	1.8019*	1.659×10^{11}	8.537
	EFe-18	1.3558*	1.320×10^{11}	9.025
	EFe-2A	2.2848*	2.193×10^{11}	8.901
	EFe-28	1.4586*	1.396×10^{11}	8.876
	EFe-3	2.5695*	2.198×10^{11}	7.933
	EFe-F3	6.846	5.851×10^{11}	7.922
	EFe-F4	8.392	7.960×10^{11}	8.792
Ni	ENi-lA	1.9627*	3.715×10^{11}	18.45†
	ENi-18	2.7754*	5.482×10^{11}	19.25
	ENi-2	3.5241*	6.732×10^{11}	18.62
	ENi-3	2.8632*	4.626×10^{11}	15.78
Zr	EZr-1	8.8429	1.296×10^{11}	2.220
	EZr-2	2.4769	4.127×10^{10}	2.340†
Nb	ENb-1A	4.5068*	8.673×10^{10}	3.066
	ENb-18	5.6642*	1.097×10^{11}	2.989
	ENb-23	8.1704	1.972×10^{11}	3.724†
	ENb-24	9.637	2.172×10^{11}	3.476
Mo	EMo-1A	5.3749*	1.132×10^{11}	3.249
	EMo-18	5.0622*	1.120×10^{11}	3.414
	EMo-2	4.1971*	1.002×10^{11}	3.803†

Continued ....

TABLE 1 (Continued)

HELIUM CONCENTRATIONS IN PURE ELEMENTAL SPECIMENS
FROM FIRST RTNS-I IRRADIATION**

Element	Specimen	Mass After Etching (mg)	Number of ^{4}He Atoms Released	^{4}He Concentration (appb)
Pt	EPt-F1	29.8716	1.391×10^{11}	1.508
	EPt-F2	23.4698	1.010×10^{11}	1.394†
	EPt-F3	23.7246	2.165×10^{11}	2.956
Au	EG-40	11.8359	2.619×10^{11}	7.210†
	EG-41	12.7367	1.624×10^{11}	4.170
	EG-42	12.7864	1.729×10^{11}	4.423
	EG-43	11.929	8.048×10^{10}	2.207
	EG-44	13.174	9.310×10^{10}	2.311
316SS	ESS-1A	1.5707*	1.732×10^{11}	10.18
	ESS-1B	1.7990*	2.091×10^{11}	10.74
	ESS-1C	1.3789*	1.589×10^{11}	10.64†
	ESS-1D	1.6928"	1.881×10^{11}	10.27
	ESS-2A	2.4024*	2.620×10^{11}	10.07

*Asterisked specimens were etched to remove the effects of helium recoil into or out of the material.

†Specimens analyzed for both ^{3}He and ^{4}He were not spiked, and therefore the absolute helium concentration has ~twice the uncertainty of the other specimens. The small amount of helium in EZr-2 has a ±8% uncertainty.

**Note significant adjustments must be made to the individual data using the fluence map to account for flux gradients, before helium generation cross sections can be calculated.

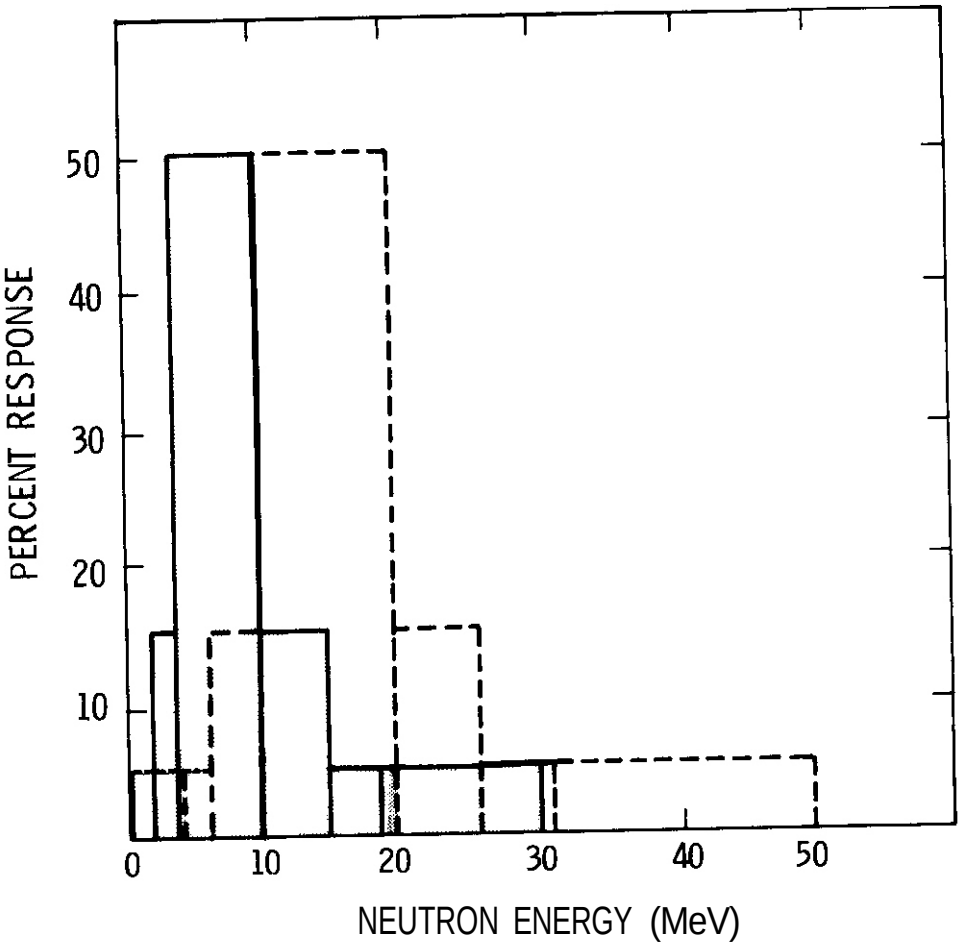

FIGURE 8. Percent Response Versus Neutron Energy for 35 (---------) and 15 (————) MeV Deuterons.

TABLE 2

CONCENTRATIONS OF ^{4}He IN UNIRRADIATED AND ^{3}He IN RTNS-I IRRADIATED MATERIALS

Material	Helium Concentration (Parts per Billion)	
	^{4}He in Unirradiated Material	^{3}He in RTNS-Irradiated Material
C	0.61-0.93	< 0.013
Al	< 0.008	< 0.03
Ti	< 0.003	< 0.03
Fe	< 0.006	< 0.04
Ni	50.047	< 0.03
Cu	< 0.003	< 0.05
Zr	< 0.04	< 0.04
Nb	< 0.001	-
Mo	< 0.002	< 0.02
Au	50.05	< 0.03
Pt	< 0.013	< 0.01
316SS	< 0.035	< 0.04

under Subtask II.A.5.1 of this report. Over 100 helium analyses were conducted on both irradiated and unirradiated samples. Table 1 gives the ^{4}He results for the irradiated samples. Table 2 gives the ^{4}He concentrations measured in unirradiated (but otherwise identically treated) samples of the same materials, and the measured upper limits of ^{3}He generated in the irradiated materials. It should be be noted that the helium generation results in Table 1 must be adjusted individually for fluence gradients before the data from separate specimens can be compared and the helium generation cross sections can be deduced.

Examination of Table 2 shows that no detectable ^{3}He was generated by the RTNS-I irradiation in the stainless steel or in the 10 elements analyzed for this isotope. Unexpectedly, the two unirradiated diamonds released 4.26×10^{10} atoms (0.61 appb) and 7.58×10^{10} atoms (0.925 appb) of ^{4}He, respectively. Even though this is well above the background and mass spectrometer system memory, it is still two orders of magnitude less than that generated by the irradiation. To account for this in the final cross section results, an average helium level of 0.77 appb was subtracted from the carbon results presented in Table 1, Column 5. An uncertainty of only 0.14% was introduced into the final helium generation results from this correction.

The data reduction leading to these results included a detailed study of the background levels that contribute to the total helium measured using the mass spectrometer system. This study led to improvements in the system that increased its sensitivity for the measurement of low helium levels.

C. Total Helium Generation Cross Sections

The total helium generation cross section results for 14.8-MeV neutrons are presented in Table 3. These results are the first direct measurements of total helium generation cross sections for a T(d,n) fusion neutron spectrum.

TABLE 3

HELIUM GENERATION CROSS SECTIONS
FOR 14.8-MeV NEUTRONS

Material	Cross Section (mb)	
	Helium Analysis (Present Results)	Magnetic Quadrupole Spectrometer†
C* (diamond)	900 ± 70**	
Al	143 ± 7	121 ± 25
Ti	38 ± 3	34 ± 7
V	18 ± 2	17 ± 3
Fe	48 ± 3	43 ± 7
Ni	98 ± 6	97 ± 16
cu	51 ± 3	42 ± 7
Zr*	10 ± 2	
Nb	17 ± 5	14 ± 3
Mo	15 ± 2	
Pt*	9 ± 6	
Au*	24 ± 12	
316 SS	57 ± 4	48 ± 7

+Reference 3

*Corrections for a-recoil effects have not been made in the present results for C, Zr, Pt. and Au, which were not etched; this is reflected in the cross section uncertainties for those elements.

**The carbon cross section includes helium production by the $^{12}C(n,n\alpha)^{8}Be$ reaction, which yields 3 helium nuclei.

Most of the helium generation specimens were acid-etched prior to analysis to remove all possible effects of helium recoil. For a variety of reasons, however, the elements C, Zr, Pt, and Au were not or could not be etched effectively. The effect that lack of etching can have on the results was clearly demonstrated with the helium accumulation fluence monitors, as described under Subtask II.A.5.1 of this report. The recoil effects are particularly significant for elements with low helium generation cross sections, such as platinum, irradiated adjacent to carbon-containing materials. The increased uncertainties introduced by the recoil effects are reflected in the cross sections of these four unetched materials. The cross section uncertainties quoted for some elements are expected to be reduced following the analysis of numerous additional specimens that have been subsequently irradiated in RTNS-I.(2)

One revealing correlation that can be made between these results is the comparison of the measured 57-mb effective cross section for N-Lot Fast Flux Test Facility (FFTF) Type 316 stainless steel with the cross section calculated from the pure element results. The combined cross sections of C, Fe, Ni, and Mo, weighted in proportion to their compositions in the steel, and substituting the iron cross section for the as yet unmeasured chromium cross section, give an effective cross section of 54 ± 3 mb. The excellent agreement between these results provides additional confidence in the measurements and the fluence mapping, and gives the important information that minor constituents of stainless steel (other than carbon) are not major contributors to the total helium production rate in a 14.8-MeV neutron spectrum. Comparing the measured stainless steel and elemental cross sections directly shows that In this Type 316 stainless steel, the C, Fe, Ni and Mo generated 1.3%, 58%, 21% and 0.7% of the helium, respectively, with chromium and other constituents providing the 20% balance.

Table 3 also lists some helium production cross section results of Haight and Grimes,[3] based on a series of (n,xα) measurements using a magnetic quadrupole spectrometer. There is generally very good agreement between the results.

VI. REFERENCES

1. D. W. Kneff, H. Farrar IV. R. A. Van Konynenburg, and R. R. Heinrich, A Neutron-Fluence Map for the Rotating Target Neutron Source, AI-ERDA-53188, Atomics International, Canoga Park, CA, December 1976.

2. D. W. Kneff and H. Farrar IV, Helium Generation in Fusion Reactor Materials, Technical Progress Report for Period April-September 1977, AI-DOE-13219, Atomics International, Canoga Park, CA, January 1978.

3. R. C. Haight and S. M. Grimes, "Experimental Studies of (n, charged particle) Cross Sections, Angular Distributions and Spectra with a Magnetic Quadrupole Spectrometer," UCRL-80235, Lawrence Livermore Laboratory, Livermore, CA, December 1977.

VII. FUTURE WORK

Work is now in progress on the analysis of a more extensive set of pure elements, alloys, and separated isotopes that have been irradiated in a second RTNS-I T(d,n) experiment, and in a Be(d,n) neutron environment for 30-MeV deuterons. [The Be(d,n) analyses will be a part of Subtask II.A.4.3.] The RTNS-I results will refine the present measurements and provide helium generation cross sections for additional materials of MFR importance.

VIII. PUBLICATIONS

A paper entitled "Helium Generation in Twelve Pure Elements by 14.8-MeV Neutrons" has been accepted for presentation at the American Nuclear Society 1978 Annual Meeting, San Oiego, CA, June 1978.

I. PROGRAM

Title: Helium Generation in Fusion Reactor Materials
Principal Investigators: D. W. Kneff, H. Farrar IV
Affiliation: Rockwell International, Atomics International Division

II. OBJECTIVE

The objective of this work is to develop helium accumulation fluence monitors for neutron fluence and energy spectrum dosimetry for long-term irradiations in fusion program neutron environments.

III. RELEVANT DAFS PROGRAM PLAN TASWSUBTASK

SUBTASK II.A.5.1 Helium Accumulation Monitor Development

IV. SUMMARY

The helium generation results have been completed for all materials irradiated in the first Atomics International (AI) experiment at the Rotating Target Neutron Source (RTNS-I) at Lawrence Livermore Laboratory (LLL). Part of these results have been used for neutron fluence dosimetry, to adjust the neutron fluence map of the irradiation volume previously calculated from radiometric foil dosimetry. The final fluence map reflects the nonuniformities in the time-averaged neutron profile from the T(d,n) source, and demonstrates the value of helium accumulation fluence dosimetry for fusion neutron irradiations. The map has been used to determine helium generation cross sections for all of the irradiated materials, as described in the Atomics International contribution to DAFS Subtask II.A.4.2 of this report.

V. ACCOMPLISHMENTS AND STATUS

Detailed Fluence Map for the Rotating Target Neutron Source (RTNS-I) -- D. W. Kneff and H. Farrar IV (Atomics International)

A. Introduction

Helium accumulation fluence dosimetry for the characterization of a neutron environment is based on the irradiation of selected materials in the region of interest, and the subsequent measurement with a high-sensitivity gas mass spectrometer of the total amount of helium generated. Dosimetry information can be extracted either from a knowledge of the helium production cross sections or from a comparison of relative helium generation rates in multiple specimens of the same material. This technique is particularly well-suited for long-term irradiations, since the helium measurements can be made accurately even at parts per billion levels, the reaction product of interest is stable, and the method can be used to obtain both neutron fluence and energy information from combinations of helium-generating materials,

The first application of this technique to fusion neutron spectra was its use in constructing a detailed neutron fluence map for the irradiation volume of the first AI RTNS-I experiment. The purpose of this experiment was to measure the 14.8-MeV total helium generation cross sections of twelve pure elements and Type 316 stainless steel. The fluence map was required to calculate cross sections from the measured helium generation concentrations in the various samples. The resultant map has successfully demonstrated the use of helium accumulation fluence dosimetry in high-energy neutron irradiations. Equally important, the experiment has provided helium generation cross sections for future dosimetry applications. The final fluence map is described here, and the evaluated cross sections are presented In this report under Subtask II.A.4.2.

B. Irradiation and Initial Analysis Summary

The irradiation experiment has been described in detail elsewhere. ("*) The experimental geometry consisted of a small stainless steel capsule containing four pure element wire rings and multiple samples of numerous helium generation specimens. The specimens were arranged in layers and sandwiched between sets of thin foils. The capsule assembly was irradiated with the plane of the foils perpendicular to the neutron source axis. Following the irradiation, the foils were cut into small segments for individual radiometric counting at Argonne National Laboratory (ANL) and LLL. The counting results were combined with the segment masses to determine an average neutron fluence for each foil segment. An analytical procedure was then used to derive an approximate neutron fluence map for the irradiation volume from the radiometric fluence dosimetry results.[1]

The pure element wire rings were cut into small segments, etched to remove the effects of helium recoil into or out of the segments, and analyzed individually for helium in the high-sensitivity gas mass spectrometer. Since all segments of each wire ring were subject to the same T(d,n) neutron energy spectrum, their relative helium generation results could be used to adjust the fluence map for details for which the large foil segments were insensitive. An initial analysis using preliminary helium generation results effectively demonstrated this procedure.[2] During this report period the helium data analysis was completed and a final fluence map was constructed.

C. Helium Generation Analysis Results

The final helium concentration results for the 59 segments comprising the four Al, Cu, and Fe helium accumulation dosimetry wire rings are given in Tables 1-3. The rings were positioned concentric with

TABLE 1

HELIUM CONCENTRATIONS IN COPPER DOSIMETRY RING FROM FIRST RTNS-I IRRADIATION

Specimen	Mass After Etch (mg)	Number of ^{4}He Atoms Released	Helium Concentration (Parts per Billion)
ECu-WA	5.9477	3.787×10^{11}	6.720*
ECu-WB	2.8714	1.921×10^{11}	7.061*
ECu-WC	3.5119	2.443×10^{11}	7.342*
ECu-WD	4.0111	2.755×10^{11}	7.250
ECu-WE	3.8774	2.821×10^{11}	7.680
ECu-WF	3.1544	2.436×10^{11}	8.151
ECu-WG	3.6980	3.088×10^{11}	8.814*
ECu-WH	4.1164	3.499×10^{11}	8.972
ECu-WI	3.8474	3.403×10^{11}	9.337
ECu-WJ	3.8072	3.252×10^{11}	9.015
ECu-WK	3.9767	3.403×10^{11}	9.033
ECu-WL	3.7531	3.151×10^{11}	8.859
ECu-WM	4.0280	3.500×10^{11}	9.170*
ECu-WN	4.5793	3.685×10^{11}	8.494
ECu-WO	4.1803	3.232×10^{11}	8.159
ECu-WP	3.6006	2.806×10^{11}	8.226
ECu-WQ	3.9581	3.064×10^{11}	8.172
ECu-WR	2.9760	2.310×10^{11}	8.191
ECu-WS	4.1733	3.382×10^{11}	8.552*
ECu-WT	2.3567	1.784×10^{11}	8.004
ECu-WU	4.2422	3.091×10^{11}	7.689
ECu-WV	3.2501	2.316×10^{11}	7.521
ECu-WW	3.9650	2.670×10^{11}	7.109
ECu-WX	3.9704	2.523×10^{11}	6.706
ECu-WY	4.2035	2.767×10^{11}	6.949*

*Seven specimens were not etched, to study the effects of helium recoil into or out of the copper wire.

TABLE 2

HELIUM CONCENTRATIONS IN OUTER ALUMINUM DOSIMETRY RING FROM FIRST RTNS-I IRRADIATION

Specimen	Mass After Etch (mg)	Number of ^{4}He Atoms Released	Helium Concentration (Parts per Billion)
EA1-WA	0.0738	2.797×10^{10}	16.98
EA1-WB	1.9198	7.614×10^{11}	17.76
EA1-WC	1.4407	6.540×10^{11}	20.33
EA1-WD	1.7178	8.339×10^{11}	21.74*
EA1-WE**	1.6402	5.900×10^{11}	16.11*
EA1-WF	1.1426	6.011×10^{11}	23.56
EA1-WG	1.4355	7.481×10^{11}	23.34
EA1-WH	0.9747	4.812×10^{11}	22.11
EA1-WI	1.4617	6.864×10^{11}	21.03
EA1-WJ	1.5984	7.378×10^{11}	20.67
EA1-WK	1.5667	7.146×10^{11}	20.43
EA1-WL	0.9124	4.052×10^{11}	19.89
EA1-WM	1.5660	6.465×10^{11}	18.49
EA1-WN	1.3616	5.243×10^{11}	17.25

*Two specimens were not etched, to study the effects of helium recoil into or out of the aluminum wire.

**Adjacent to Segments EA1-WA and EA1-WN.

TABLE 3

HELIUM CONCENTRATIONS IN IRON AND INNER ALUMINUM DOSIMETRY RINGS FROM FIRST RTNS-I IRRADIATION

Specimen	Mass After Etch (mg)	Number of ^{4}He Atoms Released	Helium Concentration (Parts per Billion)
EFe-WA	1.6218	1.261×10^{11}	7.208*
EFe-WB	1.1066	8.208×10^{10}	6.878
EFe-WC	1.2638	$9,960 \times 10^{10}$	7.308
EFe-WD	1.0488	8.748×10^{10}	7.734
EFe-WE	1.3770	1.183×10^{11}	7.966
EFe-WF	1.3192	1.129×10^{11}	7.936
EFe-WG	2.0559	1.788×10^{11}	8.065*
EFe-WH	1.4387	1.204×10^{11}	7.760
EFe-WI	0.8629	6.939×10^{10}	7.457
EFe-WJ	0.9763	7.762×10^{10}	7.372
EFe-WK	0.9792	7.542×10^{10}	7.142
EFe-WL	1.3206	9.668×10^{10}	6.789
EA1-W2A	1.1128	6.434×10^{11}	25.90*
EA1-W2B	0.8828	5.585×10^{11}	28.33
EA1-W2D	0.9655	6.915×10^{11}	32.08
EA1-W2E	1.0445	7.409×10^{11}	31.77
EA1-W2F	0.9610	6.651×10^{11}	31.00
EA1-W2G	0.7481	5.046×10^{11}	30.21
EA1-W2H	1.0389	6.793×10^{11}	29.30
EA1-W2I	1.0900	6.671×10^{11}	27.41

*Three specimens were not etched, to study the effects of helium recoil into or out of the iron and aluminum wires.

the axis of the irradiation capsule, and the helium results show generally smooth variations as a function of position around each ring. The difference between these variations and the gradients in the foil-generated fluence map provides a measure of the adjustment required in the map.

D. Adjusted Neutron Fluence Map

The fluence map constructed for RTNS-I from the radiometric foil data is given analytically by the form[1].

$$\Phi(R, \Delta Z) = \alpha\left[C_1 + C_2\beta R + C_3(\beta R)^2 + C_4(\beta R)^3\right], \tag{1}$$

where R is the radial distance from the neutron source axis and AZ is the axial distance from the front face of the capsule. The C_i are constants, β is a correction factor for the changing radial shape of the fluence curve as a function of AZ, and α is the normalization of the radial profile as a function of the distance Z from the neutron source. The measured offset (X_0, Y_0) of the capsule axis from the neutron source axis is incorporated in Equation (1) by transforming the capsule coordinates (R', θ') of the position of interest to coordinates (R, θ) relative to the neutron source axis before calculating the fluence.

When the helium generation results are combined with this map, a refinement in the capsule offset (X_0, Y_0), and an adjustment in Equation (1) then produces the following equation for neutron fluence:

$$\Phi(R, \theta, \Delta Z) = A(R, \theta)\,\Phi(R, \Delta Z), \tag{2}$$

where $A(R, \theta)$ is given empirically by the multiplicative factor:

$$A(R, \theta) = 1 + K(\theta)\,\frac{R}{R_0}\,\sin\left[2(\theta - \theta_0) + \pi\right]. \tag{3}$$

As a result, the final fluence mapping is represented by the equation:

$$\Phi(R,\theta,\Delta Z) = \alpha A(R,\theta)\left[C_1 + C_2\beta R + C_3(\beta R)^2 + C_4(\beta R)^3\right]. \qquad (4)$$

Here θ is the polar angle relative to the neutron source axis, and θ_0, R_0, and $K(\theta)$ are constants. K is double-valued, depending on the quadrant in which θ lies, and represents a small percentage adjustment ($\leq 10\%$) to the fluence. $A(R,\theta)$ reflects the noncircular shape of the fluence profile for a given (R,θ) plane.

Figure 1 compares the helium generation results from Tables 1-3 with the fluence nap previously obtained from the radiometric foils alone[1,2] (dashed line), and with the new fluence map (Equation 4) obtained with all the additional information from the helium accumulation fluence dosimeters (solid line). Examination of the curves in Figure 1 shows clearly how much better the new fluence map describes the measured helium accumulation dosimetry values at all the locations considered. It is also apparent that there is a considerable amount of fine structure in the fluence profile at around 270°, details of which could not be discerned from the coarser radiometric foil data. It should be noted that fluence values obtained from the new (combined radiometric and helium accumulation) mapping at some locations differ from the fluence values obtained from the radiometric foils alone by as much as 12%.

The helium generation results plotted in Figure 1 include those from both the etched and unetched wire segments (filled and open circles, respectively). Comparison of these results demonstrates the importance of specimen etching before helium analysis to remove the effects of helium recoil.[3] The unetched copper segments at approximately 7°, 60°, 93°, 187°, and 277°, and the unetched iron segments at 80° and 270°, were adjacent to carbon-containing materials during the irradiation. Their

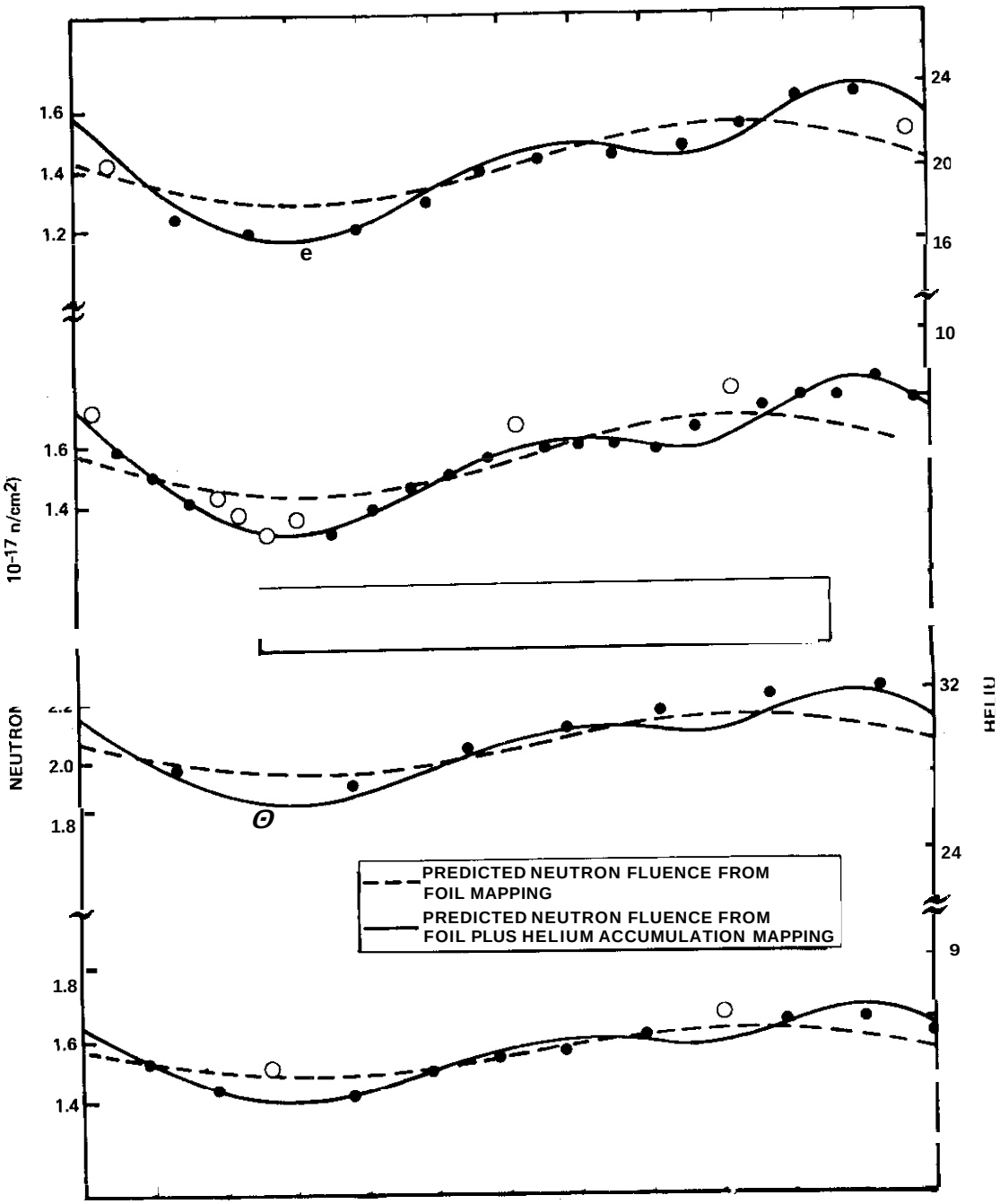
1.6
1.4
1.2
24
20
16
10
1.6
1.4
10-17 n/cm2)
32
2.0
1.8
24
9
1.8
1.6
1.4
PREDICTED NEUTRON FLUENCE FROM FOIL MAPPING
PREDICTED NEUTRON FLUENCE FROM FOIL PLUS HELIUM ACCUMULATION MAPPING

high helium-generation values are attributed to helium recoil into the specimens from the carbon, which has an order-of-magnitude higher helium production cross section. The unetched aluminum segments, on the other hand, were adjacent to materials with cross sections significantly lower than the aluminum, and their low helium generation values (relative to the map) are assumed due to a net helium recoil out of the aluminum. All of the unetched ring specimens were omitted from the final calculation of helium production cross sections (Subtask II.A.4.2, this report).

The nonuniformity of the neutron fluence map (Equation 4) can be clearly seen in Figure 2, which plots contours of constant fluence relative to the capsule axis in the capsule plane containing most of the helium generation materials. The fluence profile *is* seen to be approximately elliptical. The offset of the capsule axis (X_o,Y_o) from the neutron source axis is (-0.3 mm, 0.8 mm).

The absolute uncertainty in this fluence map within the irradiation volume of interest is estimated to be ±6%. This includes an estimated ±3.5% relative uncertainty from the fluence map, an absolute uncertainty of ±2.5% in the radiometric counting results, and an absolute uncertainty of ±4% in the $^{93}Nb(n,2n)^{92m}Nb$ cross section, to which the map is normalized. The $^{93}Nb(n,2n)^{92m}Nb$ cross section used is 463 mb at 14.8 MeV.(4)

The absolute 1σ uncertainty in the mass spectrometric measurements as these low helium concentration levels (6 to 30 atomic parts per billion), is estimated to be less than 3%. An analysis of the numerous helium measurements from the etched Cu, Al and Fe wire segments shows that the helium concentrations have relative 1σ standard deviations with respect to the fluence map of 1.6%, 2.3%, and 1.8%, respectively.

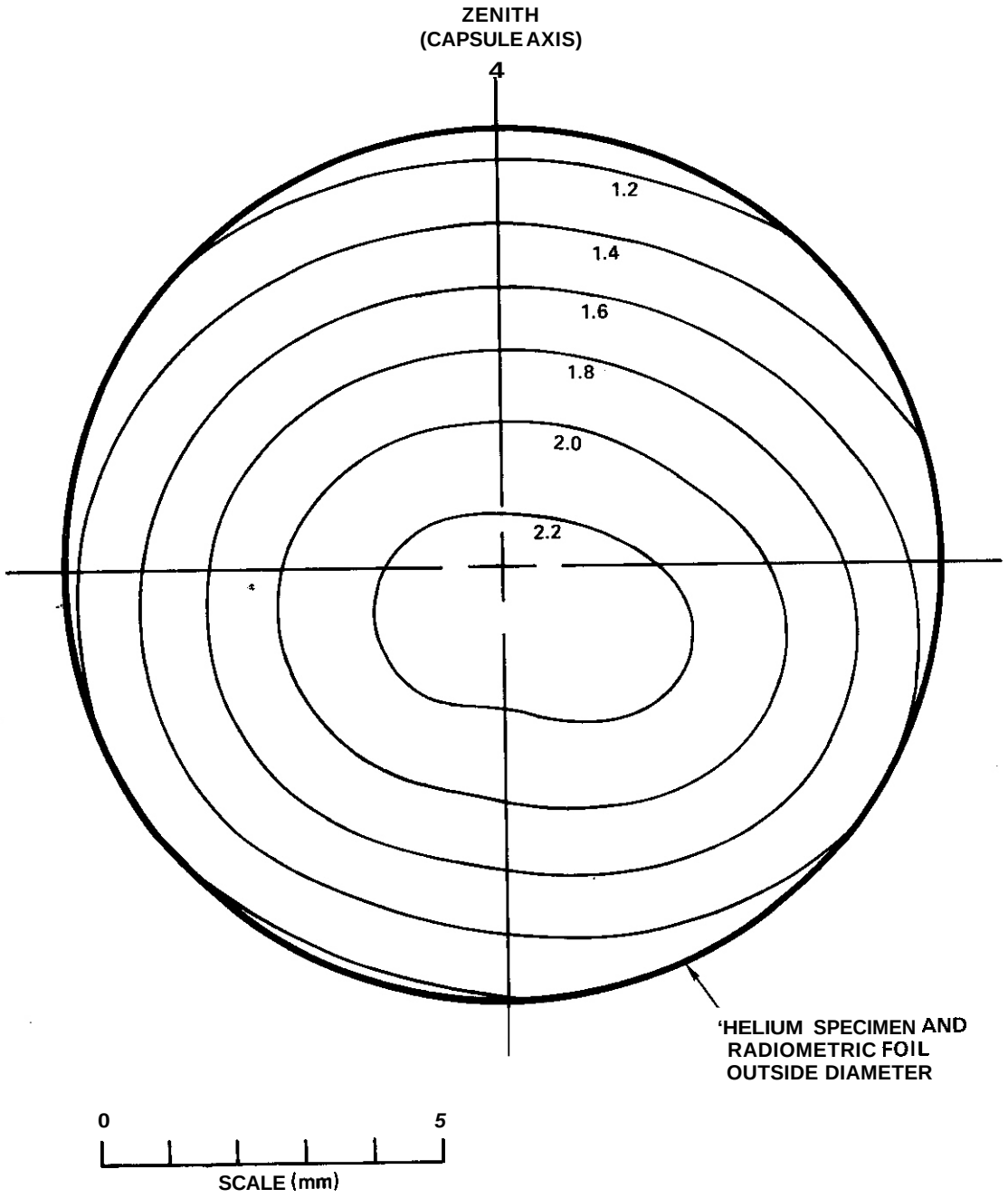

FIGURE 2. Contours of Constant Fluence for Midplane of Al Assembly Irradiated in **RTNS-I** (Units of 10^{17} n-cm^{-2}).

VI. REFERENCES

1. D. W. Kneff, H. Farrar IV, R. A. Van Konynenburg, and R. R. Heinrich, A Neutron Fluence Map for the Rotating Target Neutron Source, AI-ERDA-13188, Atomics International, Canoga Park, CA, December 1976.

2. H. Farrar IV, D. W. Kneff, R. A. Britten, and R. R. Heinrich, "Fluence Mapping of RTNS-I by Helium Accumulation and Foil Activation Methods," Proc. Symp. on Neutron Cross-Sections from 10 to 40 MeV, M. R. Bhat and S. Pearlstein, eds., pp. 175-184, Brookhaven National Laboratory, NY, Juiy 1977.

3. H. Farrar IV and D. W. Kneff, Helium Generation in Fusion Reactor Materials, Technical Progress Report for Period October 1976 - March 1977, AI-ERDA-13201, Atomics International, Canoga Park, CA, May 1977.

4. D. R. Nethaway, "The $^{93}Nb(n,2n)^{92m}Nb$ Cross Section," UCRL-80097, Lawrence Livermore Laboratory, Livermore, CA, September 1977.

VII. FUTURE WORK

The helium accumulation analysis procedures used in this work will be further developed and extended to mapping the neutron fluence and energy spectra for the second AI RTNS-I irradiation and for the recent Be(d,n) irradiation. Both of these irradiations included a significantly broader range of helium generation materials to refine dosimetry techniques and to measure helium dosimetry cross sections. The Be(d,n) irradiation in particular will provide data to demonstrate the energy sensitivity of helium accumulation dosimetry materials.

VIII. PUBLICATIONS

1. R. R. Heinrich (ANL), L. R. Greenwood (ANL), G. R. Odette (UC-SB'), H. Farrar IV (AI), R. Dierckx (LASL), and R. Gold (HEDL), "Dosimetry Needs for the Magnetic Fusion Materials Program," Proc. Second ASTM-EURATOM Symposium on Reactor Dosimetry: Dosimetry Methods for Fuels, Cladding, and Structural Materials, W. C. Morgan, ed., Palo Alto, CA, October 1977.

CHAPTER 4

SUBTASK B: DAMAGE PRODUCTION

I. PROGRAM

Title: Damage Analysis
Principal Investigator: M. T. Robinson
Affiliation: Oak Ridge National Laboratory

II. OBJECTIVE

The objective of this work is to construct both atomistic and continuum (transport theory) models of collision cascade development in solids and to apply these models to radiation damage production, to sputtering, and to plasma particle backscattering problems.

III. RELEVANT DAFS AND PMI TASK/SUBTASK

DAFS SUBTASK II.B.2.3: Cascade Production Methodology

PMI SUBTASK III.B.1.3: Development of Theoretical Model Descriptions of Reflection and Backscattering

PMI SUBTASK III.C.1.6: Development of Theoretical Models for Physical and Physichemical Sputtering

IV. SUMMARY

Methods of applying existing neutral particle transport codes to radiation damage production problems are being developed. Studies of the reflection of 10 eV to 5 keV hydrogen isotopes from various solids has been continued, including the effects of implanted hydrogen on the results. The collision cascade simulation code MARLOWE has been improved and adapted to CDC hardware.

V. ACCOMPLISHMENTS AND STATUS

A. Transport Theoretical Studies of Oamaqe Production -- T. J. Hoffman (UCCNO Computer Sciences Division), H. L. Dodds, Jr. (University of Tennessee, Knoxville), M. T. Robinson (ORNL), and 0. K. Holmes (ORNL)

In previous research,[1] it was shown that the neutral particle discrete ordinates computer code ANISN could be used to calculate sputtering yields if provided with a suitable multigroup cross section table to describe the relevant atomic scattering problems. No modifications to ANISN itself were required to treat charged particle transport. Instead, the total macroscopic cross section was modified to account for electronic excitations and small-scattering-angle elastic interactions. The cross section table was based on the well-known approximate treatment of atomic scattering of Lindhard and his co-workers[2] with low energy modifications as given by Sigmund.[3]

Although the one-dimensional ANISN code was sufficient for the sputtering problems investigated before, most applications of transport theory must use two- or even three-dimensional models. For example, the cylindrical symetry of a collision cascade in an amorphous medium requires two-dimensional calculations. These may be accomplished using the two-dimensional discrete ordinates code DOT.[4] The three-dimensional Monte Carlo transport code MORSE[5] also uses the same kind of cross section tables as do ANISN and DOT. The applicability of these codes to particle range and energy deposition calculations is being explored. They have the potentiality of supplying superior replacements for existing codes such as E-DEP-1.[6]

Both ANISN and MORSE have been used to calculate range distributions for 100-keV ^{196}Au atoms recoiling in Au. This case is of interest because of available calculations using the atomistic code MARLOWE and also because experimental data are available.[7] The ANISN and MORSE mean

penetrations agree with each other within the statistical uncertainty of the latter. The comparison with MARLOWE still requires the resolution of differences between the two models. The transport results agree fairly well also with the calculations of Winterbon[8] whose model is essentially similar.

B. Computer Simulation of the Reflection of Hydrogen, Deuterium and Tritium from Amorphous and Polycrystalline Solids -- O. S. Oen (ORNL; on assignment at Max-Planck-Institut fur Plasmaphysik, Garching, W. Germany) and M. T. Robinson (ORNL)

The reflection (backscattering) of 0.01 to 5 keV hydrogen, deuterium and tritium atoms from amorphous and polycrystalline solids has been studied using the binary collision cascade program, MARLOWE. Incident ions striking the target are followed collision by collision until they either emerge through the target surface or their energy falls below 1 eV. Each collision with a target atom consists of an elastic part described by a Thomas-Fermi potential and an inelastic part which is proportional to the velocity of the projectile. The targets chosen were Be, Fe, Mo, W and composite materials such as FeH. For the latter, the sputtering yield of the light atom constituent was also calculated by following the complete collision cascade as it developed in the solid.

The reflection coefficients increase with increasing target atomic number. For 100 eV T ions, for instance, the reflection from amorphous W is an order of magnitude larger than from **Be.** Hydrogen reflection decreases as the hydrogen content of the target increases (replacing metal atoms by hydrogen) and the reflection of H from a pure hydrogen target becomes vanishingly small. With increasing hydrogen content of the target, the, sputtering yield of hydrogen increases, passes through a maximum and then decreases to almost zero. This result may be explained by noting that most of the sputtering is produced by the reflected projectiles as they emerge through the surface.

The reflection increases with increasing incident angle such that total reflection occurs for angles greater than a critical angle. With increasing incident angle, the sputtering yield of the light atom constituent increases, goes through a maximum, and subsequently decreases.

C. Computer Simulation of Radiation Effects in Metals -- M. T. Robinson (ORNL)

The computer program MARLOWE generates collision cascades in crystalline and amorphous media using the binary collision approximation to generate individual particle trajectories. The numerical model has been improved in a number of respects and both the running time and the memory requirements have been significantly reduced. The program (originally written for IBM System/360 equipment) has been adapted to CDC 7600 hardware and has been tested on a machine at LLL using the national MFE computing network and on a machine at the Idaho National Engineering Laboratory using a recently installed link from ORNL. The code runs considerably faster on a CDC 7600 than it does on a 360/195 but requires relatively more of the machine storage capacity. At present, displacement cascades in Cu could be run on a CDC 7600 up to about 50 keV, where on the 360/195, energies as high as 300 keV can be achieved without reprogramming. If adequate access to the NMFECC can be assured, it can be used very effectively in damage analysis applications.

VI. REFERENCES

1. T. J. Hoffman, H. L. Dodds, Jr., M. T. Robinson, and D. K. Holmes, "Sputtering Calculations with the Discrete Ordinates Method," Trans. Am. Nucl. Soc. 27, 266 (1977).

2. J. Lindhard, V. Nielsen, and M. Scharff, "Approximation Method in Classical Scattering by Screened Coulomb Fields," Kgl. Dansk. Videnskab. Selskab, Mat.-fys. Medd. 36, No. 10 (1968).

3. P. Sigmund, "Theory of Sputtering. I. Sputtering Yield of Amorphous and Polycrystalline Targets," Phys. Rev. 184, 383 (1969)

4. W. A. Rhoades and F. R. Mynatt, The DOT III Two-Dimensional Discrete Ordinates Transport Code, ORNL-TM-4280 (1973).

5. M. B. Emmett, The MORSE Monte Carlo Radiation Transport Code System, ORNL-4972 (1975).

6. I. Manning and G. P. Mueller, "Depth Distribution of Energy Deposition by Ion Bombardment," Computer Phys. Comm. 7, 85 (1974).

7. J. B. Roberto and M. T. Robinson, "A Measurement of the Transverse Range of (n,2n) Recoils in Au," Proc. 7th Intern. Conf. on Atomic Collisions in Solids, to be published.

8. K. B. Winterbon, Ion Implantation Range and Energy Deposition Distributions. Volume 2. Low Incident Ion Energies (IFI/Plenum, New York, 1975.

VII. FUTURE WORK

The transport theory models will be improved by developing a code to prepare the required multigroup cross sections, based on scattering from a potential. This will allow closer comparisons with atomistic models as well as more flexibility in fitting experimental situations.

An improved adaptation of MARLOWE to CDC hardware will be begun using the INEL machine.

I. PROGRAM

Title: Irradiation Effects Analysis
Principal Investigator: D. G. Doran
Affiliation: Hanford Engineering Development Laboratory

II. OBJECTIVE

The objective of this work is to determine the characteristics of replacement sequences in face-centered cubic metals, in order to define the behavior required of a code to simulate high energy cascades. The latter will be used to generate defect production functions for correlation analyses of radiation effects.

III. RELEVANT DAFS PROGRAM PLAN TASK/SUBTASK

SUBTASK II.B.2.3 Cascade Production Methodology

IV. SUMMARY

Results of computer simulations of <100>, <110>, and <111> replacement sequences in copper are presented, including displacement thresholds, focusing energies, energy losses per replacement, and replacement sequence lengths. These parameters are tabulated for six interatomic potentials and shown to vary in a systematic way with potential stiffness and range. Comparisons of results from calculations made with ADDES, a quasi-dynamical code, and COMENT, a dynamical code, show excellent agreement, demonstrating that the former can be calibrated and used satisfactorily in the analysis of low energy displacement cascades. Upper limits on <100>, <110>, and <111> replacement sequences were found to be ∿10, ∿30, and ∿14 replacements, respectively.

V. ACCOMPLISHMENTS AND STATUS

A. Computer Simulation of Replacement Sequences in Copper -- J. O. Schiffgens (HEDL) and D. M. Schwartz (Cal. State University, Northridge, CA.)

1. Introduction

During reactor operation, most of the primary knock-on atoms (PKA's) formed by neutron interactions in reactor components produce vacancies and interstitials, some of which annihilate rapidly while others cluster or migrate to various extended stationary defects. Subsequent property changes are, for the most part, a direct result of the accumulation and growth of such defects. If vacancies and interstitials are formed close to each other, the probability of annihilation is high, and net damage production is low. Consequently, it is important to recognize and analyze the phenomena controlling the magnitude of this initial vacancy-interstitial separation.

Early theories on radiation induced atomic displacement assumed that atoms of a crystal lattice can be treated as though they are instantly ejected from lattice sites when they receive energy in excess of some threshold E_T, independent of the direction in which they are struck.[1] However, the instantaneous ejection as the energy received by lattice atoms exceeds E_T is unreasonable.[2] The fate of an atom having an energy near E_T must be critically dependent upon the manner in which particular configuration of the neighbors responds to its motion. This, in turn, depends upon the local chemical composition, the nature of the chemical bond, the temperature, and the direction in which the atom moves. Hence, the probability of ejection must vary systematically from zero to unity over an energy range $\hat{E}_T - \varepsilon < E < \hat{E}_T + \varepsilon'$, where ε' may be larger than $\hat{E}_T$ (the average displacement threshold) in value.

When the mean free path of a displaced atom decreases to the order of the lattice parameter (i.e., has kinetic energy $\lesssim 1$ keV) the repetitive lattice symmetry imposesconditions upon the possible modes of momentum transfer. The result is an increase in the probability of initiating a set of correlated collisions, such as an energy pulse propagated along a row of

atoms. These pulses may be of the kind proposed by Silsbee[3] for which nearest neighbor atoms to the row are distant and do little more than siphon off small quantities of energy, or of the kind proposed by Nelson and Thompson[4] for which nearest neighbor atoms to the row are close and tend to serve as windows or lenses to focus momentum down the row. When only energy is transported the phenomenon is referred to as a focusson; when energy and mass are transported the phenomenon is referred to as a replacement sequence. The former is associated primarily with close packed rows (<110> rows in fcc and <111> rows in bcc) and provides a mechanism for the rapid transport of energy far from the initiating event. In contrast, the latter consists of a series of consecutive replacement collisions along a given crystallographic direction and provides a mechanism for the formation of a vacancy and interstitial many lattice spacings apart.

Although the existence of replacement sequences is commonly accepted in the field of radiation effects, there is little direct experimental evidence for them and what is available is contradictory.[5] For example, with various experimental techniques, replacement sequence lengths have been deduced to be from <20,[6] to a few hundred,[7] to >1000[8] replacements. In addition to analyzing such data as sputtering patterns from the back-scattering of charged particles[9] or transmission sputtering,[6] the disordering of ordered alloys has been employed to determine replacement sequence length. Relating the length of <110> replacement sequences to changes in the saturation magnetizing of Ni_3Mn during thermal neutron irradiation is an example of the latter. Kirk, Blewitt, and Scott,[10] who have developed this technique, estimate the average length of <110> sequences per 450 eV (n,γ) recoil at from 66 to 132 replacements. As will be shown, this range is considerably longer than the longest sequence obtained in this analysis.

This paper is concerned with the atomistic computer simulation of replacement sequences. In most previous studies of this kind the approach has been to choose a single computational method and a single interatomic potential (to model a given material) and then explore the implications of this particular combination. The objective here is the determination of replacement sequence characteristics in copper and the analysis of their

sensitivity to the choice of interatomic potential, using two computational methods.

Atomistic computer simulations of radiation damage production have been performed by the dynamical method,[11,12] the binary collision method,[13,14] and the quasi-dynamical method.[15,16] From a calculational point of view, the dynamical method, which incorporates a many-body treatment, is ideally suited to the analysis of low energy cascades, in general, and replacement sequences, in particular. However, this method requires considerable computer memory and relatively long run times, making computation expensive. The binary collision method, as its name suggests, considers only single interactions between individual pairs of atoms at any specific time during the evolution of a sequence. Although such calculations are very fast, they cannot accurately simulate replacement sequences which require consideration of many relatively weak forces arising from multiple simultaneous interactions.[17] The quasi-dynamical method is intended to combine much of the accuracy and realism of the dynamical method with the speed and economy of the binary collision method. The quasi-dynamical method consists of a restricted many-body treatment with various calculational parameters which may be set so as to approximate the dynamical method as closely as desired. The key to efficient application of this method lies in setting the calculational parameters in a optimum way, i.e., so as to yield acceptable accuracy at reasonably high computational speeds.

The procedure followed in this study consists of using a dynamical code, COMENT,[12] to characterize the expected behavior for a given initial PKA momentum vector and a particular choice of interatomic potential function. Parameters are adjusted in the quasi-dynamical code ADDES[16] to obtain both acceptable agreement between the two methods and to establish a relative accuracy for the quasi-dynamical method. ADDES is then employed to economically characterize the behavior of the three well-established types of fcc replacement sequences (<110>, <100>, <111>) over a wide range of energies and angular deviations, thus establishing theoretical bounds on replacement sequence behavior.

2. Replacement Sequence Characteristics

Before discussing the relative effects of different interatomic potentials on replacement sequences, it is desirable to define the sequence characteristics of primary interest. These are the focusing energy, the average energy loss per replacement, and the replacement sequence length.

a. The focusing energy E_f is the energy below which the sequence will focus. It is defined as the maximum kinetic energy of the nth atom such that the focusing parameter

$$\Lambda = \alpha_{n+1}/\alpha_n \tag{1}$$

is unity. The α's are the angular deviations of successive replaced atoms from the sequence axis, measured when their kinetic energies E_n and E_{n+1} are maxima.

b. The energy dissipated to the atoms adjacent *to* a replacement sequence axis is defined for each collision as

$$\Delta E = E_n - E_{n+1} \tag{2}$$

In calculating the average energy loss, $\Delta\hat{E}$, the atypical loss in the first replacement is omitted.

c. The length of the replacement sequence is defined as the number of replacements, N, in the sequence.

It should be noted that dynamical results indicate that the number of replacements in a <110> sequence often develop in two stages.[12] The first stage consists of those replacements occurring during the initial expansion of the sequence while the second stage consists of the replacements occurring during the final relaxation of the lattice. As will be discussed later, the quasi-dynamical method does not model the second stage of the <110> sequences unless uneconomical parameter settings are employed.

3. Interatomic Potentials

In atomistic computer simulations, the interactions among nuclei and electrons during atomic collisions are included to some acceptab

degree of accuracy in a usually simple interatomic potential function. At very high interaction energies (or small interatomic separations) experimental information is sparse. However, in this region, the atomic electrons constitute a minor perturbation on a strong nuclear repulsion so that theoretical potentials should be quite satisfactory. At low energies (or near equilibrium separations) phenomenological potentials may be readily deduced from the generally abundant crystal equilibrium data by parameter adjustment of some assumed function. In the region between extremes, there is a serious lack of theoretical and experimental information. In this region, the effect of the overlap of closed electron shells is substantial, and the description of interactions is usually handled by extrapolation of either the high energy or "equilibrium" potential based on some reasonable physical model. Application of a screening function to the nuclear coulomb potential via the Thomas-Fermi model is an example of the former.

Copper has been selected for simulation because it is an fcc metal with atomic weight near that of iron and because there are considerable data from which interatomic potentials can be derived. Six copper potentials were chosen for this study in an effort to cover the range of physically reasonable possibilities; they include the most commonly used potentials. Three of the potentials are pure repulsive, while the remainder have an attractive part.

In recent radiation damage work[14,16] the screened repulsive Moliere approximation[18] to the Thomas-Fermi potential has been employed. This potential has a single parameter, r_s, the Firsov screening radius, and is given in eV by

$$V(r) = (Z_1 Z_2 e^2/r)\{0.35\ \exp(-0.3\ r/r_s) + 0.55\ \exp(-1.2\ r/r_s) + 0.10\ \exp(-6.0\ r/r_s)\} \qquad (3)$$

As the value of r_s increases, the potential rises more rapidly, resulting in greater repulsive forces (increased stiffness). In previous work[16] it was established that a purely repulsive Moliere potential with r_s = 0.00780 nm will give good values for the displacement threshold energy.[19] On the other hand a screening radius of 0.00738 nm yields a Moliere potential that,

while underestimating the displacement threshold by ∿30%, has the same value at the nearest neighbor distance as a Born-Mayer potential (identified by BM) with parameters determined from elastic constant data.[20] These two potentials will be referred to below as the 738M and 780M potentials.

To observe the effect of changes in functional form of a repulsive potential, a Born-Mayer potential[21] was also employed. This potential is given by

$$V(r) = A\, e^{-B(r - r_0)/r_0} \tag{4}$$

where A = 0.051 eV, B = 13.0 and r_0 = 0.2556 nm.[11] All three repulsive potentials are shown in Fig. 1. Note that the BM potential is inherently stiffer than the 738M or 789M potentials for large interaction energies.

In order to realistically simulate equilibrium lattice behavior, interatomic forces should contain attractive as well as repulsive components. The polynomial technique developed by Johnson[22] and refined by Englert[23] is frequently employed to derive the long range portion of the interatomic potential. The Englert potential[23] is a spline function made up of cubic polynomials:

$$V(r) = A_k(r - r_k)^3 + B_k(r - r_k)^2 + C_k(r - r_k) + D_k \tag{5}$$

where, over the range of interest (0.234 nm ≤ r ≤ 0.4418 nm for this work), k runs from 1 through 8 and the r_k are the interatomic separations at which adjacent cubics are joined. In this study, the Englert potential is spliced to the Moliere potentials with the function:

$$V(r) = A(r - r_1)^5 + B(r - r_1)^4 + C(r - r_1)^3 + D(r - r_1)^2 + E(r - r_1) + F \tag{6}$$

where coefficients are chosen so that the potential and its slope and curvature are continuous at the splice points, r = 0.155 nm and r = 0.235 nm. Combining Eq. (6) with both the 738M and 780M potentials gives two more potentials which will be referred to below as 738M-E and 780M-E. All coefficients for Eqs. (5) and (6) are presented in Table 1. It should be noted that the mixed Moliere-Englert potential yields threshold energies which agree best with experiment[19] when r_s = 0.00738 nm.[12]

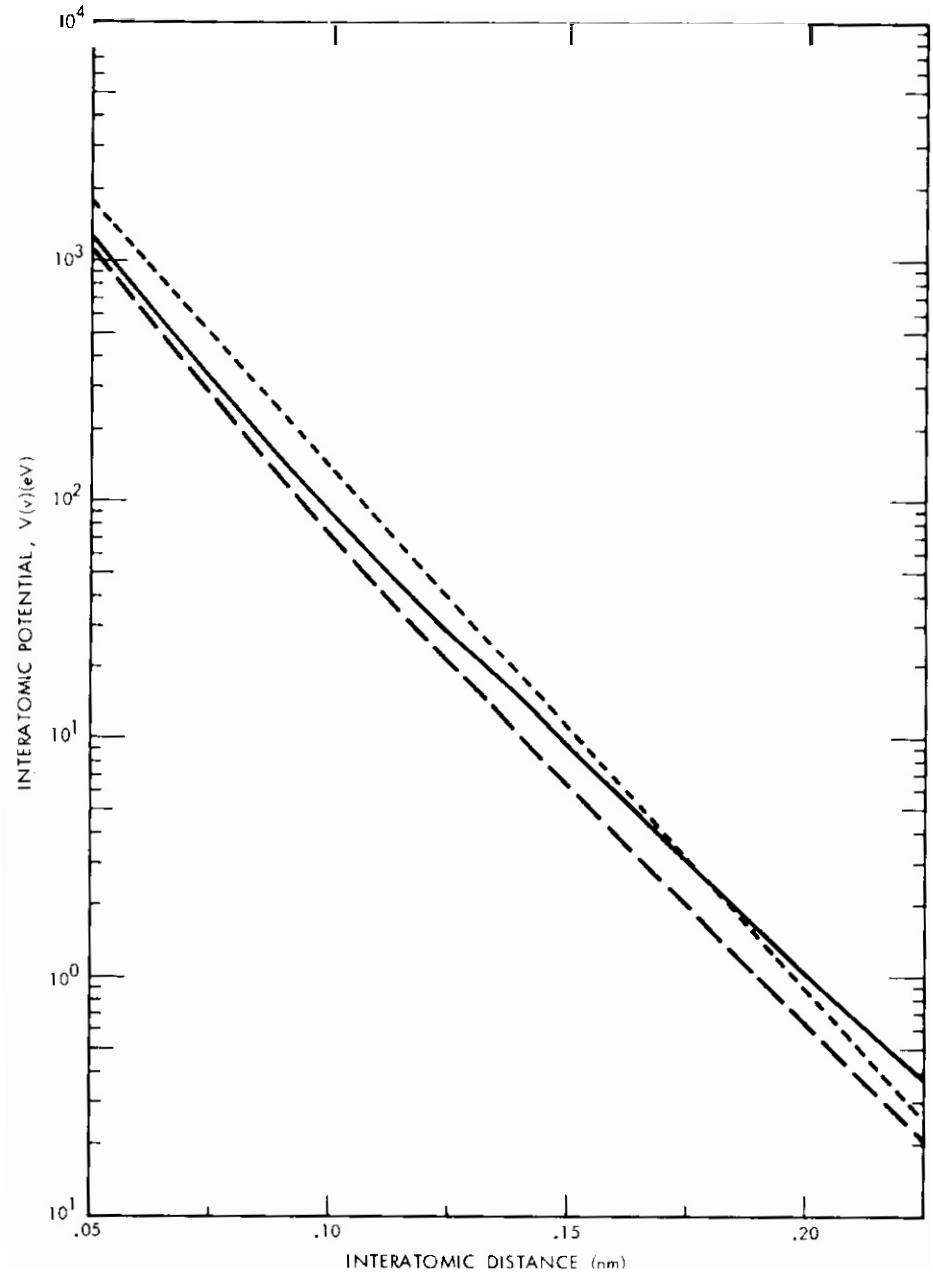

FIGURE 1. Plots of the Interatomic Potentials 738M (— —), 780M (——), and BM (---) Versus Interatomic Distance.

TABLE 1
POTENTIAL PARAMETERS

A. The coefficients for the long range part of the Moliere-Englert potential (See Equation 5)

K	r_K(nm)	$A_K(\frac{eV}{nm^3})$	$B_K(\frac{eV}{nm^2})$	$C_K(\frac{eV}{nm})$	D_K(eV)
1	.20	-3238.2	639.81	-44.591	0.8453
2	.2551	- 258.148	104.5285	- 3.57854	-0.210930
3	.3061199	-2221.407	65.0164	5.07164	-0.155699
4	.3341810	1507.669	-121.9882	3.47295	-0.011272
5	.3607658	- 80.144	- 1.7445	0.18353	0.023168
6	.4209149	2186.182	- 16.2063	- 0.89620	0.010455
7	.4311190	-1575.972	50.7171	- 0.54405	0.001945
8	.4418461	0.0	0.0	0.0	0.0

B. The coefficients for the intermediate part of the Moliere-Englert potential (See Equation 6)

	r(nm)	$A(\frac{eV}{nm^5})$	$B(\frac{eV}{nm^4})$	$C(\frac{eV}{nm^3})$	$D(\frac{eV}{nm^2})$	$E(\frac{eV}{nm})$	F(eV)
738 M-E Splice	.155 to .235	-1638620.1	206078.37	-9105.818	443.7922	-32.35393	0.685515
780 M-E Splice	.155 to .235	-2574998.8	228017.70	-10026.290	780.6601	-49.28877	0.921295

The Johnson potential[22] has the form of a power series:

$$V(r) = 611.17172 - 11426.2204\, r + 85480.690\, r^2 - 319656.06\, r^3 + 596902.0\, r^4 - 444795.0\, r^5 \quad (7)$$

where, as for Eqs. (5) and (6), V(r) is in eV and r is in nm. In this study, the Johnson potential is spliced directly to the BM potential at r = 0.17 nm. The resulting potential will be referred to below as the BM-J potential. The 738M-E, 780M-E, and BM-J potentials and respective interatomic forces are presented in Fig. 2.

4. Threshold Calculations

Odette and Schwartz[24] have recently shown that, by assuming a spontaneous recombination distance of 0.7230 nm (two lattice units), the ADDES code yields defect production data which fit the experimental data of Riley and Jung.[25] Table 2 shows the displacement thresholds obtained with

TABLE 2

THRESHOLD ENERGIES, E_T AND CORRESPONDING ADDES PARAMETER SETTINGS, E_M, P_M, T_F

Potential	E_T (eV) <100>	E_T (eV) <110>	E_M (eV)	P_M (eV)	T_F (eV)
Repulsive					
738M	14-16	12-14	0.23	0.90	1.13
780M	20-22	20-22	0.36	1.20	1.56
BM	26-28	22-24	0.20	1.00	1.25
Repulsive and Attractive					
73811-E	20-22	16-18	0.20	-0.60	-0.30
780M-E	26-28	22-24	0.33	-0.60	-0.30
BM-J	26-28	24-26	0.00	-0.30	-0.05

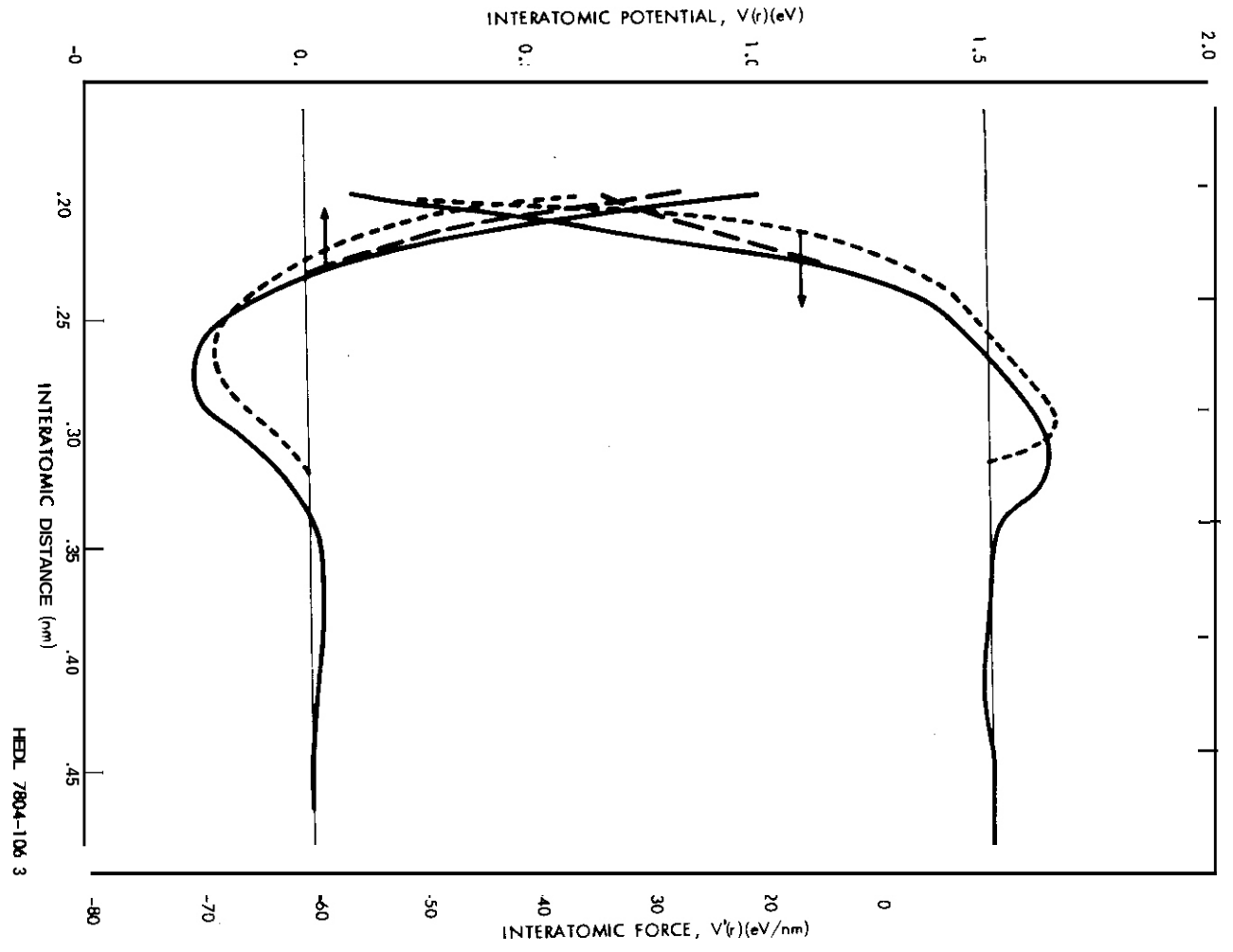

FIGURE 2. Plots of the Interatomic Potentials 738M-E (— —), 780M-E (——), and BM-J (---), and Their Corresponding Interatomic Forces, Versus Interatomic Distance. r_o Is the Equilibrium Distance Between Nearest Neighbors in the Ideal Lattice and a Is Lattice Parameter.

AOOES using this spontaneous recombination radius. Threshold values, E_T, are given for PKA's in both the <110> and <100> directions. Note that with the exception of the 780M potential the lowest thresholds were found in the <110> directions. All threshold values were obtained employing polar and azimuthal angles of 87.9" and 42.9°, respectively, for the <110> and 88.6" and 1.4°, respectively, for the <100>. These correspond to an impact parameter of ~0.0130 nm.

Table 2 shows clearly the increased energy stiffness of the potentials in going from the soft 738M (or 738M-E) to the stiff BM (or BM-J). As will be discussed later, this increase is also reflected in relatively higher focusing energies for the stiffer potentials.

The ADDES parameter settings employed in determining the threshold values are shown in Table 2. The three parameters are:

E_M = the minimum pair interaction potential energy for initiation of atomic motion;

P_M = the maximum potential energy below which an atom's motion may be terminated;

T_F = the maximum total energy below which an atom's motion may by terminated.

The values of these parameters determine the degree of rigor in ADOES calculations. To gain insight into their significance, it is helpful to consider the behavior of a single atom in a simulation. An atom is assumed stationary ("frozen") until it is "bumped" by a moving atom such that the potential energy of pair interaction exceeds E_M. At this point integration of the equations of motion *of* the atom begins. The integration will continue until its total energy (kinetic plus potential) is below T_F and its potential energy is below P_F. This double restriction allows one to adjust the maximum amount of kinetic energy that will be artificially dissipated when motion is frozen, but, at the same time, avoid freezing slowly moving atoms just entering into strong pair interactions.

The lower that E_M, P_F, and T_F are set, the more closely an ADOES calculation can be made 'to approximate a dynamical calculation. The

values chosen in Table 2 were selected empirically as the lowest computationally tractable settings. Because the search procedures in ADDES are designed for 50 to 100 atoms moving at any instant during a run, the run times increase rapidly when the parameters are decreased substantially below the values shown in Table 2. These relatively inefficient choices were only employed in the threshold determinations.

5. Calibration and Validity of the Quasi-Dynamical Method

In general, calibration of ADDES requires different parameter settings for each potential. These parameters were selected by requiring that ADDES and COMENT results from selected calculations agree as accurately as possible while demanding short computation times for ADDES relative to COMENT. The initial PKA energies and directions chosen for calibrating ADDES were 25 eV at polar and azimuthal angular deviations of 1" from the <110>, and 150 eV at angular deviations of 1.76° and 1°, respectively, from the <111>. These choices were based on the predetermined sensitivity of <110> sequences to both the stiffness and range of the interatomic potential and the details of the calculational model, and the sensitivity of the <111> sequences to only the stiffness of the interatomic potential.

It was found that the accuracy and speed of the quasi-dynamical calculations are most sensitive to the value of the parameter E_M. As E_M is lowered, the accuracy of the ADDES calculations in reproducing COMENT calculations increases significantly for near <110> replacement sequences; the <111> sequences are relatively insensitive to E_M. The insensitivity of the latter is due to the predominance of interactions with energies well above E_M (>>1 eV) in determining the <111> replacement sequence characteristics. In contrast, the window atoms neighboring a <110> replacement sequence experience interaction energies comparable to E_M (~1 eV). Unfortunately, the increase in accuracy obtained in the <110> by lowering the E_M threshold is accompanied by a systematic increase in run time, most notably for the higher index <111> events, due to the increase in the number of moving atoms.

The final E_M values chosen for each potential are listed in Table 3 along with the P_F and T_F values discussed below. A value of E_M =

TABLE 3

AODES PARAMETER SETTINGS

Potential	E_M (eV)	Separation (nm) Corresponding to E_M	P_F (eV)	T_F (eV)
738M	1.0	.190	2.25	3.25
780M	1.0	.199	3.5	4.5
BM	0.75	.203	2.3	3.3
738M-E	1.0	.191	0.1	1.1
780M-E	1.0	.198	0.1	1.1
BM-J	0.50	,202	0.1	1.1

1.0 eV proved satisfactory for both the Moliere and Moliere-Englert potentials. Because 1.0 eV resulted in a poor comparison between the quasi-dynamical and dynamical simulations for the 25 eV <110> event, somewhat lower values of 0.75 and 0.5 eV were required for the Born-Mayer and Born-Mayer-Johnson potentials. The source of this difference is that both the BM and BM-J potentials are relatively "stiff" in comparison to the M and M-E potentials.

A value of P_F was selected for each potential such that the termination of motion for an atom in an expanding <110> sequence would occur only after it had transferred essentially all of its available energy to the next atom in the sequence. Setting $T_F = P_F + 1.0$ was found to yield acceptably accurate results for events near the <110> and gave reasonable run times when simulating events near the <111>.

After calibrating ADDES, the validity of the quasi-dynamical method was tested by comparing results from AODES and COMENT calculations on replacement sequences. We chose PKA's with the following energy and angular deviations (polar, azimuthal) from given focusing directions:

150 eV (1.76°, 1°) <111>,

40 eV (1°, 1") <100>,

25 eV (1°, 1") <110>, and

50 eV (5°, 5°) <110>.

Replacement sequences in the <110>, <100>, and <111> have been regularly observed in computer simulations. Preliminary code comparisons indicated that the most significant differences occur for small deviations from the <110> direction. Therefore, two near <110> directions were used to determine the sensitivity of the quasi-dynamical code to the angular deviation from the <110> direction.

6. Results and Discussion

Table 4 shows values of the focusing energy E_F, the average energy loss per replacement ΔE, and the replacement sequence length N obtained with COMENT in five directions and with ADDES in three directions near the <100> and <110>, for all six potentials. The E_F values were obtained by fitting the focusing parameter data to

$$\Lambda(E_i) = a\ E_i^{\,b} \tag{8}$$

and finding E_F by solving $\Lambda(E_F) = 1$. E_i is the maximum kinetic energy of the replacement atom; hence, the uncertainty in E_F should generally not exceed $\Delta\hat{E}$, the average energy loss per replacement. Except near the <110> the ADDES and COMENT values seldom differ by more than this, which supports the choice of ADDES parameters. Focusing energies for the 150 eV turned out to be too much below the <111> focusing energy (as shown later in this section) to be useful in determining E_F.

Note that, within about ± 15 percent, the focusing energy obtained with a given potential is independent of PKA initial energy and angular deviation from the nominal crystallographic focusing direction. For each potential, the focusing energy from COMENT runs was averaged for all PKA initial energies and angular deviations from a nominal direction.

TABLE 4
REPLACEMENT SEQUENCE CHARACTERISTICS FROM COMENT (C) AND ADDES (A) RUNS

ENERGY	DIRECTION ANGULAR DEVIATION NOMINAL	POLAR	AZIMUTHAL	POTENTIAL	E_F(eV) C	A	$\Delta\hat{E}$ (eV) C	A	N C	A
25 eV	<110>	1°	1°	738M	20.4	14.8	.5 ± .1	.7 ± .2	34a	16
				780M	24.4	20.2	.7 ± .2	.7 ± .3	16a	10
				BM	25.6	23.9	.7 ± .1	.8 ±	9c	2
				738M-E	19.8	15.8	1.5 ± .1	1.6 ± .1	12	6
				780M-E	27.1	24.2	1.6 ± .2	1.8 ± .1	9	3
				BM-J	28.6	24.0	1.1 ± .1	1.2	5c	2
38 eV	<110>	3°	3°	738M	19.4		1.9 ± .9		13b	
				780M	25.4		1.4 ± .4		10b	
				BM	34.2		1.1 ± .3		7b	
				738M-E	21.0		2.3 ± .6		10	
				780M-E	28.1		1.9 ± .3		10	
				BM-J	33.8		1.5 ± .3		5b	
50 eV	<110>	5°	5°	738M	22.0	16.0	7.3 ± 1.0	7.9 ± 1.1	7	5
				780M	25.3	21.4	5.2 ± 1.2	5.6 ± 1.3	8	6
				BM	31.5	30.4	2.5 ± 1.5	3.9 ± .6	10	8
				738M-E	20.4	17.0	6.8 ± .9	7.5 ± 1.2	7	5
				780M-E	27.1	23.4	4.5 ± 1.5	5.4 ± 1.0	9	6
				BM-J	35.2	31.8	2.6 ± 1.3	4.1 ± .8	8	8

TABLE 4 (CONT.)
REPLACEMENT SEQUENCE CHARACTERISTICS FROM COMENT (C) AND ADDES (A) RUNS

ENERGY	DIRECTION: NOMINAL	ANGULAR DEVIATION: POLAR	ANGULAR DEVIATION: AZIMUTHAL	POTENTIAL	E_F(eV) C	E_F(eV) A	$\Delta\hat{E}$ (eV) C	$\Delta\hat{E}$ (eV) A	N C	N A
40 eV	<100>	1°	1°	738M	19.7	18.5	4.0 ± .4	4.0 ± .5	6	7
				780M	27.5	27.9	6.0 ± .3	6.1 ± .5	4	4
				BM	39.1	41.4	6.6 ± .4	7.3 ± .6	4	4
				738M-E	12.5	19.5	6.2 ± .4	6.2 ± .6	5	4
				780M-E	19.8	29.3	8.4 ± .1	7.8 ± .5	3	4
				BM-J	48.3	40.6	8.4 ± .5	8.6 ± .5	3	3
30 eV	<100>	2°	4°	738M	20.4		4.6 ± .1		4	
				780M	31.9		6.3		2	
				BM	41.9		7.0		2	
				738M-E	14.2		7.0 ± .1		3	
				780M-E	24.1		8.8		2	
				BM-J	36.2		8.2		2	
150 eV	<111>	1.76°	1°	738M			23.0 ± 4.0	23.0 ± 4.0	5	5
				780M			36.0 ± 4.0	38.0 ± 5.0	3	3
				BM			55.0	55.0	2	2
				738M-E			23.0 ± 3.0	25.0 ± 5.0	4	5
				780M-E			39.0 ± 5.0	40.0 ± 4.0	3	3
				BM-J			56.0	56.0	2	1

a. These replacement lengths are too long to be modeled by COMENT. The values presented were obtained by extrapolating data on the position of atoms relative to the mid-point between lattice sites, and

TABLE 4 (CONT.)

REPLACEMENT SEQUENCE CHARACTERISTICS FROM COMENT (C) AND ADDES (A) RUNS

counting all atoms beyond the mid-point as replacements. Note, ADDES registers a replacement for each atom along the focusing axis that is more than halfway between lattice sites at the end of cascade expansion. COMENT normally registers a replacement for each atom when that atom alone is within 0.154 nm (lattice parameter = 0.362 nm) of an occupied lattice site at the end of cascade collapse.

b For these replacement sequences the atoms tend to come to rest near the mid-point between lattice sites and remain there for very long periods of time, making identification of sequence length difficult.

c For the reasons mentioned under footnote (b), these are only estimates, and may actually be sub-threshold events.

The averaged focusing energies using the 738M, 780M, BM, 738M-E, 780M-E, and **BM-J** potentials are, for <110> sequences, 21, 25, 30, 20, 27, and 33 eV, respectively, and, for <100> sequences, 20, 30, 41, 13, 22, and 42 eV, respectively. The averaged focusing energy for PKA's near the <110> increases by about 40 percent in going from the softest (738M or 738M-E) to the hardest (BM or **BM-J**) potentials. While the addition of an attractive part to the repulsive potentials changed the averaged focusing energy by less than 10% for near <110> replacement sequences, a reduction of as much as 35% was found for near <100> sequences when using the soft potentials.

The $\Delta\hat{E}$'s in Table 4 exclude the first replacement since it is unlike all other replacements in a sequence in that the PKA is surrounded by stationary neighbors as it begins to move and hence requires a larger amout of energy. $\Delta\hat{E}$ values obtained in the <110> are low and the initial energy loss is relatively more significant than in the other directions. Provided that at least three replacements were observed, a standard deviation for $\Delta\hat{E}$ is also included in Table 4. While the energy loss per replacement after the first replacement is quite constant for sequences near the <110>, these losses tend to increase for sequences propagating in other focusing directions. The agreement between results from ADDES and COMENT on the average energy loss per replacement is excellent.

Agreement is also very good on the number of replacements per sequence for sequences near the <100> and <111> (see Table **4**). Sequences near the <110> present **a** special problem. however, owing to the weakness of interactions between sequence and window atoms. For such sequences (except those obtained with the 738M-E and 780M-E potentials), atoms tend to come to rest midway between lattice sites. and remain there for long periods of time, making identification of replacement sequence length difficult. For the same reason, ADDES tends to freeze window atoms shortly after maximum interaction with a given sequence atom, preventing the "closing of windows" from contributing to the sequence length. This final relaxation can only be modeled by ADDES with uneconomical parameter settings. With the parameter settings used here, the length of <110> sequences as calculated by the quasi-dynamical method will typically be two to six replacements shorter than those calculated by the dynamical method.

In addition to the ADDES/COMENT comparisons, ADDES was used to make an exhaustive survey of angles and energies to obtain estimates of average replacement sequence behavior. The results are shown in Tables 5 and 6. Each entry in Table 5 is based on the analysis of about 15 replacement sequences, ten of which were at a deviation of 1°, 1° from the nominal crystallographic direction while five were at an asymmetric deviation of 2°, 3°. The procedure followed for each angle was to begin with a PKA

TABLE 5

MAXIMUM REPLACEMENT SEQUENCE LENGTHS N_{max} AS OBTAINED WITH ADOES

POTENTIAL	N_{max} <100>	E (eV)	N^*_{max} <110>	E (eV)	N_{max} <111>	E (eV)
738M	8	45	17	25	14	300
780M	8	65	18	35	11	400
BM	10	80	24	45	14	600
738EM	7	45	12	37.5	12	300
780EM	8	65	14	50	10	350
JBM	9	82.5	18	52.5	13	550
AVERAGE	8.3 ± 1.0		17.3 ± 4.1		12.3 ± 1.6	

* These values are believed to be too small by about six replacements, as indicated in Table 4.

energy for which the sequence completely defocuses, then decrease the PKA energy in steps of 2.5 eV for the <110> and <100>, and 50 eV for the <111> to locate the maximum replacement sequence length. The maximum sequence length and corresponding PKA energy are presented in the table. These values have not been corrected for the above mentioned tendency of ADDES to underestimate the length of <110> replacement sequences. Note that in each case

the maximum sequence length occurs at an energy well in excess of the focusing energy. That is, although these sequences initially defocus for a number of replacements, their energy drops below the focusing energy before they break up, yielding sequences longer than those presented in Table 4. As would be expected, the runs giving the maximum lengths were all from the set that had the smallest angular deviation from the crystallographic focusing direction.

Table 6 shows the average focusing energy for each potential and nominal direction. From eight to twelve replacement sequences were

TABLE 6

AVERAGE FOCUSING ENERGY $\hat{E}_F$ (eV) AS OBTAINED WITH ADDES

POTENTIAL	<100>	<110>	<111>
738M	22 ± 2	16 ± 2	260 ± 10
780M	29	17	260
BM	40	30	330
738M-E	20	16	240
780M-E	25	23	270
BM-J	40	32	410

analyzed to obtain these values. The PKA energies were always greater than the focusing energy, and, for about half of the sequences, the initial angular deviation of the PKA from the crystallographic focusing direction was greater than 4". The focusing energy was obtained by plotting the focusing parameter versus energy for all (8 to 12) sequences near a given crystallographic direction, drawing a smooth curve through the points, and noting the energy (to within ± 2 eV for <100> and <110>, and ± 10 eV for <111>) for which the focusing parameter is unity. Fig. 3 is a typical plot based on twelve sequences with PKA energies from 28 to 120 eV and

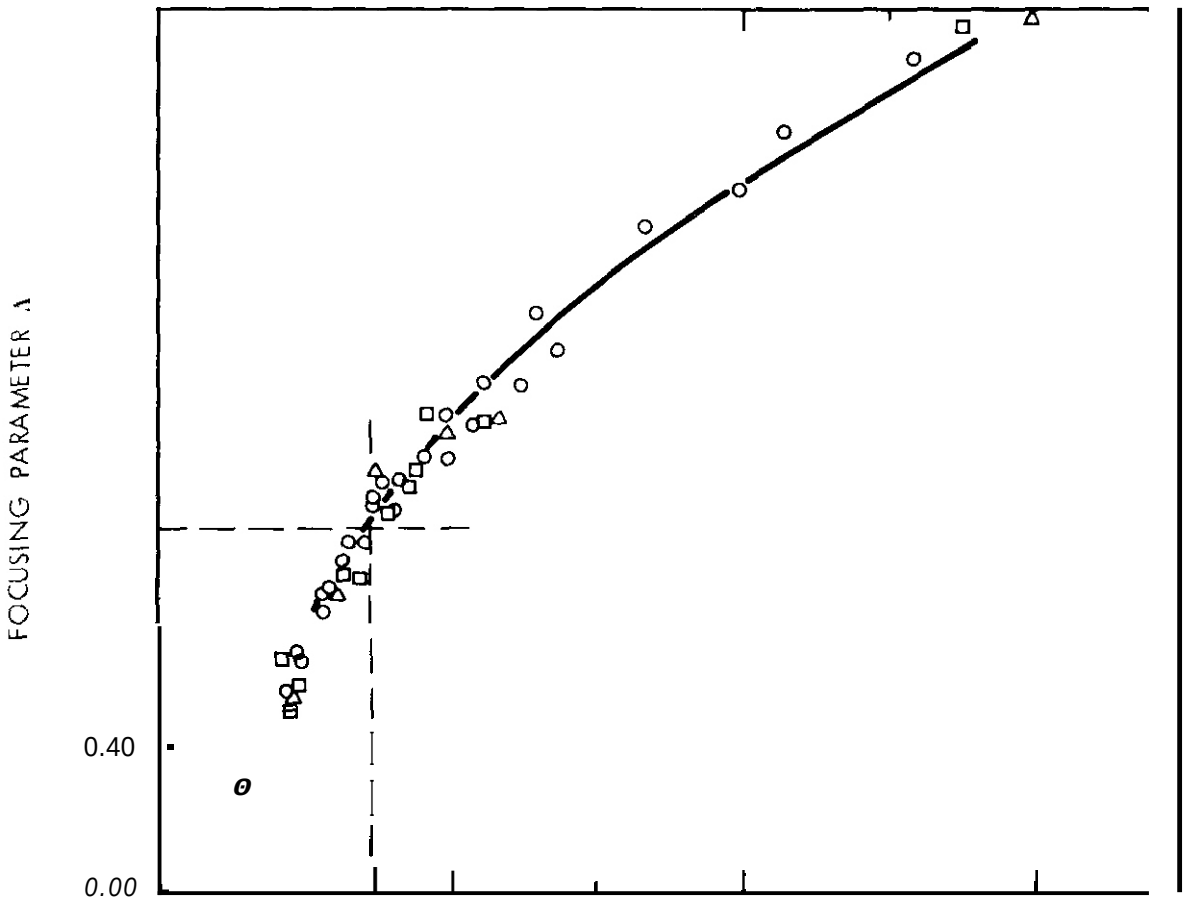

FIGURE 3. Variation in Focusing Parameter with Energy for the 780M Potential Near the <100> direction. The Symbols A, □, and o Refer to Data from PKA's Initiated at Angular Deviations from the <100> Direction of Less Than 2° Between 2° and 4°, and Greater Than 4°, Respectively.

initial angular deviations from the <110> of from 1.8 to 10.1".

From Tables 5 and 6 it is clear that, in general, the presence or absence of a potential well on both N_{max} and E_F is small, with the only clear effect in the N_{max} values obtained in the <110> direction. The presence of an attractive well results in a small decrease in sequence lengths for most cases.

One of the most significant results of this study are the estimates of initial vacancy-interstitial separations. The upper limit for such separations is N_{max} (see Table V). A check of Table IV against Table 6 shows that an increase in E_F is usually accompanied by an increase in $\Delta\hat{E}$ for <111> and <100> sequences. The increase in E_F acts to trap more energy in a given sequence while the increase in ΔE acts to dissipate the energy more rapidly; hence, the two changes have mutually compensating effects on N. As a result the values of N_{max} are relatively insensitive to the choice of potential for <111> and <100> sequences. Even though this change in $\Delta\hat{E}$ is not observed in the <110>, N_{max} is also relatively insensitive to potentials in this direction. Thus, for a wide range of possible potentials, our calculations indicate that the upper limits on <100>, <110>, and <111> replacenent sequence lengths are ∿10, ∿30, an3 ∿14 replacements, respectively. These values are considerably less than those deduced by Kirk et. al.[10] from their experiments.

7. Conclusions

a. Simulation indicates that the upper limits on <100>, <110>, and <111> replacement sequence lengths are ∿10, ∿30, and ∿14 replacements, respectively.

b. The results of these computer simulations are not in agreement with the recent experimental observations of Kirk et. al. on replacement sequence lengths.

c. Excellent agreement can be obtained between ADDES (quasi-dynamical method) and COMENT (dynamical method) on the calculated characteristics of replacement sequences.

d. While the focusing energy is a function of interatomic

potential, it is independent to within about ± 15 percent of initial PKA energy and angular deviation from the nominal crystallographic focusing direction.

e. A range *of* physically reasonable interatomic potentials results in a 20 to 30 percent uncertainty in predictions of replacement sequence length by computer simulation.

VI. REFERENCES

1. J. Neufeld and W. S. Snyder, Phys. Rev. 99, p. 1326 (1355).
2. J. B. Sampson, H. Hurwitz, and H. F. Claney, Phys. Rev. 99, p. 1657 (1965).
3. R. H. Silsbee, J. Appl. Phys. 28, p. 1246 (1957).
4. R. S. Nelson and M. W. Thompson, Proc. Roy. Soc. A 259, p. 458 (1961).
5. T. H. Blewitt, M. A. Kirk, and T. L. Scott, "Replacement Collision Sequences in Metals," Fundamental Aspects of Radiation Damage in Metals, M. T. Robinson and F. W. Young, eds., CONF-751006, Vol. 1, p. 152.
6. K. H. Ecken, Rad. Effects 23, p. 171 (1974).
7. R. W. Balluffi and D. N. Seidman, COO-3158-39, p. 13 (1975).
8. D. Keil, W. Decker, and J. Diehl, Rad. Effects 27, p. 155 (1976).
9. C. Lehmann and P. Sigmund, Phys. Stat. Sol. 16, p. 507 (1966).
10. M. A. Kirk, T. H. Blewitt, and T. L. Scott, Phys. Rev. B, 15, p. 2914 (1977).
11. J. B. Gibson, A. N. Goland, M. Milgram, and G. H. Vineyard, Phys. Rev. 120, p. 1229 (1960).
12. J. 0. Schiffgens and R. D. Bourquin, "Computer Simulations of Low Energy Displacement Cascades in a Face Centered Cubic Lattice," to be published in Proc. Int. Conf. on the Prop. of Atomic Defects in Metals, held at Argonne National Laboratory, October 18-22, 1976.
13. J. R. Beeler, Jr., Phys. Rev. 134, A 530 (1964); 150, p. 470 (1966)
14. M. T. Robinson and I. M. Torrens, Phys. Rev. 9, p. 5008 (1974).
15. I. M. Torrens, J. Phys. F, 3, p. 1771 (1973).

16. D. M. Schwartz, J. 0. Schiffgens, D. G. Doran, G. R. Odette, and R. G. Ariyasu, "A Comparison of Many Bodied and Binary Collision Cascade Models Up to 1 keV," in Computer Simulation for Materials Applications, NBS, 1, p. 75 (1976).

17. Recent modifications to the binary collision code MARLOWE [see M. T. Robinson, ORNL-5328, p. 13 (1977)] have done much to alleviate this shortcoming.

18. G. Moliere, Z. Naturforsch, 2a, p. 133 (1947).

19. P. Jung, R. L. Chapin, H. J. Fenzi, R. Reichelt and P. Wombacher, Phys. Rev. B, 8, p. 553 (1973).

20. I. M. Torrens and M. T. Robinson, "Computer Simulation of Atomic Displacement Cascades in Solids," in Interatomic Potentials and Simulations of Lattice Defects, P. C. Gehlen, J. R. Beeler, Jr., R. I. Jaffee, eds., p. 423, Plenum Press, NY (1972).

21. M. Born and J. E. Mayer, Z. Phys., 75, p. 1 (1932).

22. R. A. Johnson, Rad. Effects, 2, p. 1 (1969).

23. A. Englert, H. Tompa and R. Bullough, "Point Defects and Dislo-actions in Copper," Fundamental Aspects of Dislocation Theory, NBS Special Publ. 317 p. 273 (1971).

24. G. R. Odette and D. M. Schwartz, Trans. ANS 27, p. 316 (1977).

25. R. Riley and P. Jung, "The Simulation of Irradiation Creep," in Proc. Int. Conf. on Rad. Effects, in Breeder Reactor Structural Materials, Scottsdale, Arizona, p. 295 (1977).

VII. FUTURE WORK

This work is being continued to include an analysis of the effect of temperature on replacement sequences.

VIII. PUBLICATIONS

A paper describing this work has been submitted to Radiation Effects.

I. PROGRAM

Title: Radiation Damage Analysis and Computer Simulation

Principal Investigator: Don M. Parkin

Affiliation: Los Alamos Scientific Laboratory, University of California

II. OBJECTIVE

The objective of this work is to develop displacement functions for multicomponent systems.

111. RELEVANT DAFS PROGRAM PLAN TASK/SUBTASK

SUBTASK	II.B.2.3	Cascade Production Methodology
	II.B.4.1	Interface with other designs and other tasks
	II.B.4.2	Develop theory of spectral and rate effects

IV. SUMMARY

A computer code, DISPLCA, has been written to calculate displacement functions for multicomponent systems. Two displacement functions are calculated, the total displacement function and the net displacement function The total displacement function, $n_{ij}(E)$, is the number of atoms of type j, other than the initial knock on atom, which are displaced from their sites when an atom of type i initially has energy E. The net displacement function, $g_{ij}(E)$, is the number of atoms of type j including the initial knock on atom which will be displaced and not subsequently retrapped in a replacement collision when an atom of type i initially has energy E.

V. ACCOMPLISHMENTS AND STATUS

A. Displacement Functions for Multicomponent Systems -- D. M.

Parkin (LASL) and C. A. Coulter (The University of Alabama, University, Alabama)

1. Introduction

Damage parameters have been developed for metals and are widely utilized as correlation parameters and exposure indices. With the requirement of using insulators in intense radiation environments in fusion reactors comes the realization that similar damage parameters are required for these materials. Initial steps in developing damage parameters for multicomponent systems (e.g. insulators, alloys) are described in this report.

2. Displacement Functions

The work in the previous fiscal year has been extended to the calculation of displacement functions in multicomponent systems. Let $n_{ij}(E)$ be the number of atoms of type j, other than the initial atom, which are displaced from their sites when an atom of type i initially has energy E. By reasoning exactly similar to that used for the monatomic case[1] one can show that n obeys the equation

$$S_i(E)n_{ij}(E) = N_j \int_0^{M_{ij}E} dT \frac{d\sigma_{ij}(E,T)}{dT} \rho_k(T)$$

$$+ \sum_k N_k \int_0^{M_{ik}E} dT \frac{d\sigma_{ik}(E,T)}{dT} [\rho_k(T)\, n_{kj}(E-E_{bk})$$

$$+ (1 - \rho_k(T)\, \lambda_{ik}(E-T))n_{ij}(E-T) - n_{ij}(E)]$$

where $\rho_k(T)$ is the probability that an atom of type k receiving energy T will be displaced from its site and $\lambda_{ik}(E)$ is the probability that an atom of type i left with energy E after it displaces an atom of type k

from its site will be trapped in that site. Similarly, the net displacement function $g_{ij}(E)$ is defined to be the number of atoms of type j including the original atom which will be displaced and not subsequently retrapped in a replacement collision when an atom of type i initially has energy E. It can be shown that $g_{ij}(E)$ satisfies an equation exactly like that for $n_{ij}(E)$ above, except that the first term on the right hand side is missing. The boundary conditions for the two functions are different, however, with $n_{ij}(E)$ approaching a value of zero at its threshold energy value for all i, j, while the $g_{ii}(E)$ approach initial values of 1 at their energy thresholds.

3. Results

A computer program DISPLCA to calculate both the displacement functions n and the net displacement functions g has been developed. DISPLCA calculates both single element and multicomponent displacement functions. Preliminary results for Cu, E_d = 22 eV and Al_2O_3, $E_d(Al)$ = 40 eV and $E_d(O)$ = 70 eV,[2] are illustrated in Tables I thru III. Detailed analysis of the results and sensitivity studies have not been completed. However one feature that can clearly be seen is that the G/N ratio is near 0.8 in all cases.

VI. REFERENCES

1. A. Alton Coulter and Don M. Parkin, Trans. Am. Nucl. Soc. 27, 300 (1977).
2. W. Dale Compton and G. W. Arnold, Disc. Faraday Soc. 31, 130 (1961).

VII. FUTURE WORK

Future work will focus on studying the results obtained from the model and obtaining displacement functions for materials of interest for the fusion materials program.

TABLE I

DISPLACEMENT FUNCTIONS FOR COPPER WITH E_d = 22 eV

ENERGY (eV)	N (Cu,Cu)	G (Cu,Cu)	G/N
2.2×10^{1}	1.00	1.00	1.00
4.4×10^{1}	1.27	1.00	0.79
1.0×10^{2}	2.25	1.70	0.76
2.0×10^{2}	4.06	3.13	0.77
4.5×10^{2}	8.75	6.81	0.78
1.0×10^{3}	1.92×10^{1}	1.50×10^{1}	0.78
4.0×10^{3}	7.15×10^{1}	5.60×10^{1}	0.78
1.1×10^{4}	1.78×10^{2}	1.40×10^{2}	0.78
4.2×10^{4}	6.44×10^{2}	5.05×10^{2}	0.78
1.1×10^{5}	1.53×10^{3}	1.20×10^{3}	0.78
4.3×10^{5}	4.73×10^{3}	3.71×10^{3}	0.78
1.1×10^{6}	9.02×10^{3}	7.07×10^{3}	0.78

TABLE II

DISPLACEMENT FUNCTIONS IN Al_2O_3 FOR ALUMINUM ATOMS HAVING INITIAL ENERGY E, $E_d(Al)$ = 40 eV AND $E_d(O)$ = 70 eV

ENERGY (eV)	N (Al, Al)	G (Al, Al)	G/N
4.0×10^{1}	1.09	1.00	1.00
1.1×10^{2}	1.21	1.01	0.83
2.1×10^{2}	1.60	1.22	0.76
4.1×10^{2}	2.36	1.86	0.79
1.0×10^{3}	4.70	3.86	0.82
4.4×10^{3}	1.64×10^{1}	1.38×10^{1}	0.84
1.1×10^{4}	3.71×10^{1}	3.15×10^{1}	0.85
4.1×10^{4}	1.13×10^{2}	9.58×10^{1}	0.85
1.0×10^{5}	2.21×10^{2}	1.88×10^{2}	0.85
4.3×10^{5}	4.73×10^{2}	4.03×10^{2}	0.85
1.1×10^{6}	6.34×10^{2}	5.41×10^{2}	0.85

	N (Al, O)	G (Al, O)	G/N
7.5×10^{1}	0.00	0.00	1.00
1.1×10^{2}	5.13×10^{-2}	4.66×10^{-2}	0.91
2.2×10^{2}	3.56×10^{-1}	3.00×10^{-1}	0.84
4.4×10^{2}	1.06	8.54×10^{-1}	0.80
1.0×10^{3}	2.87	2.25	0.78
4.1×10^{3}	1.23×10^{1}	9.52	0.77
1.1×10^{4}	2.99×10^{1}	2.31×10^{1}	0.77
4.4×10^{4}	1.01×10^{2}	7.79×10^{1}	0.77
1.0×10^{5}	1.84×10^{2}	1.42×10^{2}	0.77
4.1×10^{5}	3.91×10^{2}	3.02×10^{2}	0.77
1.1×10^{6}	5.27×10^{2}	4.09×10^{2}	0.77

TABLE III

DISPLACEMENT FUNCTIONS IN Al_2O_3 FOR OXYGEN ATOMS HAVING INITIAL ENERGY E, $E_d(Al)$ = 40 eV AND $E_d(O)$ = 70 eV

ENERGY (eV)	N (O,O)	G (O,O)	G/N
7.0×10^{1}	1.00	9.44×10^{-1}	0.94
1.1×10^{2}	1.08	8.82×10^{-1}	0.82
2.0×10^{2}	1.33	9.70×10^{-1}	0.73
4.1×10^{2}	1.99	1.46	0.73
1.1×10^{3}	4.01	3.03	0.75
4.6×10^{3}	1.35	1.03	0.76
1.0×10^{4}	2.73×10^{1}	2.10×10^{1}	0.77
4.2×10^{4}	8.06×10^{1}	6.21×10^{1}	0.77
1.1×10^{5}	1.39×10^{2}	1.07×10^{2}	0.77
4.1×10^{5}	2.24×10^{2}	1.73×10^{2}	0.77
1.0×10^{6}	2.74×10^{2}	2.12×10^{2}	0.77

	N (O, Al)	G (O, Al)	G/N
4.3×10^{1}	0.00	0.00	1.00
1.0×10^{2}	1.55×10^{-1}	1.50×10^{-1}	0.96
2.1×10^{2}	5.50×10^{-1}	5.04×10^{-1}	0.92
4.5×10^{2}	1.41	1.25	0.89
1.1×10^{3}	3.63	3.15	0.87
4.1×10^{3}	1.38×10^{1}	1.18×10^{1}	0.86
1.1×10^{4}	3.35×10^{1}	2.86×10^{1}	0.85
4.3×10^{4}	9.57×10^{1}	8.16×10^{1}	0.85
1.0×10^{5}	1.59×10^{2}	1.36×10^{2}	0.85
4.0×10^{5}	2.67×10^{2}	2.28×10^{2}	0.85
1.1×10^{6}	3.31×10^{2}	2.83×10^{2}	0.85

CHAPTER 5

SUBTASK C: DAMAGE MICROSTRUCTURE EVOLUTION AND MECHANICAL BEHAVIOR

I. PROGRAM

Title: Irradiation Effects Analysis
Principal Investigator: D. G. Doran
Affiliation: Hanford Engineering Development Laboratory

II. OBJECTIVE

The objective of this work is to initiate irradiations in the Oak Ridge Reasearch Reactor (ORR) to study the combined effects of helium and displacement damage on microstructures and tensile behavior.

III. RELEVANT DAFS PROGRAM PLAN TASK/SUBTASK

TASK II.C.1.1 Effects of Material Parameters on Microstructure
TASK II.C.2.2 Effects of Helium on Microstructure

IV. SUMMARY

The first fusion materials experiment inserted in ORR, designated MFE-1, includes specimens provided by the OAFS program. The materials, primarily nickel-base alloys in the form of specimens for transmission electron microscopy (TEM), were selected with an emphasis on studying phase stability and the effects of composition on helium-displacement interactions.

V. ACCOMPLISHMENTS AND STATUS

A. DAFS Experiment in the ORR MFE-1 Test - R. W. Powell (HEDL) and G. R. Odette (UCSB)

1. Introduction

Experiments are being conducted in the Oak Ridge Research

Reactor (ORR) to assess the effects of neutron irradiation and high helium generation rates on the properties of metals. The DAFS Task Group is participating in these irradiations to determine the combined effects of helium generation and displacement damage on mechanisms of microstructure evolution and mechanical behavior.

2. Status

The first of a series of fusion materials experiments in ORR, designated MFE-1, began irradiation on February 8, 1978.[1] The OAFS test matrix for this experiment was reviewed by the Microstructural Evolution and Mechanical Behavior Subtask Group, and specimens were fabricated, engraved, heat treated, and encapsulated at HEDL and shipped to ORNL for inclusion in the test.

The original test matrix for the DAFS portion of the experiment consisted of a few tensile specimens and many TEM disks at irradiation temperatures of 350, 450, 550, and 650°C and fluences of 0.3×10^{22} and 1.0×10^{22} n/cm^2 (E>0.1 MeV). Problems with temperature control due to excessive gamma heating have led to a change in the reactor core loading and a probable reduction of fluences to roughly one-tenth of those planned.

The alloys included in the test are given in Table 1. The simple Fe-Ni-Cr ternary series, the most basic set, is to study the relationships between major element composition, swelling and helium effects. Two heats of nickel were included *to* tie with the data bases at the Naval Research Laboratory (NRL) and at Battelle's Pacific Northwest Laboratory (PNL). There is extensive fast reactor (EBR-II) experience on AISI 316; two heats were included in MFE-1 to compare EBR-II and ORR irradiations. Phase stability in nominally solid solution alloys is being studied with alloys D9, D11, D9-C1 and D11-B1; the first two alloys have exhibited extensive molybdenum-rich secondary precipitation during EBR-II irradiation. The binary alloys were included to study solute segregation effects and swelling variability with composition. Strengthening phase redistribution

effects in precipitation hardened alloys are being studied for the γ' phase with Nimonic PE16 and D25, and for the γ'' phase with Inconel 706. Two heats and different solutioning temperatures for Nimonic PE16 were included to investigate carbide redistribution. Precipitation of secondary precipitates such as G phase, η, and M_3B_2 (enhanced helium production) is being studied with A-286, D21, D21-B1 and D25. Titanium-base alloys were included to support mechanical properties tests being performed by the Alloy Development for Irradiation Performance Task Group.

VI. REFERENCES

1. J. W. Woods, A. F. Zulliger and E. E. Bloom, "Status of ORR-MFE-1 and -2 Irradiation Experiments," ADIP Progress Report, April 1978.

VI. FUTURE WORK

The MFE-1 experiment is expected to be removed from the reactor in June 1978. Post-irradiation examination of selected specimens will be initiated shortly after test disassembly.

TABLE 1

OAFS

MFE-1 TEST MATRIX

TEM SPECIMENS

Alloy Series Designation	Alloy[a]	Heat Treatment[b]
Fe-Ni-Cr Ternary	E39 (Fe-20Ni-7.5Cr)	1038°C/1 hr/AC
	E19 (Fe-20Ni-15Cr)	1038°C/1 hr/AC
	E20 (Fe-25Ni-15Cr)T	1038°C/1 hr/AC
	E21 (Fe-30Ni-15Cr)	1038°C/1 hr/AC
	E37 (Fe-35Ni-7.5Cr)	1038°C/1 hr/AC
	E22 (Fe-35Ni-15Cr)T	1038°C/1 hr/AC
	E38 (Fe-35Ni-20Cr)	1038"C/1 hr/AC
	E23 (Fe-45Ni-15Cr)T	1038°C/1 hr/AC
	E24 (Fe-75Ni-15Cr)T	1038°C/1 hr/AC
	E36 (Fe-85Ni-15Cr)	1038°C/1 hr/AC
Pure Ni	NRL heat	*
	BNW heat	700°C/2 hr/AC
AISI 316	M2783	20% CW
	N-Lot	20% CW
Phase Stability	09	1100°C/0.25 hr/AC
	D9	10% CW
	D9	20% CW
	09	30% CW
	D9-C1	20% CW
	D9-C1	1100°C/0.25 hr/AC
	011	1100°C/0.25 hr/AC
	D11-81	1100°C/0.25 hr/AC
Binary Alloys	Ni-Be	900°C/3 hr/FC at 10^{-6} Torr(ANL)
	Ni-Si	900°C/3 hr/FC at 10^{-6} Torr(ANL)
	Ni-Si**	900°C/3 hr/FC at 10^{-6} Torr(ANL)
	Ni-Mo	900°C/3 hr/FC at 10^{-6} Torr(ANL)
	Ni-Ti	900°C/3 hr/FC at 10^{-6} Torr(ANL)
	Ni-Al	900°C/3 hr/FC at 10^{-6} Torr(ANL)
	Ni-Al**	1250°C/0.5 hr/WQ
	Ni-Cu	700°C/2 hr/AC
γ' Redistribution	Nirnonic PE16	1038°C/4 hr/AC
	Nimonic PE16	1038°C/4 hr/AC + 900°C/1 hr/AC + 750°C/8 hr/AC

TABLE 1 (Cont'd)

Alloy Series Designation	Alloy[a]	Heat Treatment[b]
	Nimonic PE16	1038°C/4 hr/AC + 900°C/1 hr/AC + 750°C/8 hr/AC + 765°C/320 hr/AC
	D25	1050°C/0.5 hr/AC + 700°C/24 hr/AC + 800°C/0.5 hr/AC
γ" Redistribution	Inconel 706	1066°C/1 hr/WQ
	Inconel 706	954°C/1 hr/WQ + 843°C/3 hr/AC + 718°C/8 hr/FC to 621°C hold 18 hr total/AC
Carbide Precipitation	Nimonic PE16	1080°C/4 hr/AC + 900°C/1 hr/AC + 750°C/8 hr/AC
	Nimonic PE16	1150°C/4 hr/AC + 900°C/1 hr/AC + 750°C/8 hr/AC
	Nimonic PE16**	1080°C/4 hr/AC + 900°C/1 hr/AC + 750°C/8 hr/AC
Minor Phase Formation	A-286	982°C/1 hr/AC + 718°C/16 hr/AC
	A-286**	982°C/1 hr/AC + 718°C/16 hr/AC
	021	1050°C/0.5 hr/AC + 700°C/24 hr/AC + 800°C/0.5 hr/AC
	D21-B1	1050°C/0.5 hr/AC + 700°C/24 hr/AC + 800°C/0.5 hr/AC
	D25	1050°C/0.5 hr/AC + 700°C/24 hr/AC + 800°C/0.5 hr/AC
Titanium Alloys	Ti-6Al-4V	*
	Ti-6Al-4V	*
	Ti-6A1-4V	*
	Ti-5621	*
	Ti-6242	*
	Ti-15-333	*

a. T - Tensile specimens included also.

** - Different heat.

b. AC - Air cooled; FC - Furnace cooled; WQ - Water quenched

* - Heat treatment performed by another laboratory.

I. PROGRAM

Title: Phase Stability in Irradiated Metals

Principal Investigator: Kenneth C. Russell

Affiliation: Department of Materials Science and Engineering, Massachusetts Institute of Technology

II. OBJECTIVE

The objective is to model the stability of incoherent precipitates under irradiation.

III. RELEVANT DAFS PROSRAM PLAN TASK/SUBTASK

SUBTASK II.C.1.2 Effect of Material Parameters on Microstructure/ Modelling and Analysis.

IV. SUMMARY

A computer solution is given for a mathematical model describing the formation of incoherent precipitates from dilute solutions of substitutional impurities. Irradiation increases the calculated steady state nucleation rates by many orders of magnitude to cause precipitation when even substantial solute supersaturations are by themselves inadequate. The effect of interstitial capture and radiation dissolution is to decrease the nucleation rate, but by factors small compared to the catastrophic enhancement effect of irradiation induced vacancies. Impurity drag, which is not a factor for oversized Ge atoms but should be operative for the smaller Si atoms in Al, is not included in the model. With this simplification, similar results are obtained for both the Si-A1 and Ge-A1 systems. The results of the calculations are in agreement with the experimental work on precipitation in quenched or irradiated A1-Si alloys.

V. ACCOMPLISHMENTS AND STATUS

A. The Effect of Irradiation on the Nucleation of Incoherent Si Precipitates in A1-Si Alloys -- M.R. Mruzik (M.I.T.) and K.C. Russell (M.I.T.)

1. Introduction

The relative stability of various atomic structures can be drastically disrupted by the energy and mass fluxes characteristic of neutron, electron, or heavy ion bombardment[1-3].

A theory[4-6] of the phase stability of incoherent precipitates under irradiation was recently developed, which may be applied to precipitate nucleation. The complete mathematical model consists of a system of first order differential equations describing the time dependent concentrations of precipitates of all sizes and excess vacancy contents. Although no simple analytic solution exists, an exact determination of this system has been accomplished in this paper by numerical techniques using materials parameters appropriate for dilute A1-Si alloys. Recent experimental studies[3,7] of these alloys provide a convenient basis for a comparison of results.

2. Numerical Computation

A system of first order differential equations is generated by writing $\partial\rho/\partial t$ (where ρ=precipitate number density) for every precipitate size class (n,x) (n = excess vacancies, x = solute atoms) in some region of interest. Density variations between adjacent size classes are so large that using an average value for even a small sub-region is not practical. The region in (n,x) space necessary to accurately determine steady state nucleation rates was chosen so that all size classes lving outside a rectangular area have zero densities. Reflecting boundary conditions, which prevent any net migrating of precipitates across the

boundary, have been applied on three sides. The location of the remaining boundary is chosen to maximize the area in (n,x) space and to include the critical sized (n^*,x^*) precipitate. Mass transport across this absorbing boundary occurs in only one direction (i.e. to larger x). The usual double subscript (n,x) identifing each size class may be replaced with a single monotonically increasing integer $i = n+(x-1)(n_m+1)$, where n_m and x_m are the maximum values of n and x respectively in the region of interest. Using vector notation, our system of equations may thus be written as $\partial\tilde{\rho}/\partial t = A\tilde{\rho}$ where $\tilde{\rho} = \{\rho_1, \rho_2, \ldots \rho_{i_{max}}\}^T$, A is a banded $(i_{max} \times i_{max})$ matrix whose components are functions of the capture and emission rates $(\beta_v, \beta_x, \alpha_v, \alpha_x)$, and $i_{max} = (n_m+1)x_m-1$ is the total number of size classes considered.

Although computer storage requirements require an $i_{max} \lesssim 1500$, several computations using different size regions of (n,x) space gave nearly identical nucleation rates. Region size is thus not *of* crucial importance. This is not surprising since the ratio of the largest values of ρ_i to those along the reflecting boundary approached one googol and since the critical size class (n^*,x^*) was always included in the region.

By establishing fixed concentrations of vacancies C_v and solute atoms C_x, the steady state densities (and nucleation rates) may be obtained by solving $A'\tilde{\rho} = \tilde{c}$. In this expression A' has been modified to eliminate those components involving the densities $\rho(0,1) = C_x/\Omega_m$ and $\rho(1,0) = C_v/\Omega_m$ which constitute the only non-zero components of the vector $\tilde{c}$. The corresponding free energies are simply $\Delta G(0,1) = -k_B T \ln C_x$ and $\Delta G(1,0) = -k_B T \ln C_v$. Sparse matrix techniques permitted an exact solution of $\partial\tilde{\rho}/\partial t = A\tilde{\rho}$ by first factoring A' into upper and lower triangular matrices and then obtaining $\tilde{\rho}$ by recursion. The error of these steps was negligible as verified by monitoring the residuals $\tilde{\rho}$. The steady state nucleation rate is simply the calculated value of J_x which is now independent of x.

3. Results

An advantage of the model is versatility in that additional mechanisms such as interstitial capture or radiation dissolution may be easily included. The effect of interstitial capture on steady state nucleation is illustrated in Fig. (1) for Si precipitates. Increasing the interstitial capture rate β_i decreases the nucleation rate, but with progressively less effect as the ratio β_i/β_v increases from zero. This decrease is seen to be minor compared to the enhancement due to the excess vacancies. As β_i/β_v approaches unity, the nucleation rate must approach zero and this latter decline is relatively precipitous for $\beta_i/\beta_v \gtrsim 0.99$. The catastrophic enhancement effect (factors of 10^{50}) of excess vacancies, however, remains over the entire range of β_i/β_v.

In general, nucleation is enhanced for larger supersaturations and, all else being equal, increased temperature. At a constant damage rate and composition, however, the enhancement caused by a temperature increase may be overwhelmed by the commensurate decrease of solute and vacancy supersaturation.

Experimental difficulties, which limit the accurate measurement and even observation of many nucleation related phenomena, frustrate a complete comparison with our highly quantitive theoretical predictions. In general, the experimental work provides steady state precipitate densities as a function of sample preparation; but not early time kinetic data nor microscopic information on the actual nucleation process. For example, experimental observations tend to report highly non-spherical (rod shaped) precipitates which are dictated mostly at long times by interfacial attachment kinetics and not the spherical forms which are the rule at the nucleation stage where thermodynamics dominates. The experiments [3] do conform with the theoretical model, however, to the extent that precipitates are only observed under those circumstances where nucleation is theoretically predicted by this model on the laboratory time scale.

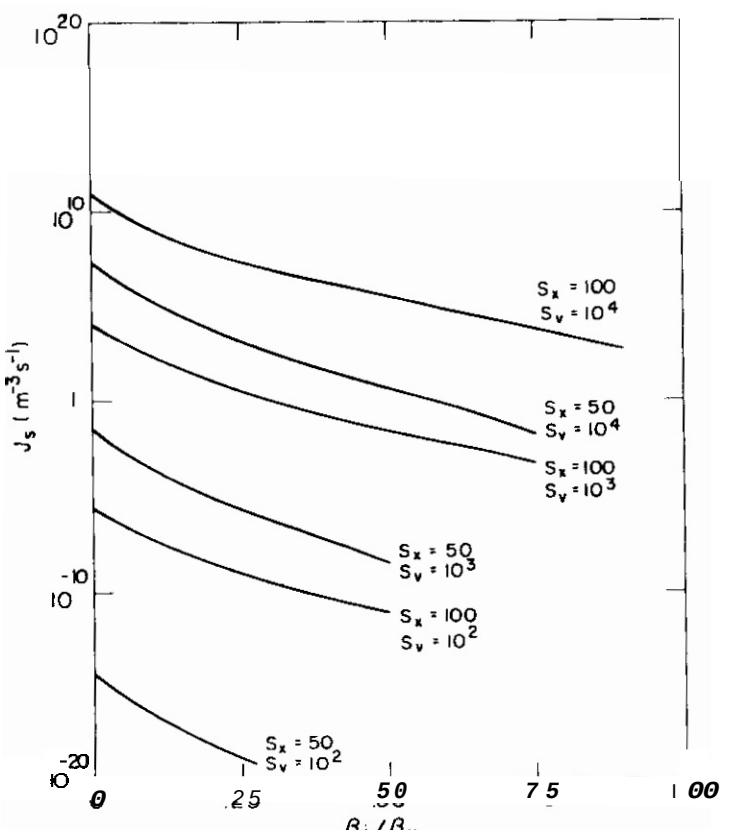

FIGURE 1. The Steady State Nucleation Rate $J_s(m^{-3}s^{-1})$ for Si-Al at 25°C as a Function of the Biasing Ratio (β_i/β_v), and Solute and Vacancy Supersaturations.

VI. REFERENCES

1. J. A. Hudson, British Nucl. Energy Soc., 14, 127 (1975).

2. H. Kahkonen, V. Viljanen, and J. Kulmala, J. Mat. Sci., 11, 1762 (1976).

3. K. Bertram, F. J. Minter, J. A. Hudson, and K. C. Russell, submitted to J. Nucl. Mat.

4. K. C. Russell, Scripta Met. 3, 313 (1969).

5. K. C. Russell. KTG/BNES Conference on Irradiation Behavior of Fuel Cladding'and Core Component Materials, Karlsruhe, Germany, p. 95 (1974)

6. S. I. Maydet and K. C. Russell, J. Nucl. Mat., 64, 101 (1977).

7. N. Kontoneon et al, J. Nucl. Mat., 54, 2b5 (1974).

8. C.J. Smithells, "Metals Reference Book", (Plenum Press, New York, 1967).

9. W. B. Pearson, "Handbood of Lattice Spacings", (Pergamon Press, New York, 1958).

10. B. von Guerard, H. Peisl, and R. Zitzmann, Appl. Phys., 3, 37 (1974).

11. M. Hansen, "Constitution of Binary Alloys", (McGraw-Hill, New York, 1958).

12. J. F. Freedman and A. S. Nowich, Acta Met., 6, 176 (1958).

13. T. S. Lundy and J.F. Murdock, J. Appl. Phys., 33, 1671, (1962); F. Y. Fradin and T. J. Rowland, Appl. Phys. Letters, 11, 2U7 (1967).

14. N. L. Peterson and S. J. Rothman, Phys. Rev., B, 1, 3274 (1970).

15. D. Bergner and E. Cyrener, Neue Huette, 18, 356 (1973).

16. H. Wiedersich, J. J. Burton and J. L. Katz, J. Nucl. Mat., 51, 287 (1974)

17. K. C. Russell, Scripta Met., 3, 313 (1969).

18. K. C. Russell, "Nucleation in Solids; Nucleation 111", p. 44, (Marcell Dekker, New York, to be published).

19. A. D. Brailsford and R. Bullough, J. Nucl. Mat., 44, 121 (1972)

20. R. W. Powell and K. C. Russell, Rad. Eff., 12, 127, (1972).

21. M. R. Mruzik and K. C. Russell, Surface Sci., 67, 205 (1977).

VII. FUTURE WORK

The next step in modelling will be to study the stability of oxide-dispersal strengthened alloys under pulsed irradiation.

VIII. PUBLICATIONS

A paper entitled "The Effect of Irradiation on the Nucleation of Incoherent Precipitates" has been accepted for publication by the Journal of Nuclear Materials.

I. PROGRAM

Title: Effects of Irradiation on Fusion Reactor Materials
Principal Investigator: F. V. Nolfi, Jr.
Affiliation: Argonne National Laboratory

II. OBJECTIVE

The objective of this work is to determine the microstructural evolution, during irradiation, of first-wall materials with special emphasis on the effects of helium production, displacement damage and rates, and temperature.

III. RELEVANT DAFS PROGRAM PLAN TASK/SUBTASK

SUBTASK II.C.2.1 Mobility, Distribution, and Bubble Nucleation

IV. SUMMARY

Single and dual-ion irradiations of an Fe-20Ni-15Cr ternary alloy, a V-15Cr binary alloy, and selected Ti alloys (Ti-64, Ti-811, and Ti-15333) have been performed over a range of doses, helium to dpa ratios, and temperatures. For the Fe-20Ni-15Cr alloy, a dose dependence study at 700°C revealed that specimens injected with helium at a rate of 50:1 (appm He: dpa) exhibited less swelling than specimens injected at 15:1, and that this lower swelling is associated with higher cavity number densities and decreased cavity growth rates. Furthermore, the simultaneous injection of helium did not cause a significant change in the peak swelling temperature of this alloy but did tend to inhibit cavity growth at higher temperatures.

A dose dependence study (5-55 dpa) on the V-15Cr alloy at 650° revealed ~20% void swelling at 55 dpa with void diameters approaching 900 Å. No irradiation-induced precipitation occurred at any of the doses, but considerable solute (Cr) enrichment near the surface (~50%) was observed by

Auger spectroscopy. The depth of Cr redistribution was ~1000 Å, which is too deep to be Gibbsian in nature. These results suggest that Cr segregates to defect sinks during irradiation and provide the first experimental evidence of irradiation-induced solute segregation in bcc alloys.

V. ACCOMPLISHMENTS AND STATUS

Microstructure of Irradiated Fusion Reactor First-wall Materials -- S. C. Agarwal and G. Ayrault

1. Introduction

One of the major problems in the development of structural alloys for use in fusion reactors (FR) is the lack of suitable materials-testing facilities. This obtains because operating fusion reactors, even of the experimental size, do not exist. A primary task in the early stages of FR alloy development will be to adapt currently available irradiation facilities for use in materials development. Thus, it is generally recognized that, at least for the next several years, studies of irradiation effects in an FR environment on the microstructure and mechanical properties of structural materials must utilize ion and fission-neutron simulations. Special problems will arise because, in addition to displacement damage, an FR-radiation envircnment will produce, in candidate structural materials, higher and more significant concentrations of gaseous nuclear transmutation products (e.g., helium and hydrogen) than found in a fast-breeder reactor. These effects must be taken into account when simulation techniques are employed, since they impact heavily upon irradiation microstructure development and, hence, mechanical properties.

2. Results and Discussion

In order to study the effects on microstructure of radiation damage and simultaneous displacement damage and helium production that will occur in structural materials in FRs, the following investigations were

performed.

A. Dual-ion Irradiation of an Fe-15Cr-20Ni Alloy

Annealed specimens of this experimental austenitic alloy were irradiated simultaneously with a **3.0-MeV** $^{58}Ni^{+}$ beam and a degraded 0.95-MeV $^{3}He^{+}$ beam at the ANL Dual-ion Irradiation Facility, Fig. 1, and subsequently examined by transmission electron microscopy (TEM). Nominal dose levels ranged from 3-25 dpa, the dose rate was $\sim 3 \times 10^{-3}$ dpa·s^{-1}, the irradiation temperature was 700°C, and the nominal He(appm):dpa ratios were 5:1, 15:1, and 50:1 (a 15:1 He:dpa ratio *is* considered typical for FR operation). For comparative studies, specimens preinjected at room temperature with 15 appm He and irradiated only with Ni ions were also included. The doses and irradiation temperatures were the same as above. A temperature dependence study was also carried out in the range 600-800°C in order to determine any shift in the swelling peak associated with the high helium levels. For this study, the dose and He:dpa ratio were held constant at 12 dpa and 15:1, respectively.

From the temperature dependence study, peaks in both the swelling curve and cavity size were observed to occur at ~650°C indicating an apparent weak effect of helium on the swelling peak temperatures, Fig. 2 (the peak swelling temperature for this alloy is ~700°C[1] when preinjected with 15 appm He and Ni-ion-irradiated at 10^{-2} dpa·s^{-1}). Both the cavity number density and dislocation density decrease with increasing temperature and show a plateau in the vicinity of the peak swelling temperature, Fig. 3. In the dose dependence study, a strong dependence of cavity microstructure on He:dpa ratio was observed, Fig. 4. A bimodal size distribution of cavities was found to persist to ~25 dpa in the 50:1 specimens and to ~6 dpa in the 15:1 specimens. For both He:dpa ratios, the cavity number density decreased with increasing dose, Fig. 5, and was generally higher for the 50:1 He:dpa ratio. In contrast, the dislocation density was nearly independent of dose and He:dpa ratio, Fig. 6. This study also showed that up to ~6 dpa, the swelling is comparable for both

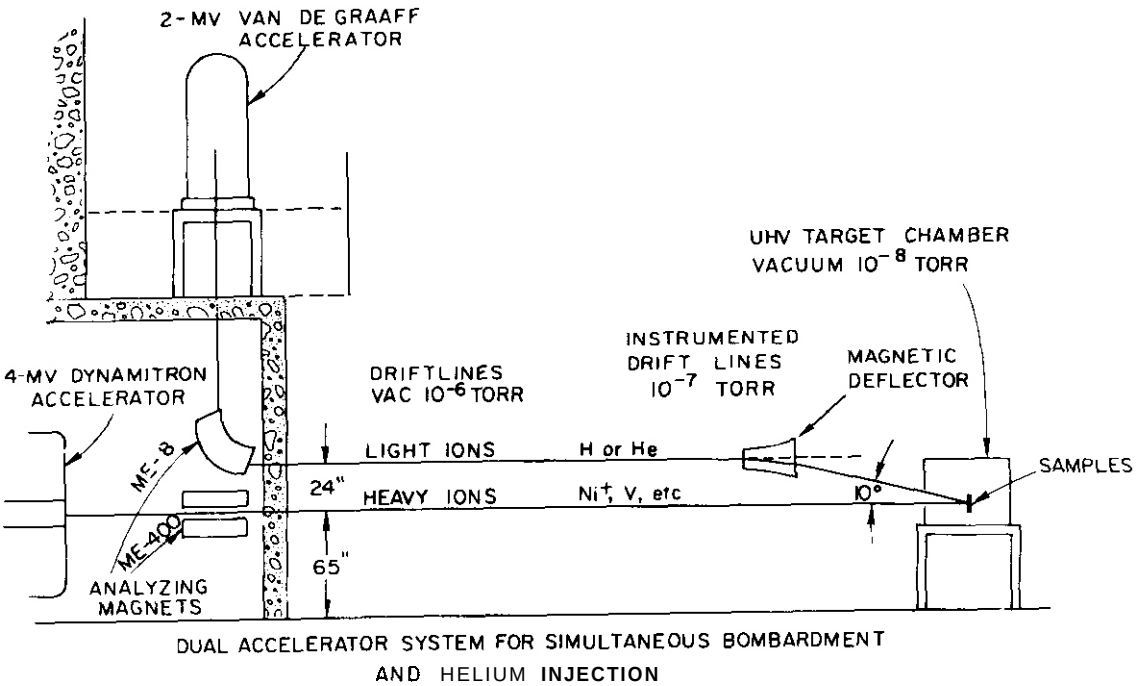

FIGURE 1. Schematic of ANL Dual-Ion Irradiation System.

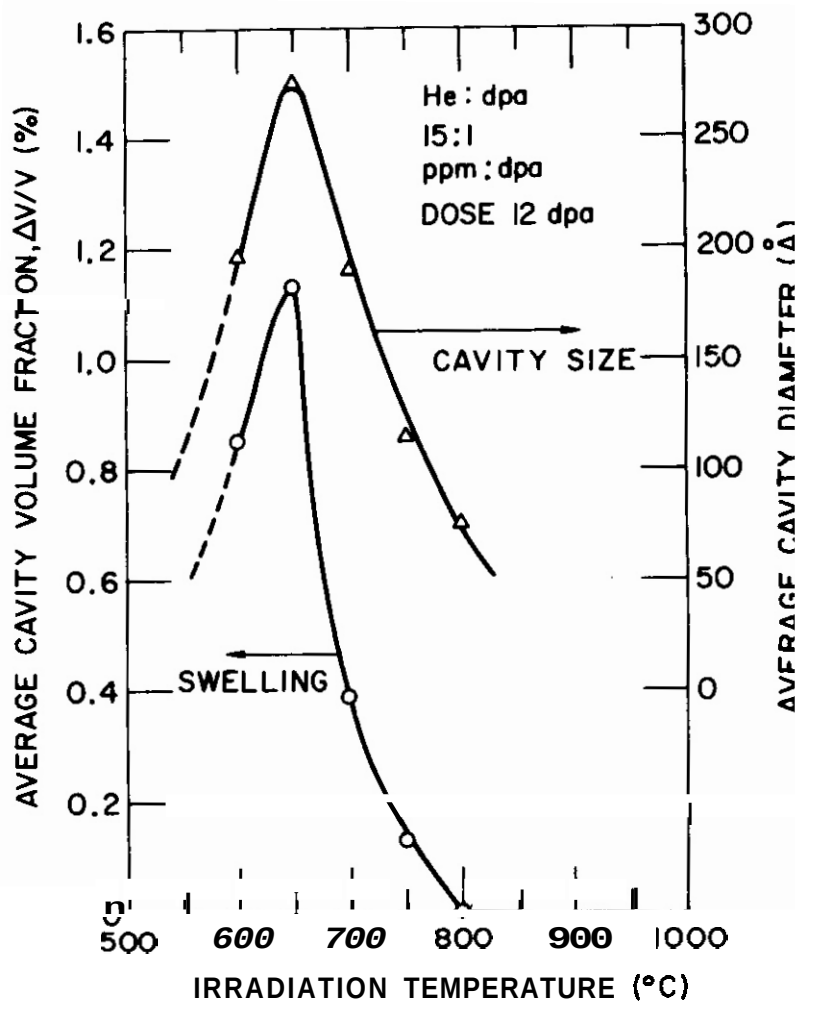

FIGURE 2. Temperature dependence of swelling and cavity size in Fe-20Ni-15Cr (dose rate = 3 x 10^{-3} dpa·s^{-1}).

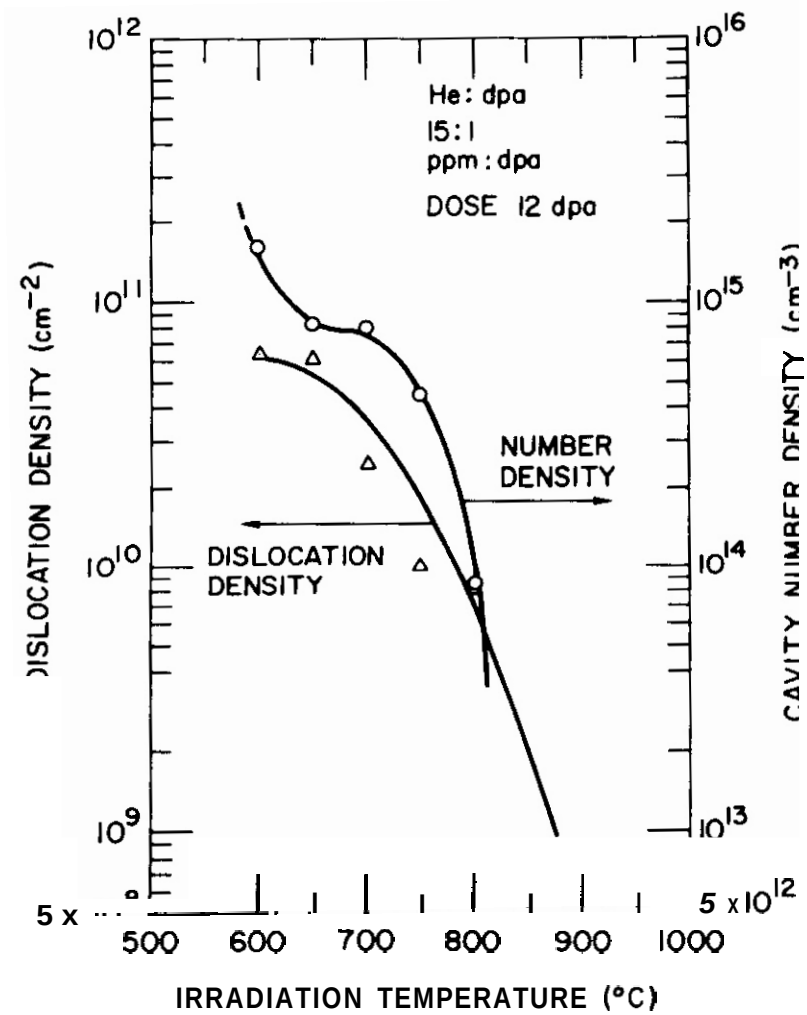

FIGURE 3. Temperature dependence of the dislocation and cavity number densities in Fe-20Ni-15Cr [dose rate = 3 x 10^{-3} dpa·s^{-1}).

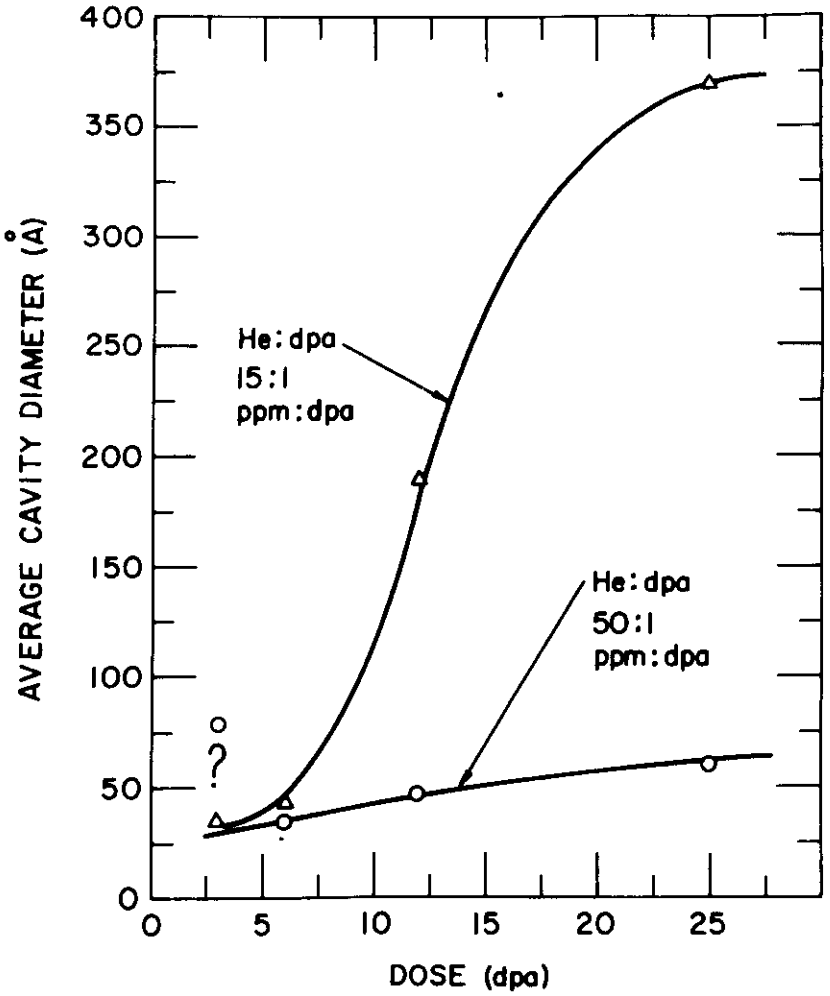

FIGURE 4. Dose dependence of cavity size in Fe-20Ni-15Cr (dose rate = 3×10^{-3} dpa•s^{-1} temperature - 700°C).

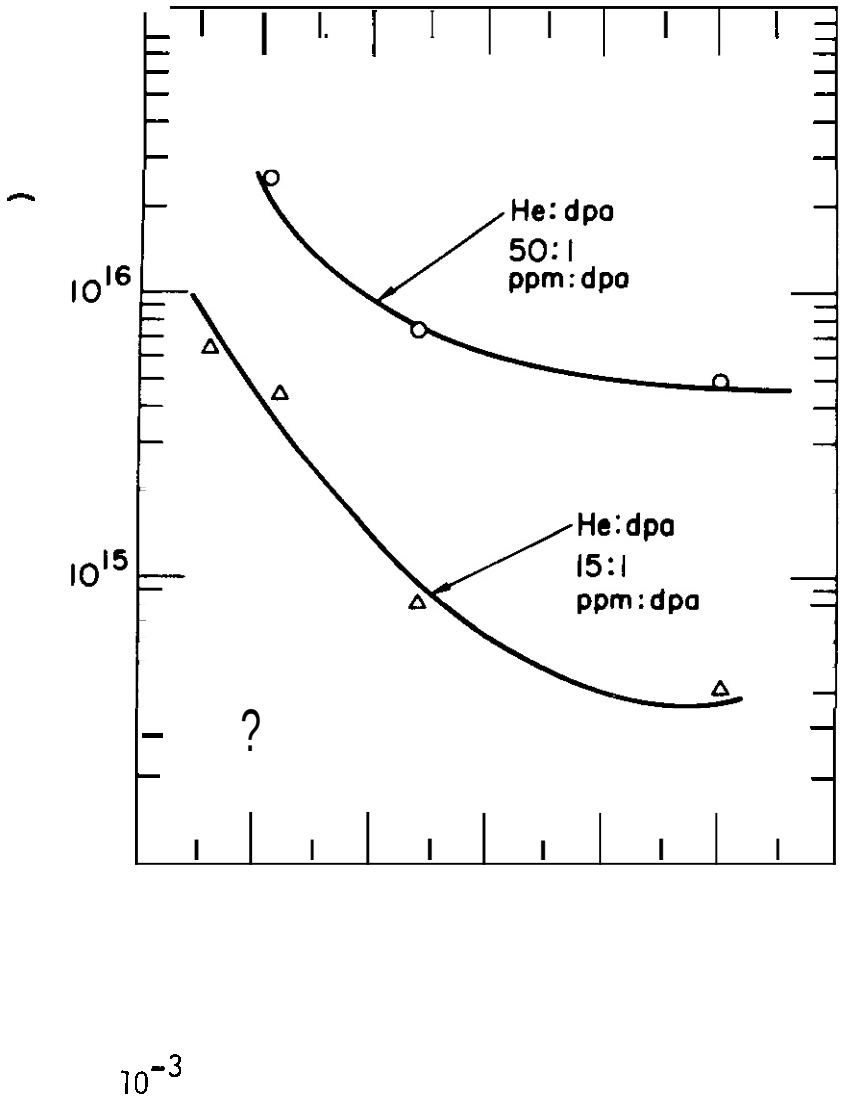
He: dpa
50:1
ppm: dpa
He: dpa
15:1
ppm: dpa
10^{16}
10^{15}
?
10^{-3}

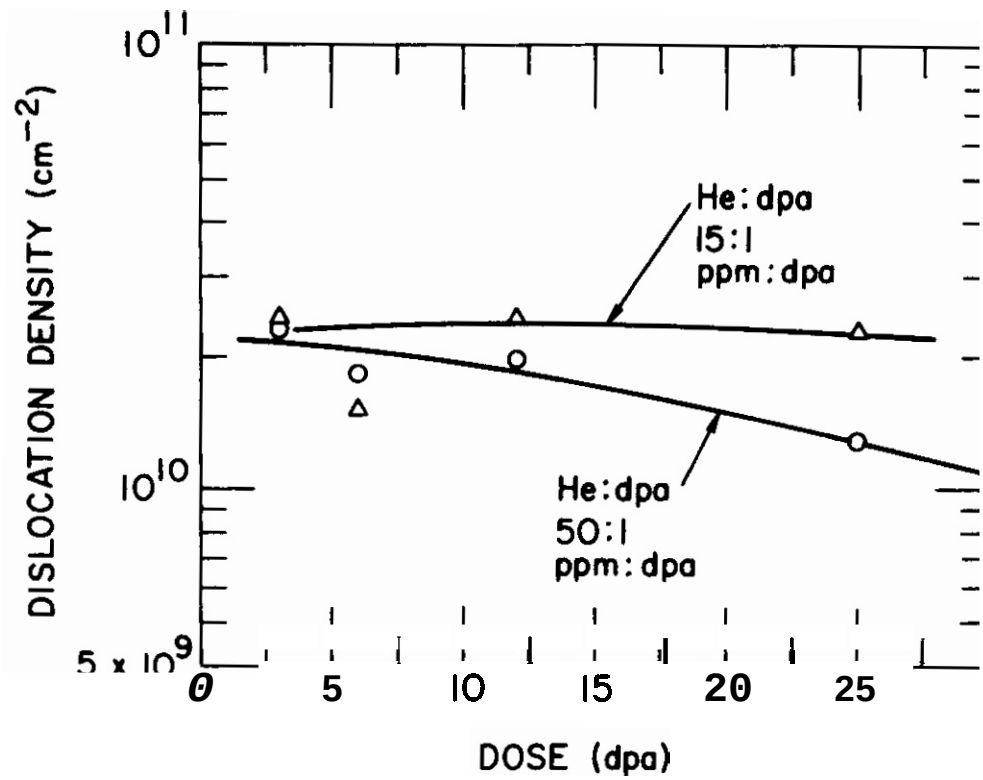

FIGURE 6. Dose dependence of dislocation density in Fe-20Ni-15Cr (dose rate = 3×10^{-3} dpa·s^{-1}, temperature = 700°C).

V. ACCOMPLISHMENTS AND STATUS

A. Transport Theoretical Studies of Damage Production -- T. J. Hoffman (UCCND Computer Sciences Division), H. L. Dodds, Jr. (University of Tennessee, Knoxville), M. T. Robinson (ORNL), and O. K. Holmes (ORNL)

In previous research,[1] it was shown that the neutral particle discrete ordinates computer code ANISN could be used to calculate sputtering yields if provided with a suitable multigroup cross section table to describe the relevant atomic scattering problems. No modifications to ANISN itself were required to treat charged particle transport. Instead, the total macroscopic cross section was modified to account for electronic excitations and small-scattering-angle elastic interactions. The cross section table was based on the well-known approximate treatment of atomic scattering of Lindhard and his co-workers[2] with low energy modifications as given by Sigmund.[3]

Although the one-dimensional ANISN code was sufficient for the sputtering problems investigated before, most applications of transport theory must use two- or even three-dimensional models. For example, the cylindrical symetry of a collision cascade in an amorphous medium requires two-dimensional calculations. These may be accomplished using the two-dimensional discrete ordinates code DOT.[4] The three-dimensional Monte Carlo transport code MORSE[5] also uses the same kind of cross section tables as do ANISN and DOT. The applicability of these codes to particle range and energy deposition calculations is being explored. They have the potentiality of supplying superior replacements for existing codes such as E-DEP-1.[6]

Both ANISN and MORSE have been used to calculate range distributions for 100-keV ^{196}Au atoms recoiling in Au. This case is of interest because of available calculations using the atomistic code MARLOWE and also because experimental data are available.[7] The ANISN and MORSE mean

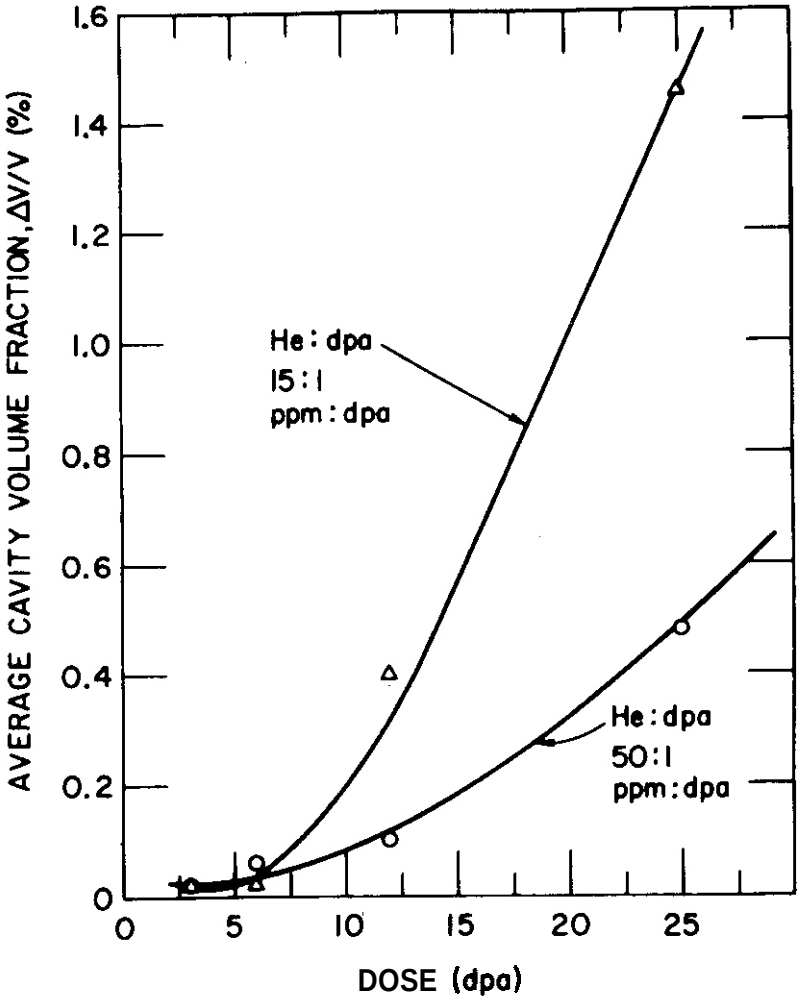

FIGURE 7. **Dose dependence of swelling in Fe-20Ni-15Cr** (dose rate = 3 x 10^{-3} dpa·s^{-1}, temperature = 700°C).

Transmission-electron micrographs of the void population obtained under absorption contrast conditions in samples irradiated at 650°C to peak doses of 5, 15, 30, and 60 dpa are shown in Fig. 8. A strong increase in void size occurs with an increase in dose, but no obvious change in number density is apparent. Control samples that were shielded from the ion beam were also mounted in the irradiation rig to ensure the same thermal history as the irradiated samples. Micrographs showed that the control samples were very clean and were characterized by a low dislocation density ($\sim 10^8$ cm^{-2}).

The effect of dose on the dislocation microstructure, imaged under two-beam conditions using a {110} diffracted beam in an {001} foil, is shown in Fig. 9. An interconnected cellular dislocation structure is observed at 5 dpa, which coarsens and stabilizes by ~27 dpa. Regions of lower dislocation density appear to contain the majority of the voids. This correlation is more clearly demonstrated in Fig. 10. The upper micrograph shows an area in the 27-dpa specimen imaged under strong dislocation contrast conditions, and the lower micrograph shows the same area under absorption contrast conditions to enhance the visibility of the void microstructure.

Quantitative verification of the general swelling behavior presented in Figs. 9 and 10 was also obtained. Figure 11 'gives the measured average void diameter as a function of irradiation dose at 650°C. The average void diameter increases linearly with dose, from ~75 Å at 5 dpa to more than 900 Å at 55 dpa. The void-number density and total swelling ($\Delta V/V$) are plotted as a function of dose in Fig. 12. Although only a slight increase in number density occurs between 5 and 55 dpa, the large increase in void size over this damage regime results in a dramatic increase in total swelling. A correction is included in the calculated total swelling results to account for the voids that intersect the foil surface. Since the foil thickness varies between 1000 and 2000 Å, this correction is insignificant at the lower doses. However, at 55 dpa the foil thickness (1200 Å) and void size (900 Å) are comparable, and this introduces a large

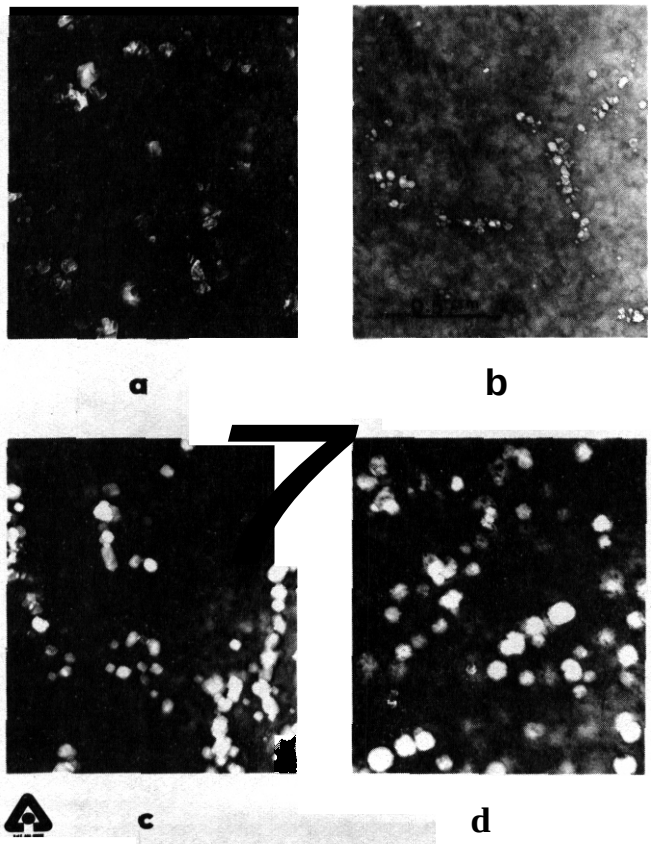

FIGURE 8. Absorption contrast micrographs of V-15Cr specimens irradiated at 650°C to different dose levels. (a) 5 dpa, (b) 11 dpa, (c) 27 dpa, and (d) 55 dpa.

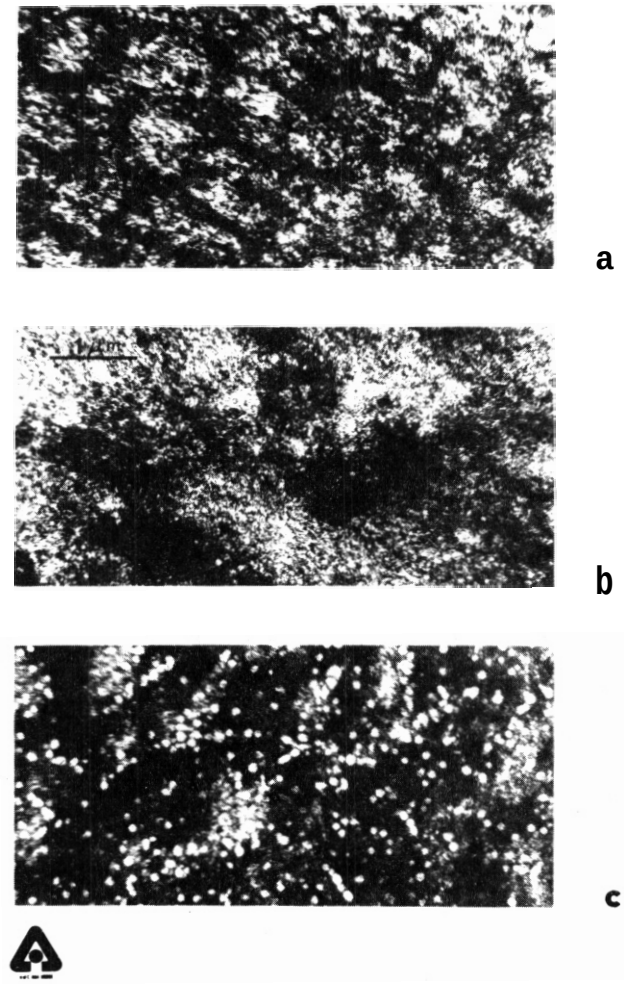

FIGURE 9. Dislocation contrast micrographs of V-15Cr specimens irradiated at 650°C to different dose levels. (a) 5 dpa, (b) 27 dpa, and (c) 55 dpa.

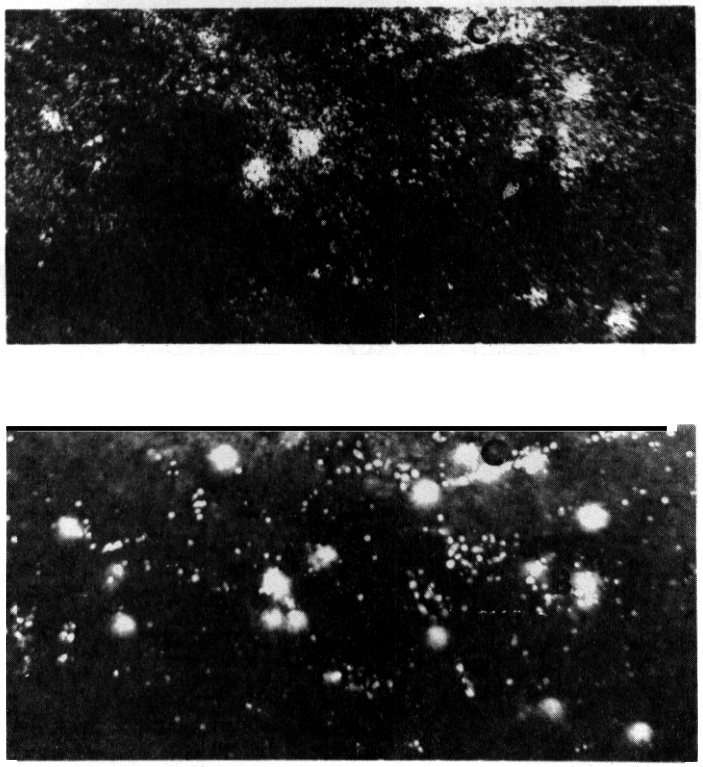

FIGURE 10. The same area of the 27-dpa specimen shown in Figure 2 imaged under strong dislocation contrast (upper micrograph) and absorption contrast (lower micrograph).

sensitivity to the choice of interatomic potential, using two computational methods.

Atomistic computer simulations of radiation damage production have been performed by the dynamical method,[11,12] the binary collision method,[13,14] and the quasi-dynamical method.[15,16] From a calculational point of view, the dynamical method, which incorporates a many-body treatment, is ideally suited to the analysis of low energy cascades, in general, and replacement sequences, in particular. However, this method requires considerable computer memory and relatively long run times, making computation expensive. The binary collision method, as its name suggests, considers only single interactions between individual pairs of atoms at any specific time during the evolution of a sequence. Although such calculations are very fast, they cannot accurately simulate replacement sequences which require consideration of many relatively weak forces arising from multiple simultaneous interactions.[17] The quasi-dynamical method is intended *to* combine much of the accuracy and realism of the dynamical method with the speed and economy of the binary collision method. The quasi-dynamical method consists of a restricted many-body treatment with various calculational parameters which may be set *so* as to approximate the dynamical method as closely as desired. The key to efficient application of this method lies in setting the calculational parameters in a optimum way, i.e., so as to yield acceptable accuracy at reasonably high computational speeds.

The procedure followed in this study consists of using a dynamical code, COMENT,[12] to characterize the expected behavior for a given initial PKA momentum vector and a particular choice of interatomic potential function. Parameters are adjusted in the quasi-dynamical code ADDES[16] to obtain both acceptable agreement between the two methods and *to* establish a relative accuracy for the quasi-dynamical method. ADDES is then employed to economically characterize the behavior of the three well-established types of fcc replacement sequences (<110>, <100>, <111>) over a wide range of energies and angular deviations, thus establishing theoretical bounds on replacement sequence behavior.

degree of accuracy in a usually simple interatomic potential function. At

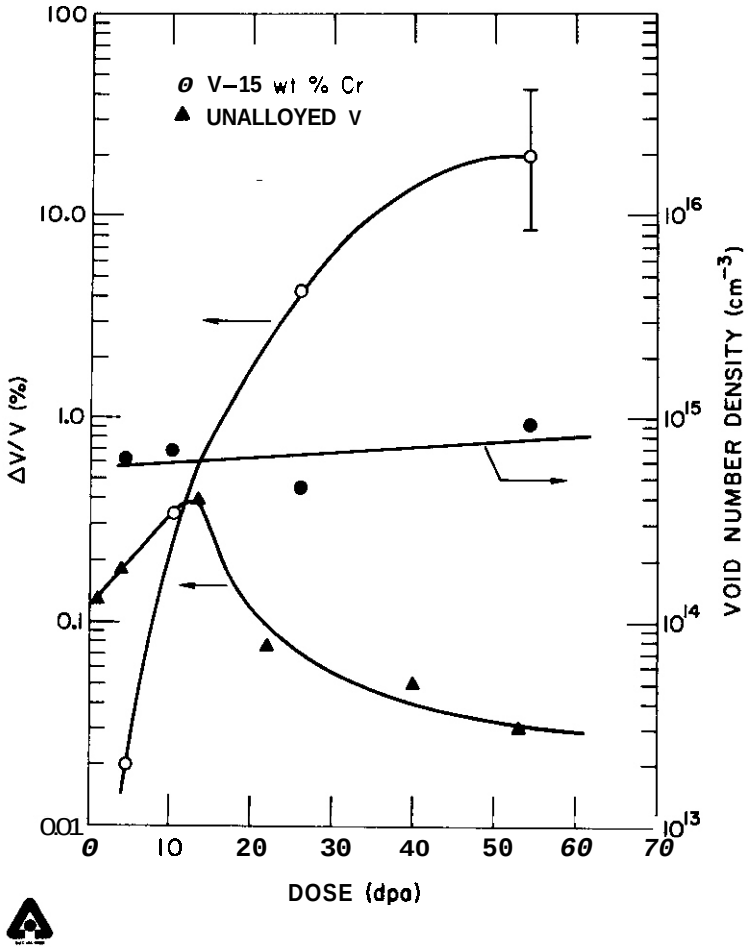

FIGURE 12. Void number density and calculated total swelling for V-15Cr as a function of total dose. The total swelling of the unalloyed V stock is also shown.

correction for surface voids. The computed swelling at this dose, including the correction (upper limit), is 42%; without the correction, the value of total swelling at 55 dpa is 8.5% (lower limit) so that we estimate the actual swelling to be ~20% at this dose.

Figure 12 also shows the swelling curve for the unalloyed V of the same stock irradiated under essentially identical conditions in a previous study.[2] In unalloyed V, the swelling initially increases with dose to a peak value of ~0.4% at ~14 dpa, and then decreases as the dose increases. This decrease in swelling at higher doses is accompanied by an increasingly high density of irradiation-induced coherent {012}-type precipitates. These precipitates appear to be associated with the presence of interstitial impurities (C, O, and N).[3]

Work on the temperature dependence of the single-ion and dual-ion irradiated specimens of V-15Cr is in progress.

Auger spectroscopy measurements on this V-15Cr alloy have been performed by L. E. Rehn under Basic Energy Sciences (BES) funding and are reported here because of their significance with respect to radiation effects in V alloys. Auger studies of the surface of irradiated and unirradiated specimens showed that Cr segregates to the surface (and presumably to other point-defect sinks) during irradiation. The Cr concentration near the surface was ~45% after 15 dpa, which is a factor of three larger than the average concentration in the bulk (~15%), Fig. 13. Profiling of the segregation by sputtering away surface layers showed a subsurface region reduced in Cr concentration and a return to essentially bulk value at a depth of ~1000 Å from the original surface. This depth is too large for the segregation to have been Gibbsian in nature and suggests irradiation-induced segregation.

Cr is undersized in V and causes a fractional change in lattice parameter per atom fraction of solute equal to -6%.[4] The observed enrichment of Cr at the surface, which serves as a sink for both intersitital- and

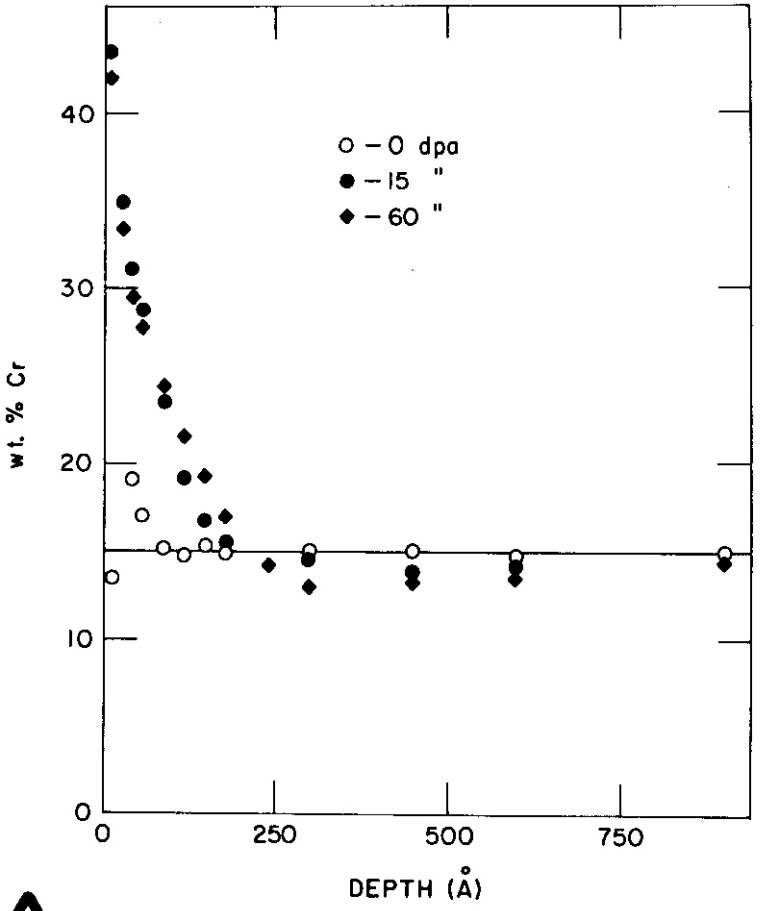

FIGURE 13. Cr concentration vs. depth profiles for an unirradiated control (0 dpa) and two irradiated specimens (15 and 60 dpa peak dose).

vacancy-type defects, is therefore consistent with the size-effect prediction of Okamoto and Wiedersich.[5] Similar measurements at our Laboratory on V-ion-irradiated V-4Si also show enrichment of the undersize Si atoms at the surface. An attempt to profile the oversize solute Ti in a V-10Ti alloy was not successful because of interference between the Ti, V, and N Auger transitions. However, the surface enrichment of Cr and Si in V indicates that the sign of the solute misfit parameter may determine the direction of substitutional solute segregation during irradiation at elevated temperatures in binary alloys of body-centered-cubic (bcc) V as well as in fcc Ni.[6] The results of the present work suggest the following conclusions:

(a) The swelling in V-15Cr increases rapidly with dose at 610°C and is much greater than for unalloyed V at high doses; no precipitation at any dose is observed in V-15Cr. These observations are consistent with the thesis that refractory alloys tend to be low swelling because of a general propensity toward precipitation during irradiation.

(b) The present results show that Cr atoms move toward defect sinks during irradiation of V-15Cr and provide the first direct experimental evidence for irradiation-induced segregation of substitutional solute atoms in a bcc alloy.

C. Radiation Damage in Commercial Ti-base Alloys (in collaboration with McDonnel-Douglas Astronautics Corporation)

Titanium alloys have been suggested as candidate materials for Frs. However, information regarding their response to displacement producing radiation is sparse and nonexistent for concurrent high helium production. Three common Ti-base commercial alloys, Ti-64 (6 wt % Al - 4 wt % V), Ti-811 (8 wt % Al - 1 wt % Mo - 1 wt % V) and Ti-15333 (15 wt % V - 3 wt % Cr - 3 wt % Al - 3 wt % Sn) were irradiated with 2.4-MeV $^{51}V^{+}$ ions, and also dual-ion irradiated with V^{+} and 0.95-MeV degraded $^{3}He^{+}$ ions. The irradiation temperatures were 450, 550, and 650°C. For the single-ion irradiations the dose levels ranged from 3 to 25 dpa, and for the dual-ion

irradiations specimens were irradiated to a fixed dose of 25 dpa and 10:1 He:dpa ratio. TEM examination and data analysis of the above alloys are in progress.

D. Helium Implantation and Profiling

During dual-ion irradiations, we use energy degradation of the helium beam to reduce the range and to spread the distribution for proper placement of injected helium in the heavy-ion damaged region. In our initial implants, Brice Code results for ^{3}He incident on nickel were used to calculate energy distributions of the degraded beam as a function of degrader foil thickness and incident ion energy. The implant distribution was measured during each dual ion run using stainless steel-copper calibration strips of variable thickness. These strips were implanted with ^{3}He, and the ^{3}He(d,p)^{4}He reaction was used to determine total ^{3}He concentrations during subsequent deuteron bombardment. In these initial implants, the helium was found to be substantially shallower and at a much lower concentration than expected. Subsequent examination of the data and calculations indicated that, because of inaccurate stopping powers used in the Brice Codes, the ^{3}He ranges in nickel were overestimated. Subsequent dual-ion experiments were performed using a thinner degrader foil, and the proper ^{3}He energy was confirmed by energy analysis of the degraded ^{3}He using Rutherford backscattering from a gold thin film (the ion-beam analysis techniques reported here were developed by K. S. Grabowski under BES funding).

VI. REFERENCES

1. W. G. Johnston, T. Lauritzen, J. H. Rosolowski, and A. M. Turkalo, "The Effect of Metallurgical Variables on Void Swelling," General Electric Corporate Research and Development Report 76CRD019, Schenectady, NY, 1976.

2. S. C. Agarwal and A. Taylor, Proc. Intl. Conf. on "Radiation Effects and Tritium Technology for Fusion Reactors," Vol. I, 150, 1975.

3. S. C. Agarwal, D. I. Potter and A. Taylor, ASTM STP 611, p. 298 (1976).

4. O. N. Carlson and A. L. Eustice, USAEC IS-47, (1959).

5. P. R. Okamoto and H. Wiedersich, J. Nucl. Mater. 53, p. 336 (1974).

6. D. I. Potter, L. E. Rehn, P. R. Okamoto and H. Wiedersich, Proc. Intl. Conf. on "Radiation Effects in Breeder Reactor Structural Materials," M. B. Bleiberg and J. W. Bennett, eds., pp. 377-386, Metallurgical Society of AIME, New York, 1977.

VII. FUTURE WORK

1. TEM examinations of dual-ion and single-ion irradiated Fe-20Ni-15Cr specimens are in progress [dose dependence studies of samples irradiated at 700°C with (a) 5:1 He:dpa ratio and (b) preinjected with 15 appm He].

2. TEM examinations of single- and dual-ion irradiated V-15Cr alloy are in progress [temperature dependence studies (450-650°C) at a dose of 25 dpa, and 10:1 He:dpa ratio for the dual-ion irradiated samples].

3. TEM examinations of the Ti alloys are in progress.

4. Low-dose rate (3×10^{-4} dpa·s^{-1}) dual-ion irradiations (15:1 He: dpa ratio) of Fe-20Ni-15Cr samples to doses of ~15 dpa have been scheduled].

5. Dual-ion irradiations of Type 316 stainless steel (MFE reference heat) have been scheduled for dose and temperature dependence studies of microstructural evolution. These studies will be similar to those reported here for the Fe-20Ni-15Cr alloy.

VIII. PUBLICATIONS

S. C. Agarwal, D. I. Potter, and A. Taylor, "Effects of Oxygen Additions on the Void Swelling Behavior of Vanadium" Met. Trans. A,

in press.

S. C. Agarwal, D. I. Potter, and A. Taylor, "Void Swelling in V-Ion-Irradiated V-O Alloys," Trans. ANS 26, pp. 184-185, 1977.

S. C. Agarwal, A. Taylor, and F. V. Nolfi, Jr., "Swelling in Dual-ion Irradiated Fe-15Cr-20Ni Alloy," Trans. ANS 27, pp. 269-271, 1977.

Barbara Ukray Hall and Hartmut Wiedersich, "Effect of Trapping and Detrapping of Helium on Void Nucleation," AIME Intl. Conf. on "Radiation Effects in Breeder Reactor Structural Materials," pp. 387-394, 1977.

R. F. Mattas, H. Wiedersich, D. G. Atteridge, A. B. Johnson and J. F. Remark, "Elevated-temperature Tensile Properties of V-15Cr-5Ti Containing Helium Introduced by Ion Bombardment and Tritium Decay," Proc. Second ANS Topical Meeting on "Technology of Controlled Thermonuclear Fusion," CONF-760935-P1, pp. 199-208, 1977.

F. V. Nolfi, Jr., A. Taylor, D. I. Potter, S. C. Agarwal and B. Okray Hall, "The Application of Dual-ion Irradiations to Fusion Materials Problems," Trans. ANS 26, p. 190, 1977.

F. V. Nolfi, Jr., "Radiation Damage in Fusion Reactor Materials," Yearbook of Science and Technology, McGraw-Hill, 1977.

F. U. Nolfi, Jr. and Che-Yu Li, "The Application of Simulation Experiments to Fusion Materials Development," Nuclear Technology, in press.

Hartmut Wiedersich and Barbara Okray Hall, "Effect of Mobile Helium on Void Nucleation," J. Nucl. Mater. 66, p. 187, 1977.

S. C. Agarwal, L. E. Rehn, and F. V. Nolfi, Jr., "Irradiation-induced Void Swelling and Solute Segregation in a V-Ion-Irradiated V-15 wt % Cr BCC Alloy," submitted to J. Nucl. Mater. for possible publication.

I. PROGRAM

Title: Irradiation Response of Materials
Principal Investigators: J. A. Spitznagel, W. J. Choyke
Affiliation: Westinghouse Research and Development Center

II. OBJECTIVE

The objective of this work is to assess the phenomenology and mechanisms of microstructural evolution in materials exposed to simultaneous helium injection and creation of atomic displacement damage by a second ion beam.

III. RELEVANT DAFS PROGRAM PLAN TASK/SUBTASK

SUBTASK II.C.2.1 Helium Mobility, Distribution and Bubble Nucleation

IV. SUMMARY

The effects of momentum transfer, detrapping and radiation-enhanced diffusion of helium in various materials can be studied using the elastic scattering of high energy alpha particles.[1,2,3] Experiments scheduled to start in the next reporting period will focus on characterizing helium distributions in ion bombarded b.c.c. metals using this technique.

V. ACCOMPLISHMENTS AND STATUS

Work is scheduled to start in June FY-78.

VI. REFERENCES

1. A. G. Pieper and R. 8. Theus, NRL Memorandum Report 2555, p. 38 (1973).

2. L. Shabason and W. J. Choyke, Nucl. Instr. and Methods, 137, p. 533 (1976).

3. W. J. Choyke, J. A. Spitznagel, J. N. McGruer and J. S. Lally, "Momentum Transfer and Damage Energy Gradient Effects on Helium Distributions in Type 304 Stainless Steel," Accepted for Publication in J. Nucl. Mater. (1978).

VII. FUTURE WORK

Specimens of Mo and V suitable for alpha-alpha scattering measurements using 18 MeV alpha particles will be prepared for helium implantation. Thin foil standards of these metals will be given shallow surface implants to calibrate for straggling and multiple scattering effects.

VIII. PUBLICATIONS

None

I. PROGRAM

Title: Effects of Irradiation on Fusion Reactor Materials
Principal Investigator: F. V. Nolfi, Jr.
Affiliation: Argonne National Laboratory

II. OBJECTIVE

The objective of this work is to develop physically based models for microstructural evolution that occurs during simulated fusion reactor irradiation.

III. RELEVANT DAFS PROGRAM PLAN TASK/SUBTASK

SUBTASK II.C.2.4 Modeling

IV. SUMMARY

Calculations of the low-dose ($\lesssim$ 1 dpa) microstructural development have been made for nickel using a time-dependent nucleation and growth model that includes both interstitial and vacancy clustering. These calculations are being compared with experimental data obtained in ion-irradiation studies.

V. ACCOMPLISHMENTS AND STATUS

Microstructural Modeling -- B. Okray Hall

1. Introduction

A comprehensive time-dependent nucleation and growth model that includes dislocation loops, voids, and helium bubbles is being developed to describe the effects of simultaneous helium production and displacement

damage on microstructural evolution in metals. The modeling complements the dual-ion irradiation studies and is designed to aid in interpretation of the experimental results.

2. Results and Discussion

At present, interstitial loop nucleation and growth and void nucleation in the absence of helium have been studied with the time-dependent nucleation and growth model. The calculations, performed using parameters for nickel, show that (1) loop nucleation is essentially complete at very low doses (of the order of $\sim 10^{-4}$ to 10^{-5} dpa) for a wide range of dose rates and temperatures; (2) experimental dependencies of loop number densities on sink-annihilation probability, dose rate, and temperature can be reproduced qualitatively; (3) the formation of vacancy clusters is initially suppressed because the interstitial flux is larger than the vacancy flux until quasi-steady-state is reached; and (4) a bias is not essential for loop nucleation, but is required for void nucleation, which occurs in the quasi-steady-state regime.

In restricted regimes, simplified models, which treat only segments of the full problem, give results in good numerical agreement with those calculated using the complete model. It may be possible, therefore, to parameterize portions of the problem, loop nucleation for example, and extend the model to higher doses and nonzero helium concentrations.

An experiment designed to verify and calibrate the model calculations has been performed in cooperation with D. I. Potter under Basic Energy Sciences funding. Nickel and several nickel alloys have been irradiated with Ni^+ ions to doses ranging from 0.001 to 0.6 dpa. The specimens have been sectioned and examined using transmission electron microscopy and results are currently being compared with model predictions.

VI. REFERENCES

None

VII. FUTURE WORK

The time-dependent model will be expanded to include mobile helium and its effect on vacancy clustering. Parameterization of segments of the model will continue. Impurity effects on loop behavior will be examined.

VIII. PUBLICATIONS

B. Okray Hall and H. Wiedersich, "Effect of Trapping and Detrapping of Helium on Void Nucleation," Proc. Intl. Conf. on "Breeder Reactor Structural Materials," M. L. Bleiberg and J. W. Bennet, eds., pp. 387-394, 1977.

A manuscript, on the time-dependent nucleation and growth model is currently in preparation.

I. PROGRAM

Title: Phase Stability In Irradiated Metals
Principal Investigator: Kenneth C. Russell
Affiliation: Department of Materials Science and Engineering
Massachusettts Institute of Technology

II. OBJECTIVE:

The objective of this work is to model from first principles void nucleation in irradiated metals.

III. RELEVANT OAFS PROGRAM PLAN TASK/SUBTASK

SUBTASK **II.C.2.4** Effects of Helium Microstructure/Modeling

IV. SUMMARY

An atomistics-based theory for void nucleation has been used to calculate - for the first time- terminal void number densities for irradiated type 316 stainless steel and the Ni-base alloy, PE-16. Both the absolute magnitudes. and temperature dependences of the void number densities are in agreement with experiment. The void nucleation parameter, ψ, which governs spontaneous void nucleation was evaluated for the two materials; the results are in agreement with experiment. The critical gas content for rapid void growth was calculated for PE-16 and type 316 stainless steel, and was found to increase from about 10 helium atoms at the lower end of the void swelling range to some 10^4 atoms at the upper end. The theory was also found to predict re-nucleation of a new distribution of voids after a drop in temperature during irradiation.

V. ACCOMPLISHMENTS AND STATUS

A. Numerical Simulation of Void Nucleation in Irradiated Stainless

Steel and Nimonic PE-16 -- S. I. Maydet (M.I.T.) and K.C. Russell (M.I.T.)

1. Introduction

In order that low swelling materials be developed, greater insight into the mechanistics of the swelling process is needed.[1-4] Reactor studies are extremely expensive and often difficult to control to the degree desired, so that various out-of-reactor modelling schemes are desirable. Experimental simulation techniques typically involve bombardment of the material with high energy particles (electrons, protons, self ions, other heavy ions). High effective dose levels (>50 dpa) may be achieved in relatively short time because the defect production rate is about 3 orders of magnitude larger than in-reactor. In that void nucleation under reactor conditions is usually catalyzed by transmutation-produced helium , these simulations often include pre-injection or simultaneous injection of a controlled amount of helium gas by alpha particle bombardment. (4)

Various investigators have concerned themselves with formulating theories of void nucleation based upon the current level of understanding of the radiation damage and nucleation processes, and then testing these theories against observed phenome'na as a measure of their validity. Russell (5) and Katz and Weidersich (6) independently developed the theory of homogeneous nucleaton of voids in the absence of gas atoms. This theory for the co-precipitation of vacancies and interstitials was then extended to include nucleation on single gas atoms (7,8), on gas atom clusters (8) and on highly mobile and immobile non gaseous impurities (7) and to include the effects of mobile inert gas (8).

All these treatments have shortcomings which have been resolved by a unified treatment of the nucleation process (10), which proceeds atomistically from first principles to derive equations for terminal void number densities under a variety of conditions. This paper presents a nunierical evaluation of this theory for materials with the physical parameters of

type J16 stainless steel and the Nimonic alloy PE-16. Conditions are derived for spontaneous (no activation barrier) void formation, and terminal void number densities are calculated and compared with experimental results on each material,

2. Theory: Nodal Line Formalism

The theory considers the motion of a void in a phase space of n (number and vacancies) and x (number of helium atoms). Equations are written for void movement in (n,x) space. Such first-order differential equations in which time does not appear explicitly (termed Autonomous) and which may be linearized in the region of interest lend themselves to analysis through a rather well-developed branch of mathematics associated with the name of Poincaré (13-15). This analysis emphasizes the loci of points wnere n or x are zero (nodal lines) and points of intersection, where n = x = 0 (critical points). The application of this formalism to radiation effects problems is described in detail elsewhere (16).

Simultaneous solution of x = n = 0 shows intersections of the nodal lines (critical points) to occur at n values given by:

$$n^{1/3} = \frac{A}{3\ln S_e} \pm \frac{A}{3\ln S_e}(1-\psi)^{1/2}$$

where

$$\psi = \frac{9\beta_x^{\circ}\ln S_e}{A\,K_x^{c}}$$

$$A = (36\pi\Omega^2)^{1/3}\gamma/kT$$

$$\ln S_e = \ln[S_v(1-\beta_i^{\circ}/\beta_v^{\circ})]$$

When $\psi > 1$ no activation barrier to nucleation exists and any (n,x)-mer is free to grow spontaneously and rapidly upon reaching a critical gas content (x*).

3. Terminal Void Number Density

One important and experimentally measurable quantity in void swelling is the number density of voids, i.e. voids per unit volume (ρ_c). However, ρ_c may generally not be obtained simply by multiplying the nucleation rate by the irradiation time as nucleation is often preceded by an incubation time and often terminates early in the irradiation.

Once begun, nucleation is assumed to proceed until it is terminated by the growing voids, which through trapping of vacancies or gas atoms or by decreasing the biasing or by a combination of these factors to render $\psi < 1$. In that all three of these quantities are related to the sink strength it follows that a certain critical void sink strength, k_c^2, will be required to terminate the nucleation process.

4. Results and Discussion

The void nucleation parameter, ψ, was evaluated for each of the materials as a function of the homologous temperature (T/T_m). This allowed the regime over which void nucleation is spontaneous to be determined for a given pre-injection concentration of helium. In the case of 316 SS under a fast neutron flux, the analysis was applied with helium concentrations appropriate to one year of exposure in fission (C_x^o = 20 appm*) and fusion (C_x^o = 300 appm) environments).

In the case of PE-16 with C_x^o = 1 appm, $\psi > 1$ in the interval $0.32 < T/T_m < 0.59$. For 316 SS under neutron irradiation $\psi > 1$ over a substantial temperature range even at C_x^o = 1 appm.

The interval for which $\psi > 1$ appears to agree with the temperature interval over which voids have been observed (26). These

*appm = atomic parts per million

results also reproduce the relative susceptabilities of 316 SS and PE-16 to swelling reported by Johnston et al. (27). The fact that PE-16 does swell with C_x° = 1 appm is explainable in the context of the theory. When bohh nodal line intersections occur at sufficiently small values of (n,x), the situation is essentially that a small, easily produced vacancy : gas aggregate is stable, or small fluctuation may result in observable void nucleation.

A crucial test of a theory of void nucleation is its ability to predict the void number densities (voids/cm^3) observed in irradiated materials. If agglomeration of voids during growth is ignored and the nucleation rate is considered not to be a function of time, the final void number density is obtained in terms of an equation which involves no adjustable parameters, and although there is uncertainty in some of the physical parameters (in particular ρ_d, K_x^c and K*), this is not enough to greatly affect the results of the calculation. In the case of stainless steel, the calculations were performed before the experimental results were obtained for comparison, so the calculations are in no sense curve fitting.

The calculated void densities for the case of spontaneous nucleation are depicted in Figs. 1,2 for 316 SS and PE-Ib in relation to measured values. In the case of PE-16, the theory predicts void number densities somewhat higher than are actually observed. However, this calculation did not consider the role of coherent γ' precipitates as point defect traps; this omission would give too high calculated number densities. In the case of type 316 stainless steel, the extremely good agreement is partly fortuitous, as theory and experiment refer to two different damage rates. The agreement should, however, still be reasonably good for data taken under the displacement conditions assumed in the calculations.

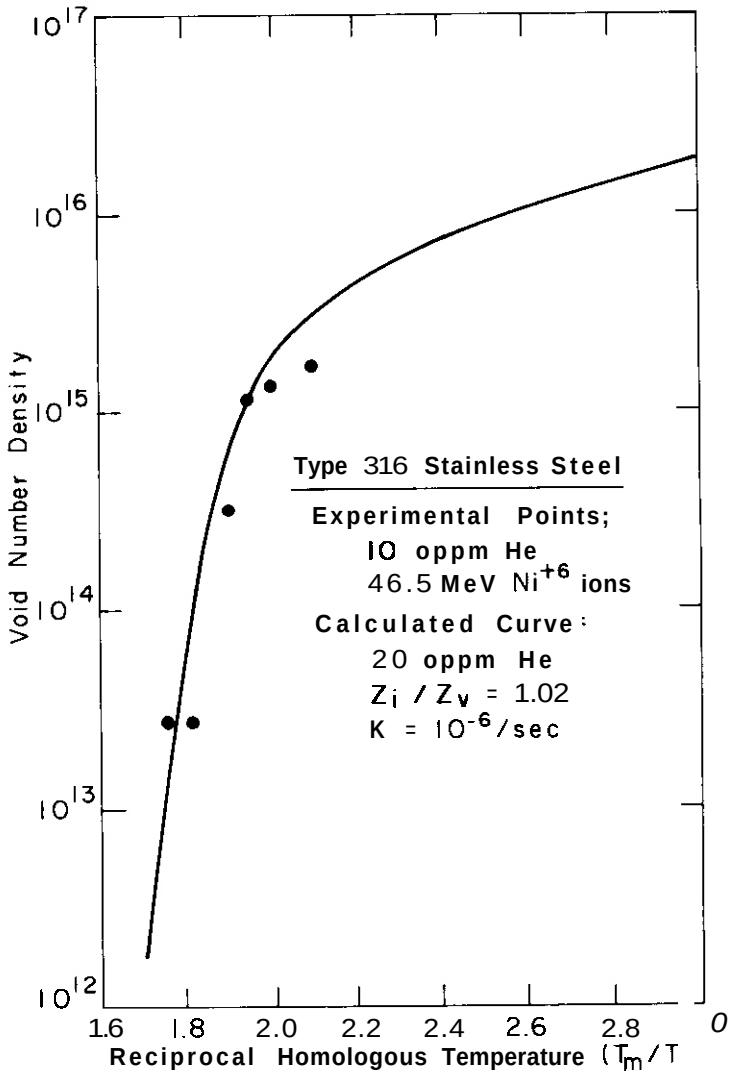

FIGURE 1. Comparison of Measured and Calculated Void Number Densities in Type 316 SS.

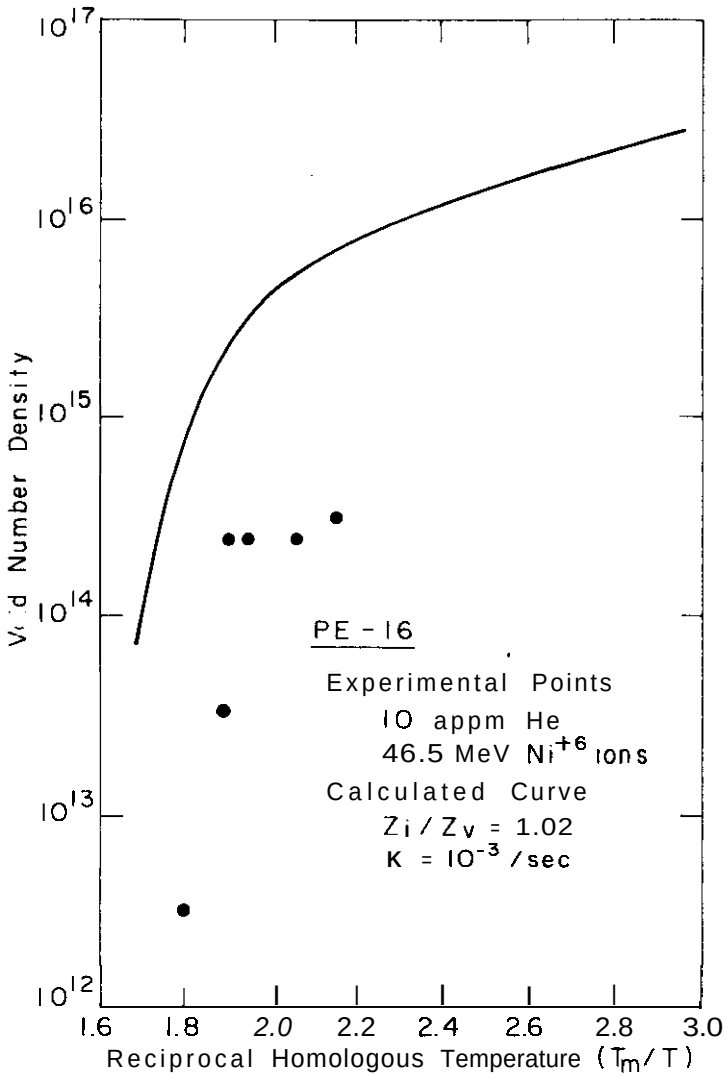

FIGURE 2. Comparison of Measured and Calculated Void Number Densities in PE-16.

VI. REFERENCES

1. C. Cawthorne and E. J. Fulton, Nature 216, 575 (1967).

2. "Voids Formed by Irradiaton of Reactor Materials," ed. S. F. Pugh, M. H. Loretto, and D. I. R. Norris, Brit. Nucl. En. Soc. (1971).

3. Radiation- Induced Voids in Metals," AEC Symposium Series CONF_ 710601, Albany, N.Y. (June, 1971).

4. "The Physics of Irradiation Produced Voids," ed. R. S. Nelson, HMSO, London (1975).

5. K.C. Russell, Acta Met. 19, 753 (1971).

b. J. L. Katz and H. Weidersich, J. Chem. Phys. 55, 1414 (1971).

7. K. C. Russell, Scripta Met. 7, 755 (1973).

8. H. Weidersich, J. J. Burton and J. L. Katz, J. Nucl. Mat. 51, 287 (1974).

9. K. C. Russell and D. H. Hall in Defects and Defect Clusters in bcc Metals and Their Alloys, ed. R. J. Arsenault, p. 545, National Bureau of Standards, Washington, D.C. (1973).

10. "The Theory of Void Nucleation in Metals," K. C. Russell, Acta Met. (In Press).

11. K. C. Russell, J. Nucl. Mat. 61, 330 (1976).

12. K. C. Russell, Acta Met. 20, 899 (1972).

13. H. Poincaré. Le Methods Nouvelles de la Mecanique Celeste, Vols. I-III, Sauthiers-Villars, Paris (1892-1899).

14. L. E. El'Sgol'ts, Transl. Math. Monographs, V. 12 Amer. Math. Soc., Providence, R.I. (1964).

15. R. J. Somorjai in Physical Chemistry, V. XI-B, eds. H. Eyring, D. Henderson and W. Jost, Academic Press, New York (1975).

16. S. I. Maydet and K. C. Russell, J. Nucl. Mat. 64, 101 (1977).

17. S. I. Maydet, "Numerical Analysis of a Theory of Void Nucleation in Metals Under Irradiation," SM Thesis, M.I.T. (June, 1977).

18. Handbook of Chemistry and Physics, 52 edition, ed. R. C. Weast, Chenical Rubber Company, Cleveland, Ohio (1972).

19. Table of the Periodic Properties of Elements, Szrgent-Welch Scientific Company, Skokie, Illinois (1968).

20. H. Weidersich in Radiation Damage in Metals, ASM, Metals Park, Ohio (1977).

21. R. Bullough and R. C. Perrin in Radiation-Induced Voids in Metals, p. 778, AEC Symposium Series, CONF-701601, Albany, N.Y. (June, 1971).

22. H. R. Brager and J. L. Straalsund, Met. Trans. 2, 1893 (1971).

23. J. A. Sprague, J. E. Westmoreland, F. A. Smidt, Jr. and P.R. Malmberg, J. Nucl. Mat. 54, 286 (1974).

24. E. E. Bloom and J. O. Steigler in Effects of Radiation on Substructure and Mechanical Properties of Metals and Alloys, p. 360, ASTM STP 529, Philadelphia, PA (1973).

25. A. D. Brailsford and R. Bullough, J. Nucl. Mat. 44, 121 (1972).

26. A. J. Bement, Jr., "Void Formation in Irradiated Austenitic Stainless Steels," in Advances in Nuclear Science and Technology, V. 7, p. 1 (1973).

27. W. G. Johnston, T. Lauritzen, J. H. Rosolowski and A. M. Turkalo, "The Effect of Metallurgical Variables on Void Swelling," in Radiation Damage in Metals, ASM, Metals Park, Ohio (1977).

VII. FUTURE WORK

The next step is to model void nucleation on dislocations and precipitates.

VIII. PUBLICATIONS

A paper entitled "Numerical Simulation of Void Nucleation in Irradiated Metals" will shortly be submitted to Journal of Nuclear Materials.

I. PROGRAM

Title: Mechanical Properties
Principal Investigator: R. H. Jones
Affiliation: Battelle - Pacific Northwest Laboratory

II. OBJECTIVE

The displacement damage produced in Materials Research Corporation Marz grade nickel and niobium and reactor grade 316 SS by 16 MeV protons and (D,T) and (D, Be) neutrons is being correlated on the basis of cluster size and density and yield strength. The effects of both steady state and cyclic flux, temperature and stress on the microstructure and flow stress is being studied. The relationship between the radiation induced microstructure and flow properties is also being studied. Irradiation damage studies of path B and C alloys are planned.

III. RELEVANT DAFS PROGRAM PLAN TASK/SUBTASK

SUBTASK II.C.5	Effects of Cycling on Microstructure
SUBTASK II.C.11	Effects of Cascades and Flux on Flow
SUBTASK II.C.12	Effects of Cycling on Flow and Fracture

IV. SUMMARY

The damage produced in nickel and niobium by 16 MeV protons and T(d,n) neutrons has been correlated as a function of particle fluence on the basis of microstructure and flow stress. Proton and neutron irradiations were performed on material taken from the same source; with the same geometry, given identical heat treatments, prepared and evaluated by the same techniques, and irradiated at 20-30°C at a flux 10^{12} particles/cm^2-s.

16 MeV protons produced an equivalent amount of hardening per particle in the nickel as the T(d,n) neutrons and about 20% more hardening per particle in the niobium at 10^{17} particles/cm^2. The fluence dependence of the yield strength increase of 16 MeV proton and T(d,n) neutron irradiated nickel and niobium were equal, within the experimental error.

Preliminary cluster size and density results for proton and neutron irradiated nickel indicate a similarity in size but a higher density for the proton irradiated material. The average cluster diameters were 25A° and 35A° for the proton and neutron irradiated nickel, respectively, while the cluster densities were 2.5×10^{16} cm^{-3} and 1x1016 cm^{-3}, respectively.

V. ACCOMPLISHMENTS AND STATUS

A. Light Ion and Fusion Neutron Damage Studies -- R. H. Jones, D. L. Styris and E. R. Bradley (PNL)

1. Introduction

The use of energetic light ions for simulating the radiation damage effects of 14 MeV neutrons on microstructure and mechanical properties looks attractive because of their penetrating power, high available fluxes ($>10^{14}$ p+/cm^2-s) and primary knock on spectra which closely simulates that produced by 14 MeV neutrons in some materials. Calculations by Logan et.al. (1) indicated the recoil energy spectra of 16 MeV protons closely simulate that of 14 MeV neutrons in niobium while damage energies and displacement cross-section reported by Omar et. al, (2) indicate that the high energy recoil damage produced by 16 MeV protons and 14 MeV neutrons should be very similar while the low energy (> 1 keV) recoil damage will differ. Transmission electron microscopy observations by Mitchell et.al. (3) showed a similarity between the size and density of defect clusters in copper irradiated with 16 MeV protons and 14.8 MeV neutrons. Experiments have been undertaken to evaluate and compare the

effects of damage produced by energetic light ions and fusion energy neutrons on the microstructure and flow stress of nickel, niobium and 316SS.

2. 16 MeV Proton Irradiations

An apparatus for monitoring and controlling the irradiation environment of materials during bombardment with energetic light ions (<28 MeV pf, d+, α^{++}) has been assembled and located at the Nuclear Physics Laboratory of the University of Washington. The ion beam from the University of Washington Tandem Van de Graaff is continously monitored by a profile monitor, quadrant collimators, three chromel-alumel thermocouples in the same plane as the specimens and a vacuum faraday cup. The specimens, collimator and beam scanner are, 2, 5 and 25 cm in front of the faraday cup, respectively. Particle fluence is determined from the integrated faraday cup current and a 0.04mm thick vanadium dosimeter positioned directly in front of the specimens. The ^{51}V (p,n) ^{51}Cr reaction cross-section is taken to be 325 mb cross-section for 16 MeV protons[4,5] The vacuum faraday cup is isolated from the irradiation chamber by a thin Havar window and maintained at a pressure of $5x10^{-7}$ torr by a 2 ℓ/s ion pump. The integrated cup current and the vanadium dosimeter agree within 10%.

Specimen cooling is accomplished with either a static or flowing helium atmosphere. The helium flow is maintained with a stainless steel diaphram pump, purified with a liquid nitrogen cryopump and monitored with a quadrapole mass analyzer and oxygen analyzer. The system is initially vacuum processed at 200°C to a pressure of 10^{-9} torr, and back filled with high purity helium boiled from a liquid helium dewar. The affectiveness of the flowing helium gas for cooling the wire specimens was recently demonstrated by a 3 $\mu a/cm^2$ ($2x10^{13}$ p+/cm^2-s) beam of 16 MeV protons where the specimen temperature was 300°C in static helium and 30°C in flowing helium.

The yield strength change of irradiated nickel and niobium is shown in Figures 1 and 2 as a function of particle fluence. Preparation and testing techniques for the 0.25mm diameter wires and comparison of the unirradiated flow properties with bulk specimens have been reported previously.(6,7)

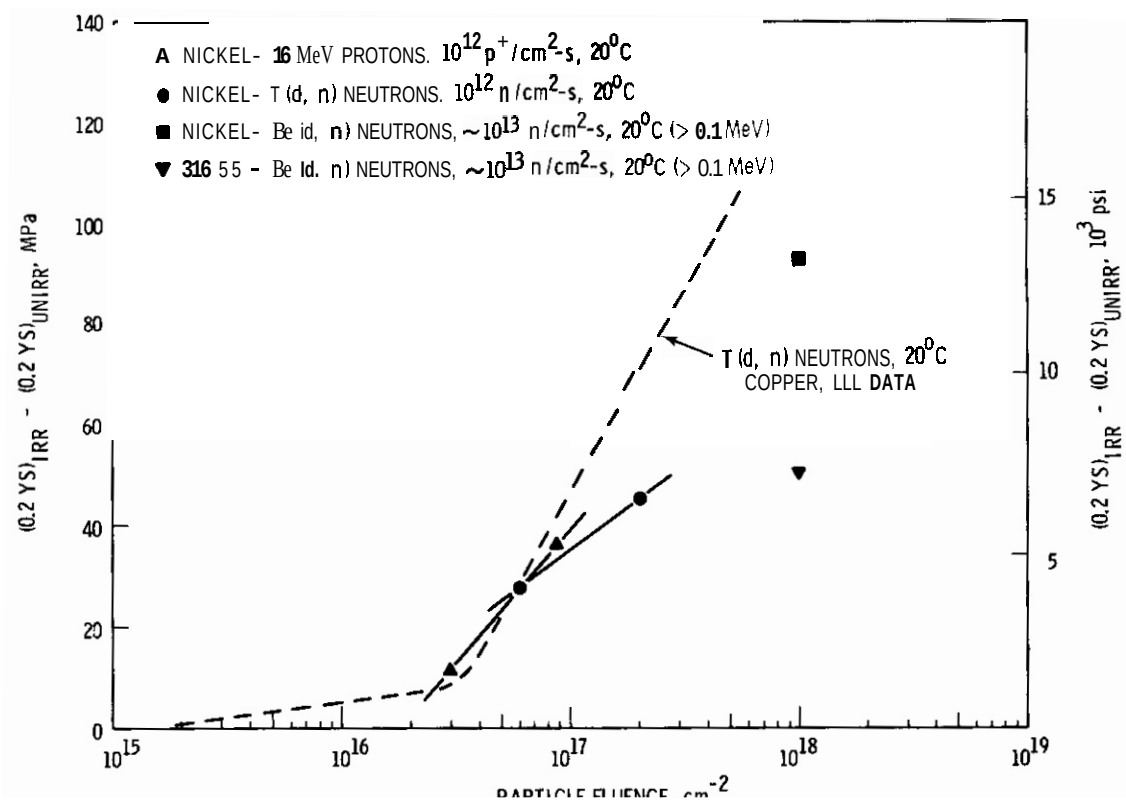

FIGURE 1. Yield strength increase versus particle fluence for 16 MeV proton and 14 MeV neutron irradiated nickel.

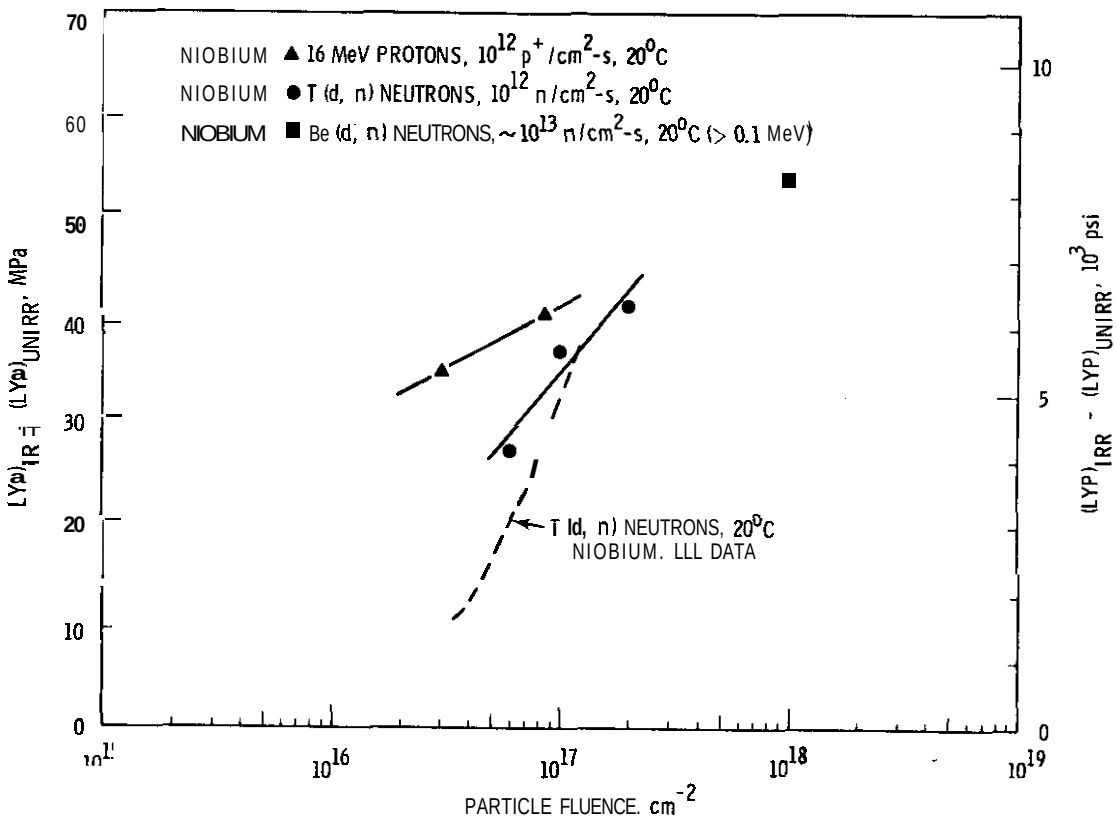

FIGURE 2. Yield strength increase versus particle fluence for 16 MeV proton and 14 MeV neutron irradiated niobium.

16 MeV protons produced an equal amount of hardening in nickel and 20% more hardening in niobium than T(d,n) neutrons at equal particle fluences. However, at equal damage energies the 16 MeV protons produced about 20% less hardening at 5×10^{-2} eV in nickel and equal hardening in niobium, as shown in Fig. 3. The damage energy cross sections given by Omar et al.[2] were used for these calculations. Within the experimental scatter of ± 10%, the hardening dependence on 16 MeV proton and T(d,n) neutron

fluence are equal in both nickel and niobium. Certainly more data is needed to confirm this conclusion.

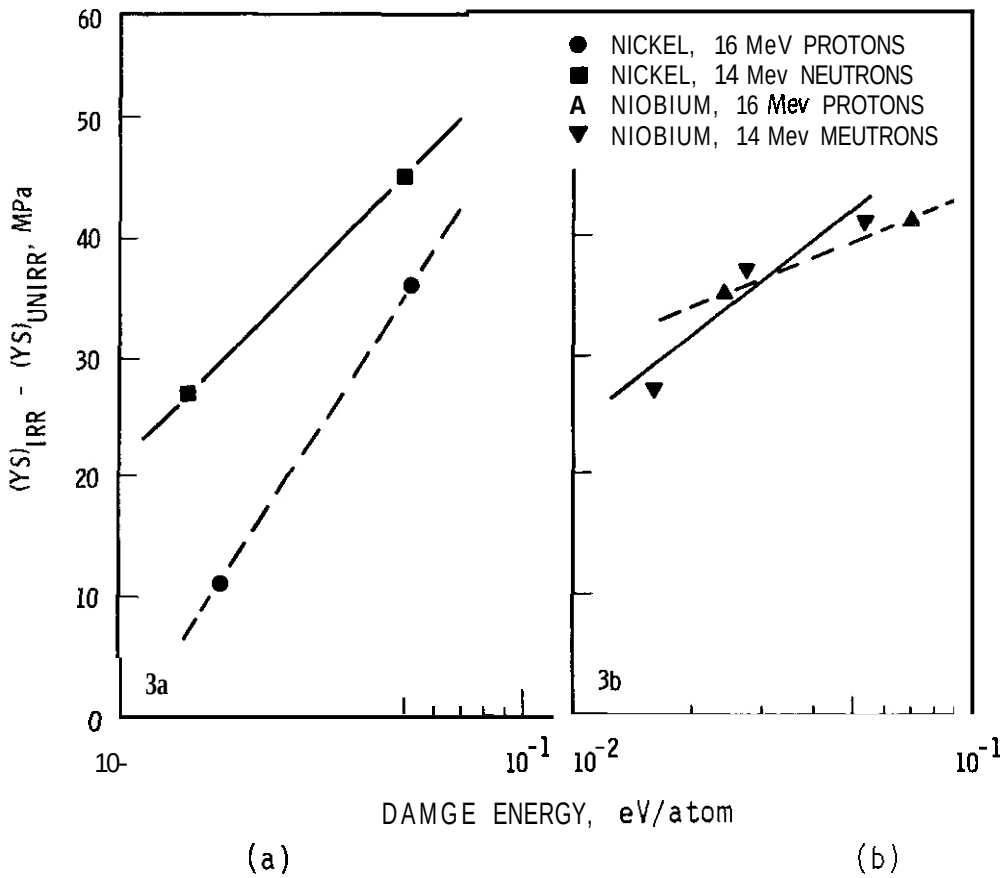

FIGURE 3. Yield strength increase versus damage energy for 16 MeV proton and 14 MeV neutron irradiated a) nickel, b) niobium.

Preliminary cluster size versus density results for 16 MeV proton and 14 MeV neutron irradiated nickel are shown in Figure 4. The microscopy results are too preliminary to allow quantitative comparisons; however, they do indicate that 16 MeV protons produce a larger defect cluster density than T(d,n) neutrons in nickel. These results are not in

agreement with the calculated recoil spectra[1,2] and microstructural results in copper[3] for 16 MeV proton and 14 MeV neutron irradiated material. Further microstructural studies are underway to help clarify these differences.

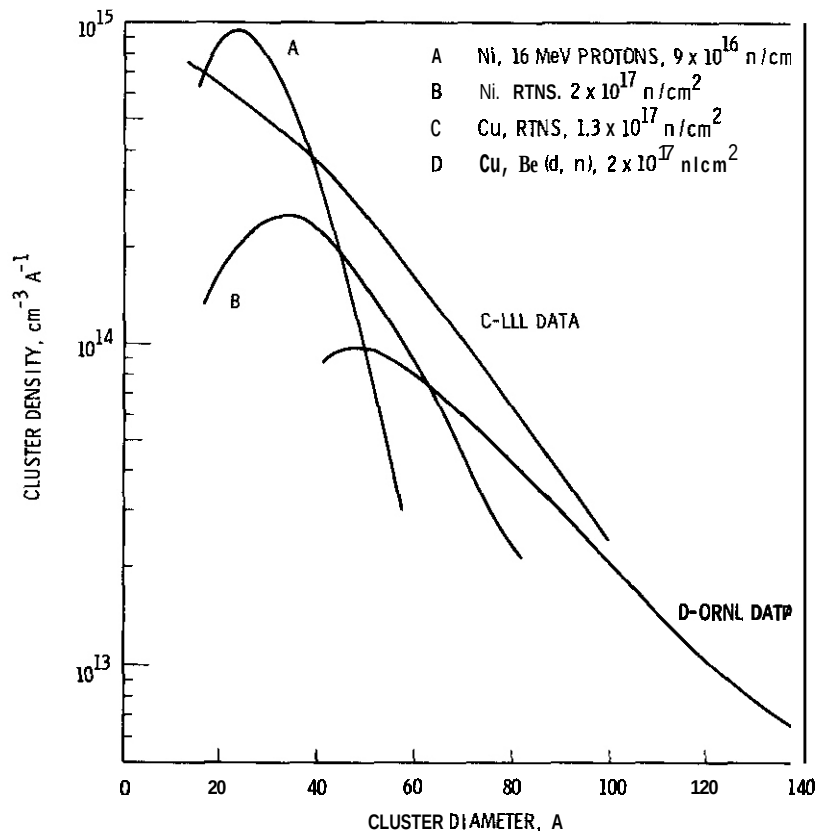

FIGURE 4. Preliminary results showing point defect cluster density versus size for 16 MeV proton and 14 MeV neutron irradiated nickel. Curve C is LLL data and D is ORNL data.

3. Be (d,n) Neutron Irradiations

.-,n) neutron irradiations of nickel, niobium and 316 SS wires and foils have been completed over a fluence range of $1x10^{17}$ n/cm^2 to $1x10^{18}$ n/cm^2 at 20°C using the cyclotron at the University of California at Davis. A neutron flux of $6x10^{12}$ cm^{-2} s^{-1} (>0.1 MeV) was obtained by placing the 1.5 mm thick wire-foil packet against a beryllium target on which a 22ma beam of 40 MeV deuterons was directed. The target was built by Lawrence Livermore Laboratory and the multi-foil dosimetry is being done by Argonne National Laboratory and LLL. The 7x50 mm dosimeter foils were sliced into 2mm wide strips perpendicular to the longitudinal specimen axis to give some spatial information about neutron energy and flux. The yield strength results for the Be (d,n) neutron irradiation to 10^{18} n/cm^2 are shown in Figures 1 and 2. The hardening response of the nickel is greater than a straight line extrapolation of the T(d,n) nickel data while the niobium results are slightly less. The 316SS had a hardening response of approximately 1/2 that of the nickel. Quantitative comparison between the Be (d,n) and T (d,n) results should be possible with the evaluation of the specimens irradiated to $1x10^{17}$ and $5x10^{17}$ n/cm^2.

B. Effect of Energetic Particles on the Tensile Properties of Nickel and Niobium

The proton and neutron irradiated wire specimens have been strained to failure to evaluate the effects of energetic particle damage on the ultimate tensile strength and strain to failure. While this data is not of the same quality as the flow stress data because of the greater degree of scatter in the data and larger divergence of the wire properties from bulk properties, some interesting trends are observed. The results for 16 MeV proton and T(d,n) and Be (d,n) neutron irradiated nickel and niobium are shown in Figures 5 and 6.

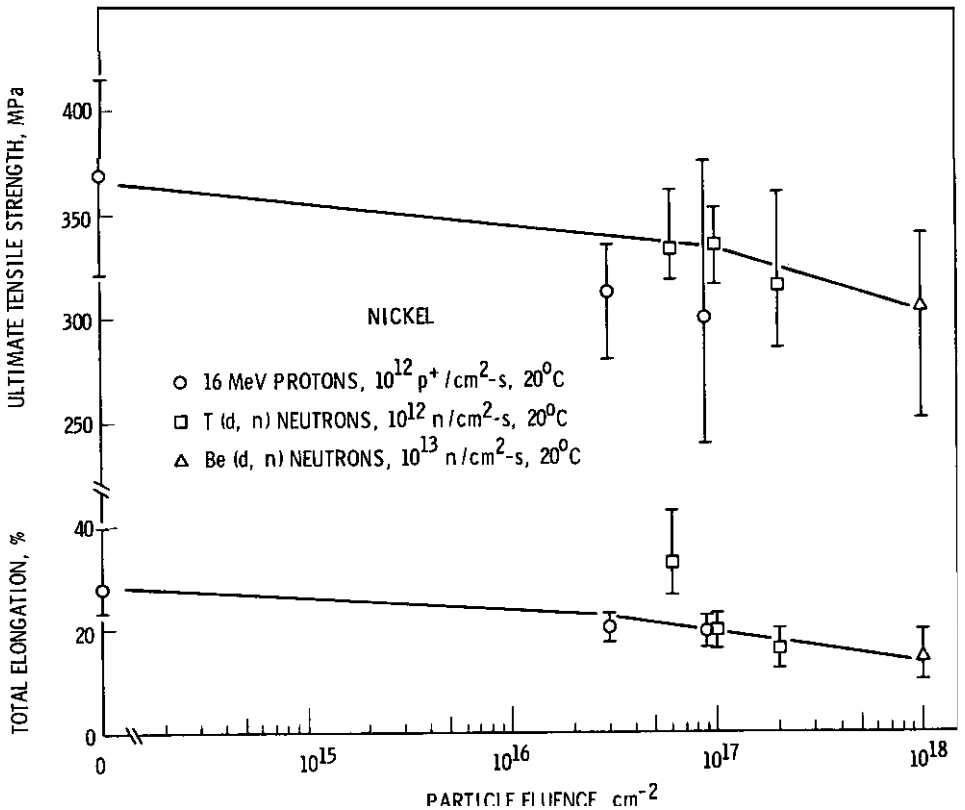

FIGURE 5. Ultimate tensile strength and total elongation versus particle fluence for 16 MeV proton and 14 MeV neutron irradiated nickel.

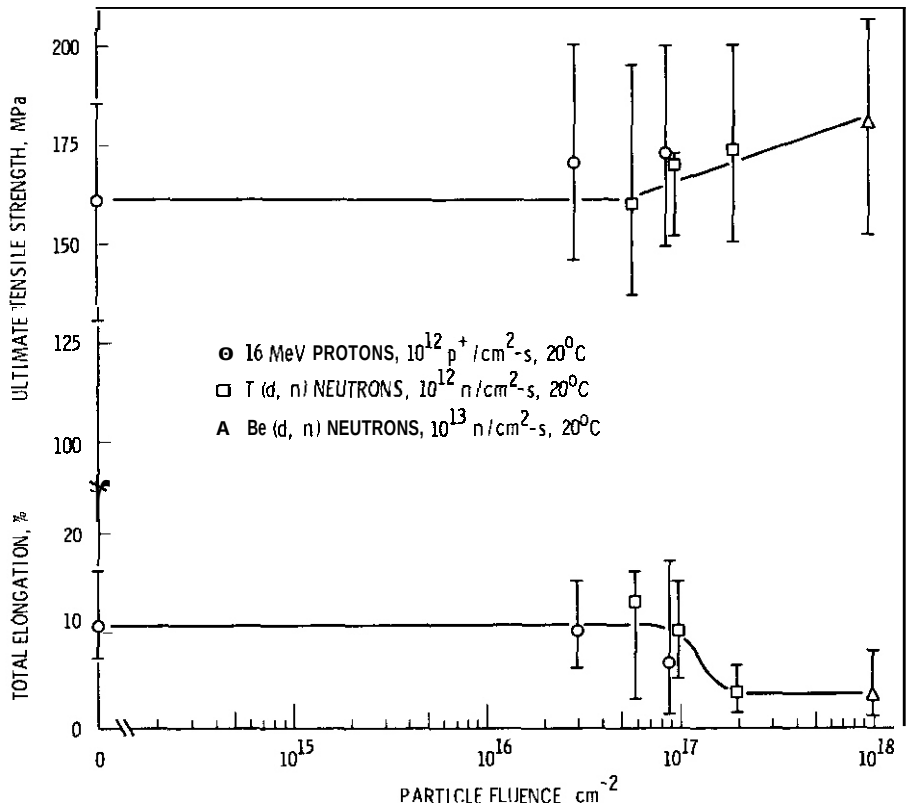

FIGURE 6. Ultimate tensile strength and total elongation versus particle fluence for 16 MeV proton and 14 MeV neutron irradiated niobium.

The ultimate tensile strength and total elongation of nickel decreased with increasing particle fluence while the ultimate tensile strength of niobium increased with fluence and the total elongation decreased. The present data is insufficient to allow comparisons between the various particles; however, the tensile property changes coincide with the onset of defect agglomeration into clusters. In niobium, the work hardening rate is apparently reduced by the presence of the defect

clusters such that only inhomogeneous strain (luders band type deformation) occurs. This inhomogeneous strain is probably associated with dislocation channeling as observed in fission neutron irradiated niobium by Wechsler et. al.[8]

VI. REFERENCES

1. C. M. Logan, J. D. Anderson and A. K. Mukherjee, "Proton Simulation of Displacement Effects Induced in Metals by 14 MeV Neutrons, J. Nucl. Mater. 48, (1973), 223.

2. A. M. Omar, J. E. Robinson and D. A. Thompson, "Calculations of Scattering and Radiation Damage Parameters for 14 MeV Neutrons and 10 *to* 20 MeV Protons on Fe, Ni, Cu, Zr, Nb and Au," J. Nucl. Mater., 64, (1977), 121.

3. J. B. Mitchell, C. M. Logan and C. J. Echer, "Comparison of 16 MeV Proton, 14 MeV Neutron and Fission Neutron Damage in Copper," J. Nucl. Mater., 48, (1973), 139.

4. Wing, Huizenga, Phy. Rev., 128, (1962), 280.

5. Chodil et. al., Nucl. Phy. A, 93, (1967), 648.

6. R. H. Jones and D. L. Styris, "Some Considerations of Temperature and Displacement Rate Gradients and Specimen Dimensions on Penetrating Ion Irradiation Experiments," The Proceedings of the 2nd Topical Meeting on The Technology of Controlled Nuclear Fusion, G. L. Kulcinski, ed., p. 247, Richland, WA 1976.

7. R. H. Jones and D. L. Styris, "16 MeV H^+ and (D,T) Neutron Hardening Correlation in Nickel and Niobium at 20°C," Trans. ANS 1977 Annual Meeting, vol. 26, p. 193, New York, 1977.

8. M. S. Wechsler, R. P. Tucker, and R. Bode, "Radiation Hardening in Single Crystal Niobium - The Temperature Dependence of Yielding," Acta Met. 17, (1969), 541.

VII. FUTURE WORK

The next immediate milestone is to complete 16 MeV proton irradiations at a flux of 10^{13} p^+/cm^2-s over a fluence range of 10^{17} to 10^{18} p^+/cm^2 at 20°C. The second 16 MeV proton irradiation milestone is to perform elevated temperature irradiations at fluxes of 10^{13} to $2x10^{14}$ p^+/cm^2-s.

The next fusion neutron milestone is to evaluate the specimens irradiated to $1x10^{17}$ n/cm^2 and $5x10^{17}$ n/cm^2 with Be(d,n) neutrons. The second fusion neutron irradiation milestone is ambient and elevated temperature irradiations at RTNS 11. Also, within the next 6 months, path B and C alloys for proton and neutron irradiation will be selected and procured.

VIII. PUBLICATIONS

1. D. L. Styris and R. H. Jones, "Experimental Studies Using Light Ions to Simulate Fusion Neutron Damage Effects on Mechanical Properties" 24th National Vacuum Symposium, Nov. 8-11, 1977, Boston, MA.

I. PROGRAM

Title: 14 MeV Neutron Irradiation Studies
Principal Investigator: Richard R. Vandervoort
Affiliation: Lawrence Livermore Laboratory

II OBJECTIVES

This project has the following principal objectives: 1) to characterize 14 MeV neutron damage; 2) to compare radiation damage from 14 MeV neutrons, Be(D,n) neutrons, and fission reactor neutrons; and 3) to evaluate the effect of helium on the mechanical properties of Nb and Nb-1%Zr.

III. RELEVANT OAFS PROGRAM PLAN TASK/SUBTASK

SUBTASK	II.C.6.3	Low Energy-High Energy Neutron Correlations
	II.C.7.1	Helium Injection Experiments
	II.C.11.4	High Energy Neutron Irradiations
	II.C.18	Relating Low and High Exposure Microstructures

IV. SUMMARY

A. 14 MeV Neutron Damage

Tensile specimens of copper, vanadium, and niobium were irradiated by high-energy neutrons from the Rotating Target Neutron Source (RTNS-I) and the Be(D,n) Source at the University of California at Davis and by lower-energy neutrons from the Livermore Pool-Type Reactor (LPTR). After being irradiated, the specimens were tensile tested, and the increases in their 0.2%-offset yield strengths were related to the neutron fluences. In these metals, about 20 times as great a fluence of neutrons (E > 0.5eV) from the LPTR was required to produce the same increase in yield strength as RTNS 14 MeV neutron fluences above 10^{17} n/cm^2; the corresponding ratio

for Be(D,n) neutrons to RTNS neutrons was about 1.3. In terms of yield-strength increase versus displacement damage energy (eV/atom), the results showed that the radiation strengthening in these metals was essentially identical for the RTNS and Be(D,n) sources, while it took about twice as much damage energy to produce the same strengthening with LPTR neutrons.

B. Effect of Helium on the Mechanical Properties of Nb and Nb-1%Zr

An optimized process has been developed for doping Nb and Nb-1Zr specimens with helium using the tritium decay method. This process is commonly called the "tritium trick". Tritium is dissolved in the metal at 400°C to give a resultant Nb to ^3H ratio of 20 and an equilibrium partial pressure of 1.33 Pa over the specimens. The tritium decays by the reaction $^3H \rightarrow {}^3He + \beta^-$ at a rate that produces about 7 atomic ppm helium per day in the host microstucture. Mechanical properties specimens can be successfully doped to 500 appm ^3He in less than 10 weeks using this technique.

Tensile tests were done on annealed specimens and specimens having several ^3He concentrations in both Nb and Nb-1Zr materials. Tests were conducted under high vacuum to temperatures as high as 800°C.

Helium generally caused an increase in strength and decrease in ductility in both materials over the range of test temperatures. While the loss in ductility was significant, it was not considered to be deleterious.

V. ACCOMPLISHMENTS AND STATUS

A. 14 MeV Neutron Damage -- J. B. Mitchell

1. Introduction

Fusion neutrons will create a larger number of atom displacements per primary collision than lower energy (1-2 MeV) fast fission

neutrons and internal helium generation from (n,α) reactions will be substantially greater for fusion neutrons than for fast fission neutrons. Thus, we expect that the deleterious effects of radiation damage that have been experienced in fission-reactor materials will be even more severe in fusion reactors.

Studies are in progress to determine the characteristics and effects of 14 MeV neutron damage and to compare the nature and magnitude of these effects with radiation damage from Be(D,n) neutrons and fission reactor neutrons.

2. Specimens and Experimental Procedure

Small tensile specimens of copper, niobium, and vanadium were machined from 0.5 mm thick (0.020 in.) sheet stock. Overall specimen length was 28.6 mm. The gage section was 6.35 mm long and 1.57 mm wide. A chemical analysis of the copper is shown in Table I, and the interstitial impurities in the niobium and vanadium are shown in Table II.

Table I Chemical Analysis of Impurity Elements in Cominco Copper

Element	Concentration (appm)
Fe	400
Si	150
Mg	10
Ag	2
Ca	2
co	< 10
Ni	< 3
Al	< 3
Be	< 1

Table II Chemical Analysis of Interstitial Impurities in Niobium and Vanadium

Element	Concentration (appm)		
	LLL Niobium	MRC[a] Niobium	MRC[a] Vanadium
C	15	15	210
O	208	40	110
N	70	5	60

[a]Materials Research Corp.

The niobium and vanadium specimens were annealed for 1 hour at 1200 and 1000°C, respectively, in 0.13 μPa ($\sim 10^{-9}$ torr) vacuum. The copper specimens were annealed for 1 hour at 600°C in 1.3 mPa (10^{-5} torr) vacuum. These times and temperatures were selected to obtain grain sizes that would give at least ten grains over the 0.5 mm specimen thickness to insure reproducible polycrystalline tensile behavior.

Specimens were irradiated at the Rotating Target Neutron Source (RTNS-I), at the Be(D,n) source at the University of California at Davis, and at the Livermore Pool Type Reactor (LPTR). After irradiation, the specimens were tested in an Instron testing machine at about 26°C and a crosshead rate of 0.05 mm/min (0.002 in./min). The 0.2% offset yield stress was determined using the Instron crosshead motion as the sample extension.

3. Results and Discussion

The increase in 0.2%-offset yield stress versus neutron fluence for tensile specimens of Cu, Nb, and V are shown in Figs. 1, 2, and 3, respectively. It is apparent from these plots that the high-energy neutrons from the RTNS and Be(D,n) sources are considerably more effective than the lower-energy neutrons from the LPTR in strengthening all of the metals.

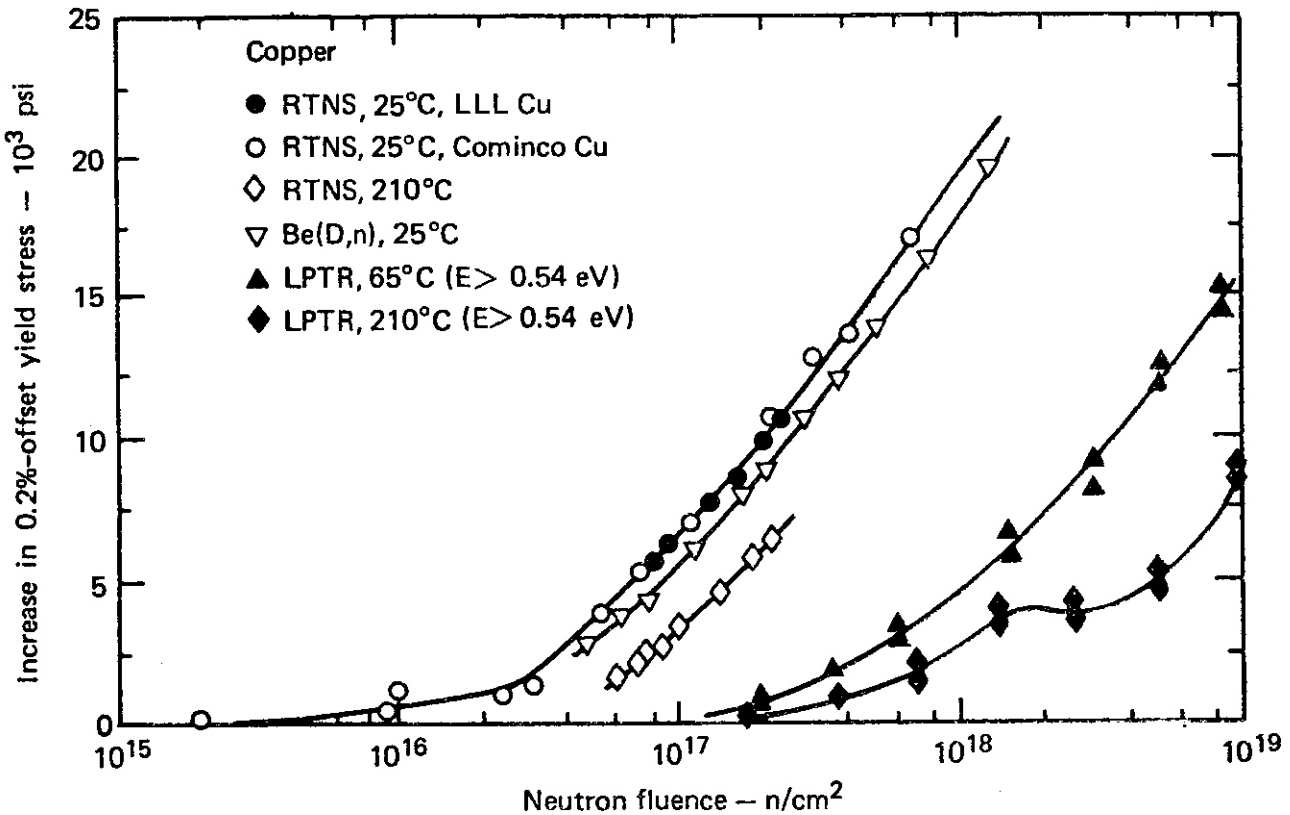

Figure 1. Increase in 0.2%-offset yield stress vs neutron fluence for RTNS, Be(D,n), and LPTR irradiations of copper.

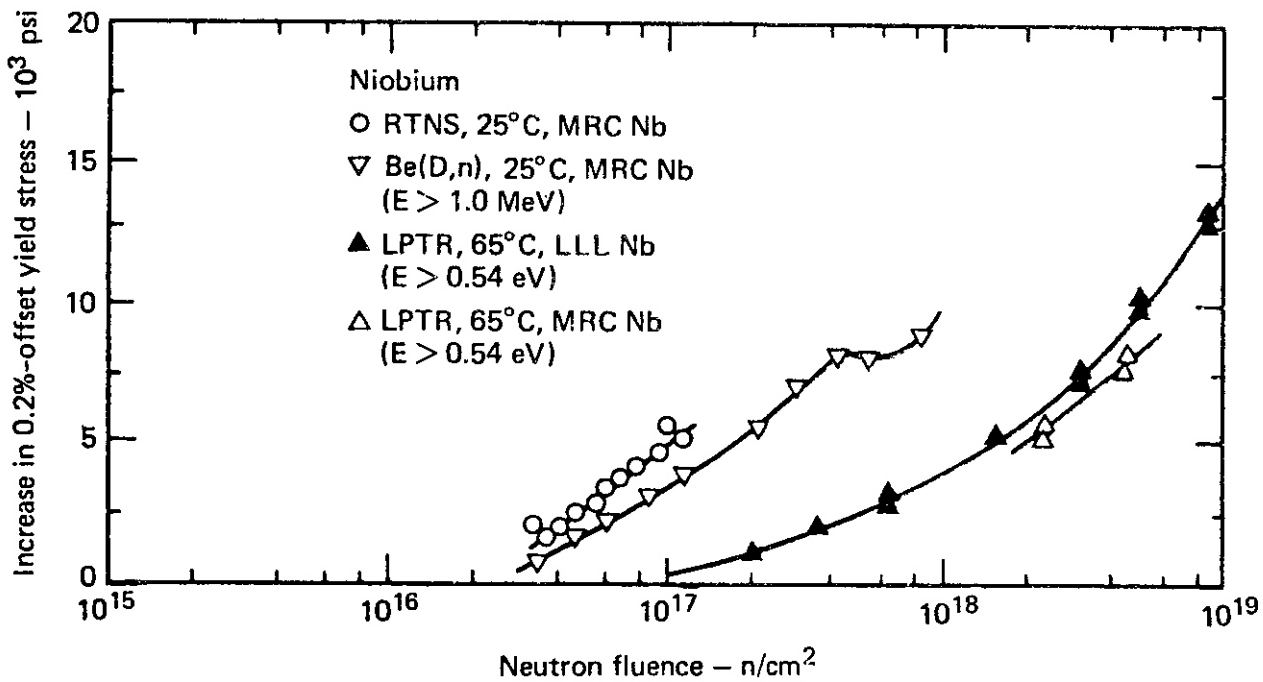

Figure 2 Increase in 0.2%-offset yield stress vs neutron fluence for RTNS, Be(D,n), and LPTR irradiations of niobium.

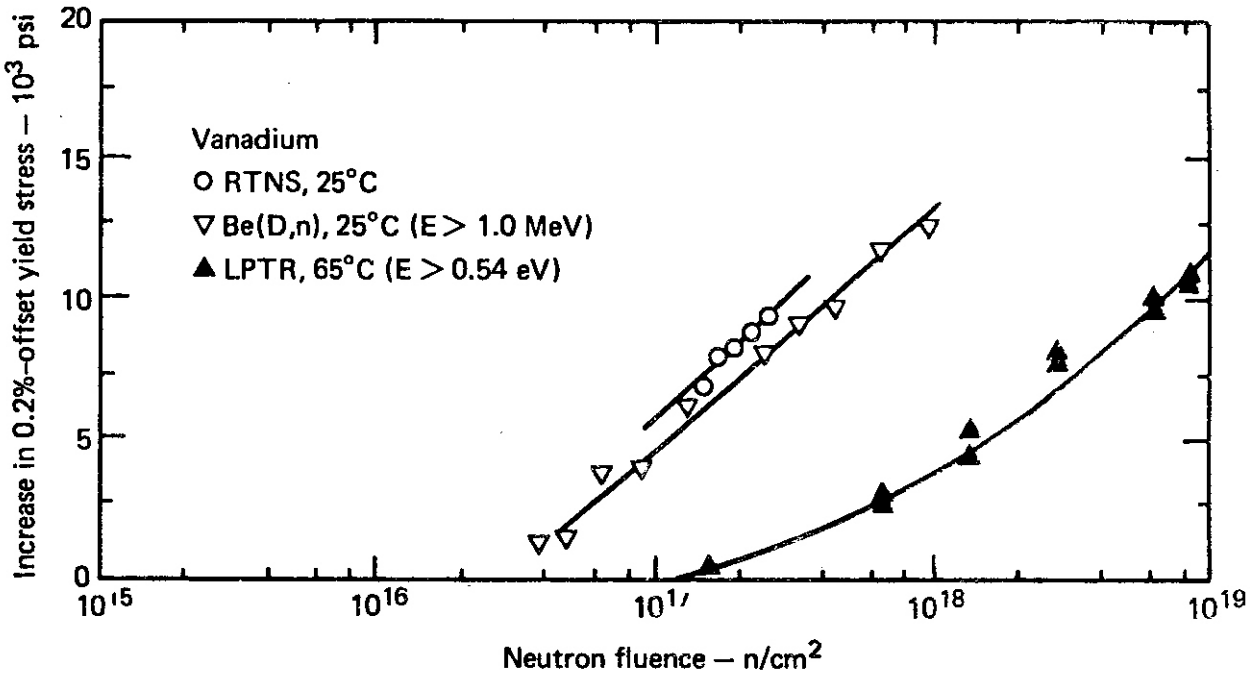

Figure 3. Increase in 0.2%-offset yield stress vs neutron fluence for RTNS, Be(D,n), and LPTR irradiations of vanadium.

If we compare the 25°C RTNS and 65°C LPTR data for the Cu, Nb, and V, we find that about 20 times as great a fluence of neutrons (E > 0.5 eV) from the LPTR is required to produce the same increase in yield strength as 14 MeV neutron fluences above about 10^{17} n/cm^2. (If the LPTR neutron fluence is experessed in terms of E > 0.1 MeV, this ratio reduces to about 10.)

Comparison of the 25°C RTNS and Be(D,n) data gives a ratio of Be(D,n) neutrons (E > 1.0 MeV) to RTNS neutrons of about 1.3 for the same strengthening.

LPTR irradiation produced greater strengthening in LLL Nb than in Materials Research Corp. (MRC) Nb. The only apparent difference between the two materials is the higher interstitial impurity content in the LLL Nb (see Table II). It has previously been shown that interstitial impurities can significantly increase the radiation strengthening of Nb irradiated with fission-reactor neutrons.(1)

The ambient-temperature results for Cu and Nb are plotted in Figs. 4 and 5 as yield-strength increase versus displacement damage energy. These plots normalize the results with respect to the differences in neutron energies from the three sources.

Figures 4 and 5 show that the ambient-temperature radiation strengthening produced in Cu and Nb by RTNS and Be(D,n) irradiations are essentially identical on the basis of damage energy, whereas it takes about twice as much damage energy to produce the same strengthening with LPTR neutrons. The same effect would be observed in V.

These differences in radiation strengthening produced for the same amount of displacement damage energy result from differences in the resultant structural damage. Transmission electron-microscopy observations reveal that the damage structures produced by the RTNS, Be(D,n), and LPTR irradiation consist of the same kind of primary defects, i.e., vacancy

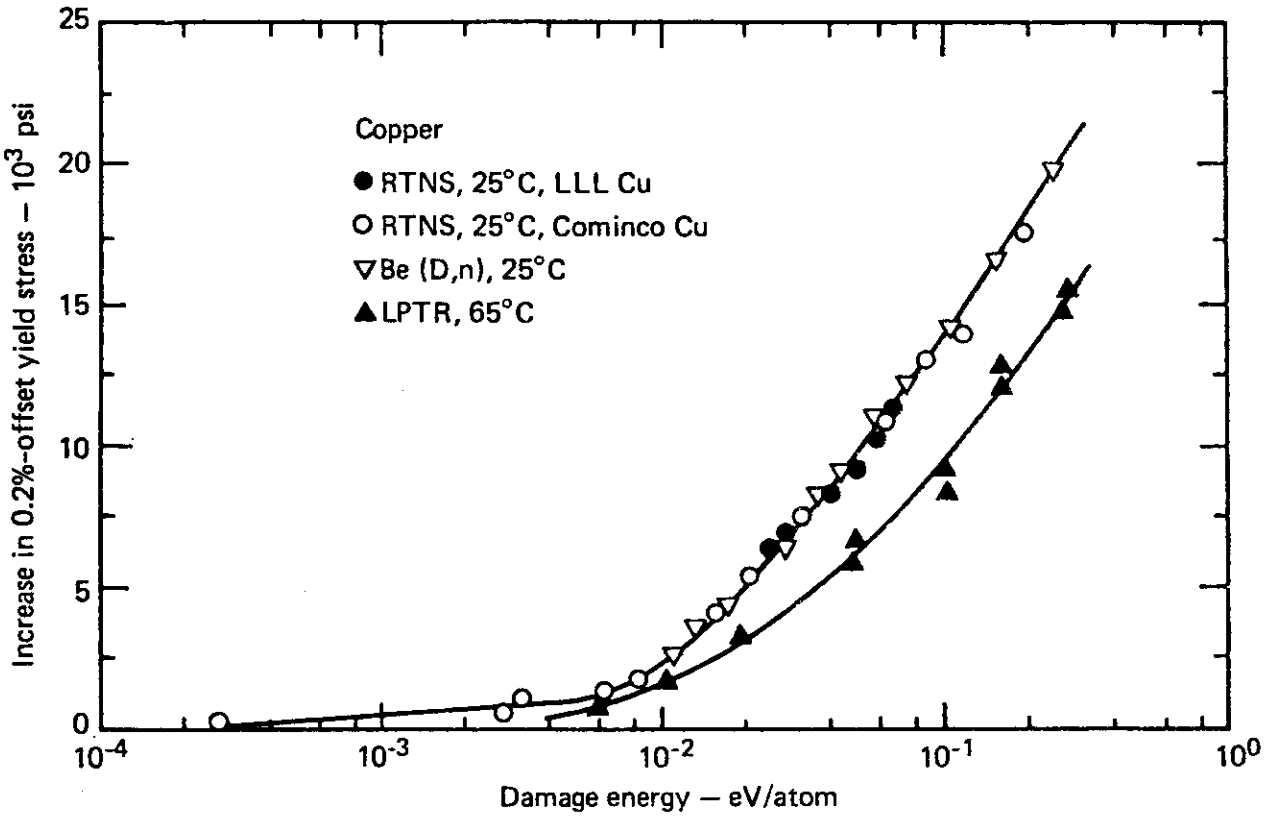

Figure 4. Increase in 0.2%-offset yield stress vs damage energy for neutron-irradiated copper.

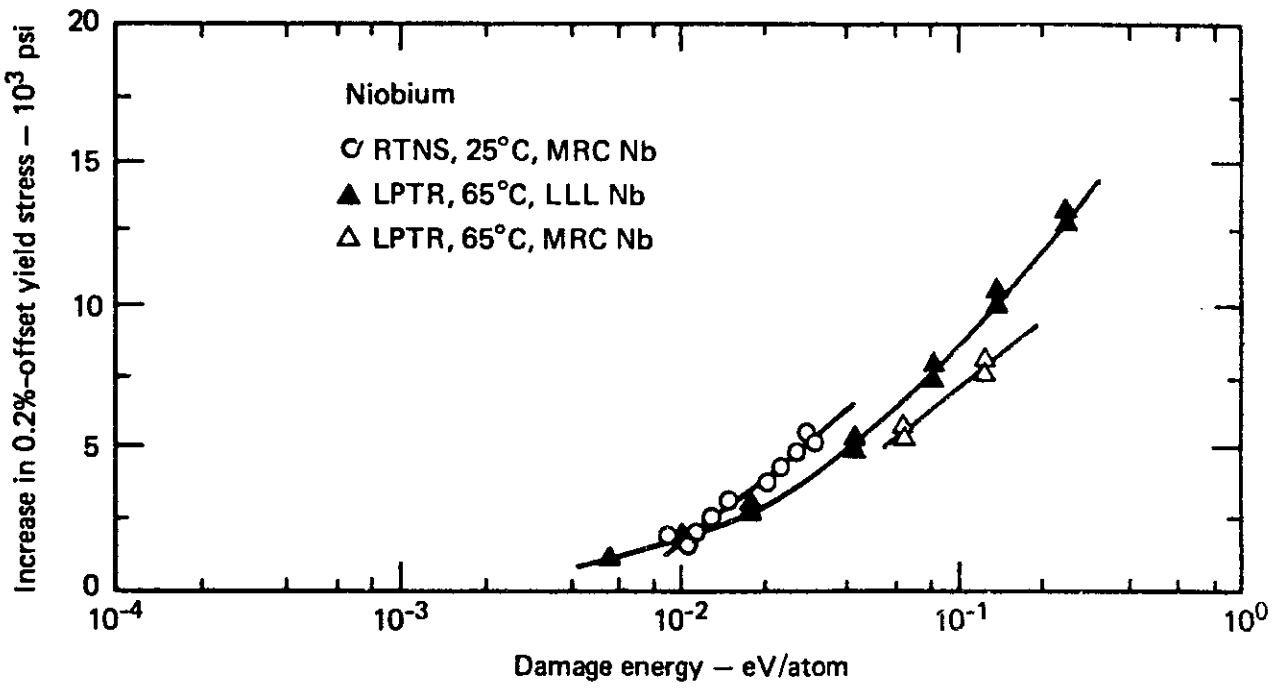

Figure 5. Increase in 0.2%-offset yield stress vs damage energy for neutron-irradiated niobium.

and interstitial clusters and small Frank and prismatic dislocation loops. In the pure metals irradiated to a given damage energy level, the damage structures produced with high-energy RTNS and Be(D,n) neutrons appear to differ from those produced with lower-energy LPTR neutrons in the number density and size distribution of the defects. Thus, it can be concluded that the fraction of radiation-produced displacment damage retained in the form of point-defect clusters is greater for high-energy neutrons than for fission-reactor neutrons.

B. Effect of Helium on the Mechanical Properties of Nb and Nb-1%Zr -- W. L. Barmore and R. R. Vandervoort

1. Introduction

High energy (E $\sim$ 14 MeV) neutron radiation from fusion reactors will cause enhanced damage to the microstructures of component materials. The displacement damage per incident 14 MeV neutron is greater, and cross sections for (n,α) reactions also are higher for fusion neutron irradiation than for fission neutron irradiation.

Mechanical properties of component materials are changed by large concentrations of internally generated helium. Because of high (n,α) cross sections significant quantities of helium will be produced in fusion reactor materials irradiated by 14 MeV neutrons in a relatively short time span. A concentration of 25-50 appm helium will be produced internally in niobium by a fusion neutron flux of $\sim 10^{18}$ neutrons $m^{-2}sec^{-1}$ with one year's exposure. Helium atoms produced at a high concentration in a host matrix having low helium solubility, are thermodynamically unstable and have a high driving force to coalesce in the microstructure at various defects. Thus, helium atoms tend to migrate to dislocations, precipitates, grain boundaries impurity particles and microcracks where they coalesce to form bubbles. These helium-induced defects generally cause embrittlement.

Changes in the mechanical properties of Nb and Nb-1%Zr doped with ^3He by the "tritium trick" method to as high as 500 appm are under investigation.

2. Helium Doping Procedure

The niobium and Nb-1Zr materials used in this study were ordered in wrought form. Sheets were cross-rolled to 1.59 mm (.0625 in.) thickness with a 50% reduction on the final pass. Before use in the tritium trick process, niobium specimens were given a two-hour anneal at 1200°C, and the Nb-1Zr specimens were annealed at 1600°C for one hour. Pressures in the furnace chamber were less than 1.3 μPa (10^{-8} torr) in all the annealing runs. These initial heat treatments produced microstructures with uniform, equiaxed grains. The average grain size in both materials was 50 μm.

Helium is charged into niobium or Nb-1Zr by first dissolving about 5 atom percent tritium in the metal at elevated temperature. The specimens are held at constant temperature, and the tritium undergoes a spontaneous radioactive decay to helium by the reaction $^3H \rightarrow {}^3He + \beta^-$. When the desired level of ^3He has been introduced into the metal, most of the tritium is removed by vacuum extraction at the same temperature used in charging.

The helium doping procedure is as follows: Niobium (or Nb-1Zr) pieces are weighed and placed in the reaction vessel. The vessel is evacuated and then back-filled with high purity helium. The reaction vessel is placed into a resistance heated furnace that is enclosed in a secondary containment vessel. This outer vessel is evacuated to 4 Pa. Temperature is controlled at 400°C by monitoring thermocouples spaced regularly along the external wall of the inner vessel. The inner vessel is evacuated to 4 Pa and purged with high purity helium several times to dilute and remove gaseous impurities from the system. After final evacuation to 4 Pa, the hot inner chamber is filled with a predetermined amount of tritium which

is controlled by precise volumetric techniques. The amount of tritium required in the system is the sum of that dissolved in the niobium or Nb-1Zr giving a metal-to-tritium atom ratio of 20 and an equilibrium pressure of 1.33 kPa (10 mm Hg) around the specimens at 400°C. Under these conditions helium is formed in the specimens at a rate of 7 appm per day. Constant temperature of 400°C is maintained until a preselected concentration of ^{3}He is introduced into the metal microstructure. Most of the tritium is subsequently removed by evacuating the system at 4 Pa for one week at 400°C. Next, the reactor is cooled and the various specimens are transferred to a second reaction vessel attached to a vacuum system capable of 133 μPa (10^{-6} torr). After purging with helium, this vessel and its contents are heated to 550°C for 170 hr (∿ 1 week) to lower the tritium concentration in the specimens to a level where specimens ran be handled safely by standard laboratory techniques. Residual tritium concentrations are typically less than 10 appm. Helium analyses for selected specimens are done in a precision mass spectrometry system at Atomics International.[2]

3. Tensile Test Procedure

Short term tensile tests are done in a stainless steel clamshell furnace mounted on an Instron Universal testing machine. All flange seals are Viton, and a six-inch diffusion pump coupled with a liquid nitrogen cold trap provide testing pressures less than 13 μPa (10^{-7} torr). This unit has a tungsten mesh heating element and heat shields and a copper cold wall. Tensile loads are applied through a metal bellows at the base of the furnace chamber.

4. Results and Discussion

The tensile properties of Nb and Nb-1%Zr at temperatures up to 800°C as a function of helium concentration are given in Tables III and IV. For Nb, the helium causes an increase in yield strength at temperatures above room temperature and some loss in ductility at high helium concentrations. For Nb-1%Zr alloy, the strengthening effects and losses

Table III Tensile Tests on Nb

Helium (appm)	Test Temp. °C	Yield Stress MPa	(ksi)	Ultimate Stress MPa	(ksi)	Elongation %	Reduction in area %
0	23	122	(18)	202	(30)	62	95
25	23	123	(18)	206	(30)	60	95
100	23	126	(18)	212	(31)	46	85
250	23	111	(16)	202	(30)	35	55
500	23	117	(17)	212	(31)	30	50
0	200	43	(6)	150	(22)	41	95
25	200	72	(10)	175	(25)	46	95
0	400	32	(5)	125	(18)	41	95
25	400	58	(8)	151	(22)	41	95
0	600	44	(6)	125	(18)	42	95
25	600	61	(9)	123	(18)	48	95
0	800	23	(3)	64	(9)	69	95
25	800	31	(5)	62	(9)	64	95
100	800	66	(10)	76	(11)	65	80
250	800	52	(8)	71	(10)	59	80
500	800	56	(8)	75	(11)	50	80

Table IV Tensile Tests on Nb-1%Zr

Helium (appm)	Test Temp. °C	Yield Stress MPa	(ksi)	Ultimate Stress MPa	(ksi)	Elongation %	Reduction in area %
0	23	150	(22)	260	(38)	53	95
25	23	165	(24)	279	(41)	46	95
100	23	234	(34)	355	(52)	36	65
0	200	106	(15)	202	(29)	43	95
25	200	92	(13)	194	(28)	45	95
100	200	158	(23)	275	(40)	30	85
0	400	102	(15)	202	(29)	27	95
25	400	92	(13)	194	(28)	33	95
100	400	147	(21)	244	(35)	30	75
0	600	70	(10)	222	(32)	32	95
25	600	85	(12)	208	(30)	31	95
100	600	*116*	(17)	236	(34)	25	55
0	800	65	(9)	204	(30)	31	95
25	800	78	(11)	221	(32)	27	65
100	800	186	(25)	292	(42)	12	30

in ductility caused by helium were more pronounced, particularly at a concentration of 100 appm. The loss in ductility at 800°C in the specimen containing 100 appm helium should be noted. The combined effect of temperature and deformation may lead to rearrangement of helium in the metal matrix causing deleterious changes in the microstructure. Electron microscopy observations showed a homogeneous distribution of helium in as-charged specimens at 25 appm, but as the helium concentration increased, there was a greater tendency for helium bubbles to form on grain boundaries.

Fractured specimens were examined with a scanning electron microscope, and all fractures were ductile-dimple. No evidence of brittle fracture was found in any of the test specimens.

VI. REFERENCES

1. B. A. Loomis and S. B. Gerber, "Effect of Oxygen Impurity on Defect Agglomeration and Hardening in Neutron-Irradiated Niobium", Acta Met, 21, p. 165 (1973)

2. H. Farrar, IV, W. N. McElroy, and E. P. Lippincott, "Helium Production Cross Sections of Boron for Fast-Reactor Neutron Spectra", Nucl. Technol., 25, p. 305 (1975)

VII. FUTURE WORK

A. 14 MeV Neutron Damage - Study irradiation damage in 316 stainless steel.

8. Effect of Helium on Mechanical Properties of Nb and Nb-1%Zr - Study creep behavior of Nb doped with helium.

I. PROGRAM

Title: Simulating the CTR Environment in the HVEM
Principal Investigator: D. Kuhlmann-Wilsdorf
Affiliation: University of Virginia

11. OBJECTIVE

The objective of this work is to evaluate the effects of helium and irradiation on the fracture of 304 and 316 stainless steel.

III. RELEVANT DAFS PROGRAM TASK/SUBTASK

SUBTASK II.C.8.2 Post-Irradiation Testing

IV. SUMMARY

In-situ HVEM tensile tests of unirradiated 316 stainless steel and neutron irradiated 304 stainless steel samples from EBR-II were performed at room temperature and at 600°C.

Typical crystallographic crack formation was observed during the ductile failure of the unirradiated samples. Irradiated samples failed in a brittle mode with preexisting dislocation loops acting to promote plastic deformation around the crack. Preexisting voids enlarged in diameter by a factor of two when the crack propagated near them at 600°C. No strong evidence of helium embrittled grain boundary cracking has been observed yet.

V. ACCOMPLISHMENTS AND STATUS

A. In-Situ HVEM Tensile Tests of Irradiated and Unirradiated Stainless Steel -- W. A. Jesser, J. A. Horton and 3. I. Bennetch, University of Virginia, Charlottesville VA.

1. Introduction

Comparisons on the differences in modes of fracture of unirradiated and irradiated bulk material have been carried out in some detail in the past. In order to improve theoretical fracture models attempts have been made to correlate gross property changes with observed microstructural differences in the specimens. In the literature many articles have been published showing micrographs of alterations in the interior and on the surfaces of the fractured material obtained by using optical and electron microscopy. A necessary companion to these bulk studies is the in-situ examination of fracture in a high voltage electron microscope (HVEM), which would enable one to view detailed changes in microstructure as deformation progresses. Saka, Noda, Matsumoto, Imura at Nagoya University have employed a high temperature tensile device in a 1 MeV HVEM to study dislocation behavior in irradiated nickel.[1] Valle, Martin and Stohr have designed a similar tensile stage to that used in Nagoya University for the research 3 MeV facility at Toulouse, France.[2] At the University of Virginia, dynamic in-situ fracture with a 500 KeV HVEM have previously been accomplished with various materials including stainless steel.[3,4] This present work is a preliminary examination of microstructural changes as fracture progresses in neutron irradiated stainless steel as compared

to helium irradiated and nonirradiated stainless steel.

2. Experimental Data

The tensile tests reported here were conducted in a RCA 500 kV electron microscope at the University of Virginia. The loading force in the tensile stage is provided by a spring restrained by a fluid filled bellows. As fluid escapes the bellows through a controlled leak a mechanically smooth pulling action occurs over a wide range of regulated elongation rates. The stage also allows heating to 600°C and a single axis of tilt.[5]

A 200 kV ion accelerator is attached to the microscope so that the light ion beam can strike the sample inside the HVEM while the sample is under observation.

The non-irradiated samples were type-316 stainless steel, 40 μm thick, obtained from A.D. Mackay, Darien, CT. They were annealed at 1200°C for one hour and electropolished at room temperature in 10% perchloric acid and 90% acetic acid. The two irradiated samples (type 304 stainless steel) were irradiated at about 375°C in the EBR II and were provided by J. O. Stiegler at ORNL.[6] These samples were obtained from bulk tensile specimens by mechanically lapping to 0.2 mm before punching. The samples were then electropolished to perforation under the same conditions as for the unirradiated samples. The sample of Experiment 5 showed a high defect cluster density (4×10^{14} cm^{-3}) and a low density (10^8-10^9 cm^{-3}) of 200 nm diameter voids while the sample of Experiment 4

showed a high density (10^{14} cm^{-3}) of 30 nm diameter voids. The experimental conditions for the HVEM in-situ tensile tests are summarized in the table.

SUMMARY OF **IN-SITU HVEM** TENSILE EXPERIMENTS

Experiment Number	Sample Type	Test Temperature
1	316 Stainless Steel (SS)	600°C
2	316 Stainless Steel	600°C
3	316 Stainless Steel	Room Temperature
4	Irradiated 304 SS	600°C
5	Irradiated 304 SS	Room Temperature

3. Results and Discussion

Room temperature tensile tests on unirradiated samples showed that the fracture behavior and crack propagation mode were similar to that previously reported in the literature.[3] For example, in Experiment 3 the familiar hole formation in front of the crack tip occurred. Also a crystallographic tooth-like fracture occurred in the plastic region, see Figure 1. The crack tip (radius around 150 nm) was preceeded by a long plastic region which is consistent with high ductility and extensive dislocation motion.

The high temperature (600°C) unirradiated samples behaved similarly. The crack tip radius was about 100 nm. The plastic zone ahead of the crack was longer than the room temperature experiment. Some of the same crystallographic cracking occurred however it was less pronounced as may

be expected at high temperature where dislocation climb is active.

The neutron irradiated sample which was pulled at room temperature (Experiment 5) showed a high defect density with a few large (220 nm) voids. The crack tended to propagate in the thinner areas along microstructural slip bands instead of grain boundaries. The mode of fracture appeared more brittle as evidenced by a smaller plastic region in front of the crack tip but still bole formation ahead of the crack occurred. The crack tip radius was about 100 nm which is the same value obtained for the unirradiated samples pulled at 600°C. The final fracture itself tended not to follow crystallographic lines but still pulled out some ligaments along the flanks of the cracks. Preliminary observations on these samples suggest that the unfaulted dislocation loops present after neutron irradiation may contribute to the plastic deformation associated with crack propagation by elongation of the dislocation loop.

The irradiated sample that was pulled at 600°C exhibited a high void density (10^{14} cm^{-3}). This sample had very steep walls, i.e. little electron transparent area, with a round electrothinned hole showing no preexisting cracks. Crack initiation was observed to be at 90" to the tensile axis. No grain boundary, second phase particle or other microstructural feature was observed as a nucleation site for the crack. In this case the crack tip radius of 200 nm is larger than that of the other cases. Ahead of the crack tip very little plastic deformation occurred but the voids within a region which extended about 200 nm from the flank of the crack enlarged from their original 30 nm to around 60 nm in diameter.

The shape of the enlarged voids at the crack flanks seemed to be slightly elongated with no obvious correlation to the direction of crack (see Figure 2). Scanning electron microscope observations of the fracture surface showed a void sheet of very large (250 to 1200 nm) voids commonly referred to as dimples. It is likely that an area which exhibited small dimples experienced a large deformation rate with the area with large dimples likely experienced a slow deformation rate.

ACKNOWLEDGMENT

The authors thank H. G. F. Wilsdorf for his advice and suggestions.

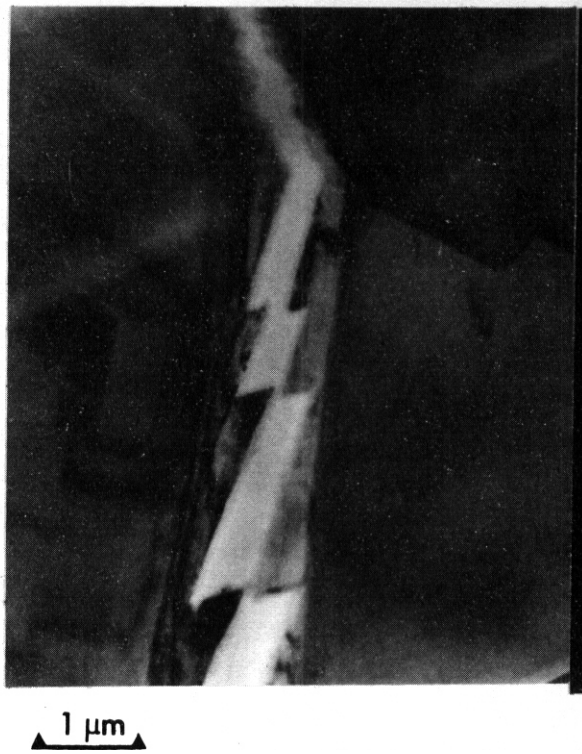

Figure 1

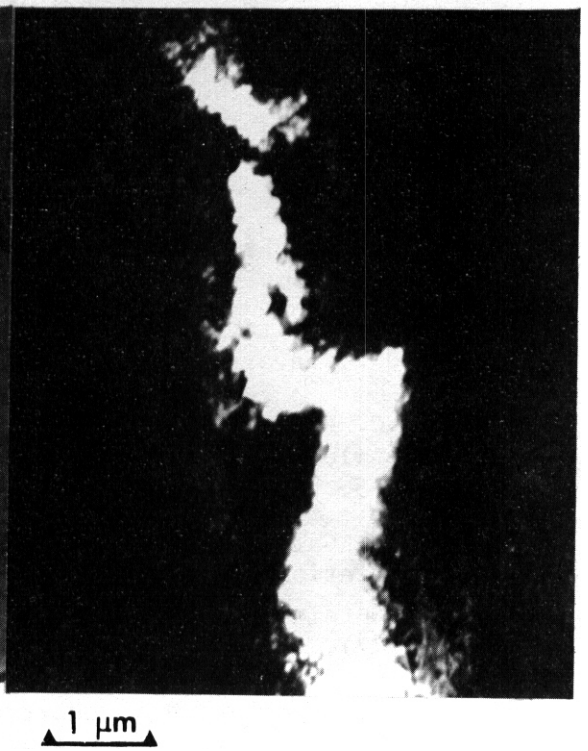

Figure 2

FIGURE 1 *400* kV Electron Micrograph of Unirradiated *316* SS Fractured at Room Temperature. Note the Tooth-Like Plastic Region in the Crack.

FIGURE 2 *400* kV Electron Micrograph of Neutron Irradiated *304* SS Fractured at 600°C. Note the Void Enlargement at the Crack Flanks and at the Crack Tip.

VI. REFERENCES

1. H. Saka, K. Noda, K. Matsumoto and T. Imura, Proc. 4th Int. Conf. on HVEM, B. Jouffrey and P. Favard, Eds., p. 325 (1976)

2. R. Valle, J. L. Martin, J. F. Stohr, "In-Situ Experimentation; Side-Entry Straining Stage with Heating and Double Tilting Facilities; Role of Dislocation Pile Ups in the Deformation of Composite Materials" Proc. 4th Int. Conf. on HVEM, B. Jouffrey and P. Favard, Eds., pp. 59-62 (1976).

3. H. G. F. Wilsdorf, "Void Initiation, Growth, and Coalescence in Ductile Fracture of Metals", J. of Electronic Materials, 4, no. 5, pp. 791-809 (1975).

4. R. N. Gardner, T. C. Pollock and H. G. F. Wilsdorf, "Crack Initiation at Dislocation Cell Boundaries in the Ductile Fracture of Metals", Materials Science and Engineering, 29, pp. 169-174 (1977).

5. J. I. Bennetch, J. A. Horton and W. A. Jesser, "Ion Accelerator-HVEM Link", Proc. 35th Annual Meeting EMSA, Ed. by G. W. Bailey, p. 96 (1977).

6. E. E. Bloom, J. O. Steigler and C. J. McHargue, "Radiation Damage in Annealed Type 304 Stainless Steel", Radiation Effects 14, pp. 231-243 (1972).

VII. FUTURE WORK

Tensile tests will be continued in order to compare the fracture mechanisms of neutron irradiated samples to the unirradiated samples. Further fracture tests of in-situ HVEM helium irradiated samples will be performed. These samples will be irradiated to various fluences and defect structures in an effort to elucidate in a controlled manner the mechanisms of helium embrittlement and the role of preexisting microstructural features to the tensile test results.

I. PROGRAM

Title: Irradiation Response of Materials
Principal Investigators: J. A. Spitznagel, W. J. Choyke
Affiliation: Westinghouse Research and Development Center

II. OBJECTIVE

The objective of this work is to assess the phenomenology and mechanisms of microstructural evolution in materials exposed to simultaneous helium injection and creation of atomic displacement damage by a second ion beam.

III. RELEVANT DAFS PROGRAM PLAN TASK/SUBTASK

SUBTASK II.C.11.1 Light Particle Irradiations

IV. SUMMARY

Current emphasis is on scaling uniaxial tension specimens to determine the effects of specimen size, geometry, and microstructure on the stress-strain response. The scaling studies are being funded from sources outside DOE.

I. PROGRAM

Title: Effects of Irradiation on Fusion Reactor Materials
Principal Investigator: F. V. Nolfi, Jr.
Affiliation: Argonne National Laboratory

II. OBJECTIVE

The objective of this work is to establish a correlation between the net point defect production rates obtained during light-ion and neutron irradiations that have the same calculated damage rates deduced from exposure parameters.

III. RELEVANT DAFS PROGRAM PLAN TASK/SUBTASK

SUBTASK II.C.II.I Light Particle Irradiations

IV. SUMMARY

Transfer of the Torsional-Creep Apparatus from the Hanford Engineering Development Laboratory to ANL has been completed. Repairs of irradiation damaged and malfunctioning electronic equipment are underway and installation of the apparatus at the ANL Cyclotron is in progress.

V. ACCOMPLISHMENTS AND STATUS

Damage Correlation -- H. Yamada

The method we use to establish a link between the damage produced in first-wall materials by ions and neutrons with energies similar to those of the fusion reactor regime is by load-relaxation and creep measurements where the deformation is climb-controlled. The rate of climb-controlled plastic deformation is proportional to the rate at which an excess of vacancies or interstitials arrives at dislocations. Since these

measurements are flux sensitive and do not depend upon fluence during the short test time involved, irradiation can be performed in low-flux neutron environments without prohibitively long experimental times. As a result, microstructure can be controlled, and the measurements are more sensitive and accurate than, for example, void-growth measurements. In this type of study, experimental measurements of load relaxation and creep are made under the influence of Cyclotron (light-ion) bombardments and high-energy neutron irradiation. These data are used to correlate the effective displacement rates that obtain during irradiation with neutrons and energetic light ions. Neutron data are obtained from, for example, experiments in Cyclotron-based Be(d,n) sources. The damage correlation between energetic light ions and heavy ions is made on the basis of void-growth and other microstructural data that are readily obtained.

VI. REFERENCES

None

VII. FUTURE WORK

Upon completion of the installation and repair of the torsional-creep apparatus, it will be checked out by performing thermal-creep measurements on Type 316 stainless steel. Following successful testing, creep measurements on this material will be made during alpha-particle bombardment at the ANL Cyclotron. These initial experiments will be carried out in collaboration with Eric Opperman of the Hanford Engineering Development Laboratory.

VIII. PUBLICATIONS

H. Yamada, "Effect of Fast-neutron Irradiation on Plastic Deformation of Type 304 Stainless Steel," submitted for publication in the Proc. of the Symposium on the Metal Physics of Stainless Steels, AIME Annual Meeting, February 26-March 2, 1978, Denver, Colorado.

I. PROGRAM

Title: Effects of Irradiation on Fusion Reactor Materials
Principal Investigator: F. V. Nolfi, Jr.
Affiliation: Argonne National Laboratory

II. OBJECTIVE

The objectives of this work are to determine, using light-ion irradiations of miniature specimens, the relationship between changes in mechanical behavior, and irradiation and irradiation-induced microstructure with special emphasis on the effects of helium.

III. RELEVANT OAFS PROGRAM PLAN TASK/SUBTASK

SUBTASK II.C.12.1 Light Ion Irradiations

IV. SUMMARY

During the early part of FY 1978, the mechanical behavior activity has been concentrated on preparations for the experimental programs. The hydraulic mechanical testing system has been ordered and is to be delivered later in FY 1978. An environmental chamber for irradiation of miniature mechanical test specimens using a helium beam from the ANL Cyclotron has been designed and will be constructed by the time the mechanical testing system is available. Type 316 stainless steel (HT No. 15893) has been obtained from the Magnetic Fusion Energy (MFE) stockpile and is being processed into suitable form for the program needs.

V. ACCOMPLISHMENTS AND STATUS

Effects of Irradiation and Irradiation Microstructure on Mechanical Behavior -- A. P. L. Turner

The information available to predict mechanical properties such as ductility and creep rates from quantitatively characterized microstructures is very limited. This work is designed to obtain information about the relations between microstructure and mechanical properties during and after irradiation. Because of cost and environmental-control considerations, miniature test specimens will be employed in this investigation to a large extent so that mechanical tests can be conducted during high-energy charged-particle irradiations. Although the question of quantitative predictions of design data from results on miniature test specimens has not been resolved, little doubt exists about the usefulness of the well-established qualitative correlations between results on miniature and on bulk mechanical test specimens for alloy development.

Miniature tensile specimens of annealed and 20% cold work Type *316* stainless steel (MFE reference material) have been fabricated and are being prepared for alpha-particle injection in the ANL Cyclotron.

VI. REFERENCES

None

VII. FUTURE WORK

The miniature tensile specimens will be injected with He at room temperature to various concentrations. After elevated temperature annealing, these specimens will be tested at temperature and the behavior of the annealed material will be compared to that of 20% cold-worked material. Transmission and scanning electron microscopy will be performed on the specimens in both the as-injected and post-testing conditions. When the environmental chamber becomes available, the results of these tests will be compared to similar tests but where the He has been injected at elevated temperatures.

VIII. PUBLICATIONS

None

I. PROGRAM

Title: Irradiation Response of Materials

Principal Investigators: J. A. Spitznagel, W. J. Choyke

Affiliation: Westinghouse Research and Development Center

II. OBJECTIVE

The objective of this work is to assess the phenomenology and mechanisms of microstructural evolution in materials exposed to simultaneous helium injection and creation of atomic displacement damage by a second ion beam.

III. RELEVANT OAFS PROGRAM PLAN TASK/SUBTASK

SUBTASK II.C.18.1 Nucleation Experiments

IV. SUMMARY

Emphasis during this reporting period has been on the "baseline" or calibration experiments required for program start-up. Choice of bombarding ion was based on consideration of primary recoil spectra calculations and solubility and diffusivity of the implanted ions. Beam heating calculations and experiments and ion milling (target sectioning) calibrations were completed. Type 316 stainless steel from the Magnetic Fusion Energy (MFE) heat was processed to produce targets suitable for irradiation with co-impinging ion beams. Thermomechanical processing was chosen to produce initial microstructures identical with those for the MFE-I neutron irradiation experiments.

Tailoring of the helium concentration profile to match the "flat" damage energy deposition region for the second ion beam was achieved. Design and construction of a residual gas analyzer which will permit

in-situ measurements of the gaseous environment in the target chamber during ion bombardment of the reactive refractory metals were initiated. Initial experiments to determine the effects of helium implantation technique on void and dislocation loop nucleation in 20% cold worked 316SS are in progress.

V. ACCOMPLISHMENTS AND STATUS

A. Introduction

The simultaneous production of helium from (n,α) reactions and atomic displacement damage by energetic neutrons in reactor structural alloys is expected to have a strong influence on their irradiation response for first wall and structural applications in fusion power reactors. Previous studies in a fission reactor environment have indicated that high and low helium generation rates result in markedly different void and dislocation structures in an austenitic stainless steel.[1] Charged particle bombardment offers the possibility of assessing the phenomenology and mechanisms of microstructural evolution in a wide range of materials exposed to simultaneous helium injection and creation of atomic displacement damage by a second ion beam. In this program two ion accelerators are used to simultaneously focus a beam of helium ions and a second ion beam on targets of selected reactor structural alloys. The resulting microstructural changes will be studied for systematic variations in damage rate, irradiation temperature, fluence and appm helium/dpa ratio and compared and correlated with results from companion fission reactor and high energy neutron irradiation studies conducted elsewhere in the Division of Magnetic Fusion Energy Program. The initial efforts in the program are being directed to a careful characterization of helium and damage energy profiles, temperature control and other aspects of environmental control on two model materials.

8. Target Preparation

To facilitate comparison with the proposed MFE-I and MFE-II experiments in the Oak Ridge Research Reactor, it was decided that 316SS from the MFE heat would be used as a model material for the austenitic class of alloys. To date only a few square inches of solution annealed and 20% cold rolled strip obtained from Oak Ridge National Laboratory (ORNL) have been processed. Additional material from this heat in the form of 5/16" (0.8 cm) thick plate was received January 10, 1978, from ORNL. Approximately sixty (60) 3 mm diameter discs have been prepared from the available material for the target bonding, beam heating, ion milling and dual ion irradiation experiments.

Figure 1 is a schematic representation of the target preparation technique that was developed during this reporting period. It offers the advantages of controlling the initial microstructure of the 316SS and providing excellent heat sinking of the target during high energy dual ion beam bombardment. To begin the process, 3 mm discs are punched from ~0.5 mm thick cold rolled strip. To study specimens in the annealed condition, discs are first partially punched from cold rolled strip. The strip itself then serves as a holder for the discs during a subsequent high temperature solution annealing treatment. Following annealing, the discs are lightly tapped free from the strip. Both cold worked and annealed discs are lapped through several stages to produce parallel-sided targets approximately 0.2 mm thick. The surface to be bombarded (front surface) is finished with 0.1 μm diamond abrasive. The back surface is then plated with copper and placed in a cylindrical molybdenum holder with a conical recess as shown in Fig. 1. It has been found that by evaporating Cr and Au on the surface of the conical recess, an adherent copper layer can be plated onto the tapered sides. With the specimen held in position on the holder by a layer of lacquer, a very excellent bond can be obtained between the Cu-plated disc and the holder if a pointed copper rod is

inserted into the recess to serve as the anode during a subsequent electroplating operation.

Figure 2 is a photograph of the teflon rig which has been designed and constructed to permit the copper bonding of nine stainless steel target/molybdenum holder assemblies. Approximately two weeks of continuous electroplating are required to produce nine targets adequately bonded for high energy ion bombardment.

As a final step in target preparation, approximately 10 μm of material is removed from the surface to be bombarded by electropolishing using a jet of perchloric-acetic acid as the electrolyte. This has been found adequate to remove the debris layer from the lapping operations and results in a strain-free surface. The "dimple" has a very large radius of curvature so that a surface profilometer can be used to measure "step-heights" after ion bombardment or ion milling.

Following ion bombardment, the targets are easily removed from the Mo holders by dissolving the copper using a nitric acid solution.

C. Target Temperature Control and Beam Heating Experiments

To determine whether the temperature measured during ion bombardment (by a spring-loaded thermocouple pressing against the Cu-plating in the conical recess of the molybdenum target holder) accurately represents the target temperature, a number of heat flow calculations and beam heating experiments were conducted. These will be briefly summarized.

Consider a target of thickness **t** under bombardment by an energetic beam of ions as shown schematically below.

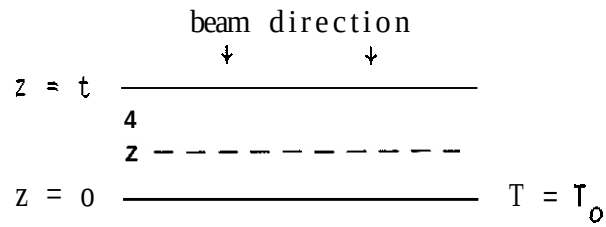

z = thickness

T = temperature in °C

The temperature gradient normal to the foil surface can be estimated as follows: Past any plane at z, the heat flow in joules/cm^2/sec =

$$JK \frac{\partial T}{\partial z} - j_Q$$

where j = 4.184 joules/cal

K = cal/cm·sec·°C ≃ 0.1 for 316SS

≃ 0.9 for Cu.

If $(S_n + S_e)$ is the total stopping power of the ions in the target, dE/dz, and ϕ is the flux (ions/cm^2·sec), then j_Q toward $z = 0$ must increase as z increases.

$$\partial jQ/\partial z = (S_n + S_e)\,\phi$$

$$\text{or} \quad \partial^2 T/\partial z^2 = (S_n + S_e)\,\phi/JK$$

$$(\partial T/\partial z)\Big|_z = (\phi/JK)\int_{z'=z}^{t} (S_n + S_e)\,dz'$$

For a "worst case" approximation, assume all of the energy loss from the ions occurs at $z = t$ corresponding to

$$(S_n \; t \; S_e) = \Delta E \cdot \delta(t - z)$$

then $\partial T/\partial z = \phi \cdot \Delta E/JK$

and $T_{MAX} = T_o + (\phi \Delta E t)/JK$

if we take $\phi \Delta E \sim 50$ watts/cm^2

$$(T_{MAX} - To) = (50/4.18)\ (t/K)$$

If $t \sim 0.2$ mm and $K = 0.1$

then $\Delta T_{MAX} = 2.4°C$

Unless there would be a gross change in thermal conductivity induced by radiation damage, we conclude that the temperature variation with depth in the target can be ignored. The remaining question is the effect of the contact resistance between the thermocouple bead and the holder. This was addressed experimentally by using a beam of 2 MeV helium ions to bombard Cu-bonded target/holder assemblies with the thermocouple bead either spring loaded against the holder or copper brazed into the conical recess. The brazing was done with an electron gun in vacuum. The ion current was adjusted to pump 5 watts into the target in each case. This is approximately the rate of energy deposition under dual ion irradiation using 28 MeV Si^{+6} ions with a beam current (total) of ~ 1 μA. The external furnace was adjusted to give a steady state temperature of 500°C with the beam on and the thermocouple brazed into the holder. With identical beam current and temperature setting, the indicated temperature was again 500°C ± 5°C if the bead was spring loaded against the copper backing. From the results of these calculations and measurements it was concluded that there is no significant difference between the temperature of the beam-heated sample and the temperature indicated by a thermocouple placed in good mechanical contact with the back of the molybdenum holder.

D. Ion Milling Calibration

Sectioning dual ion irradiated targets to various depths along the damage energy curve for the high energy ions requires a very reproducible, accurate technique. Previous experience with 304SS in this laboratory has indicated that ion milling with 800 eV krypton ions while continuously rotating the target to minimize anisotropic (crystallographic) sputtering effects is well suited for this purpose. With this technique it is possible to remove several microns of material within a few hours with an accuracy of ~10-20%. The thickness of the sputtered layer is determined by partially masking the surface and measuring the step at the interface of the masked and sputtered areas using a stylus profilometer.

Figure 3 is a calibration curve for ion milling 316SS from the MFE heat in both solution annealed and 20% cold rolled condition. Also shown are the results obtained for a 304SS used in ion bombardment studies as part of another research program in our laboratories. Both solution annealed and cold worked samples of the 316SS were milled at the same rate (within the scatter band of the data). The difference in milling rates observed for the 316SS and 304SS is somewhat surprising since the difference in composition is mainly the addition of 2-3% Mo to the 316SS.

The surfaces of the samples used in the calibration were prepared with exactly the same procedures used to prepare targets for dual ion irradiation. Previous experience has shown that the calibration curves can be used to select approximate milling times for post-bombardment sectioning although profilometer measurements must still be made on the actual targets.

E. Selection of Second Ion Beam and Range Matching

For the dual ion irradiation experiments a number of ions could be used to serve as the "primary beam," i.e., the ions responsible for most of the lattice damage. Since the implantation of helium results in

only ~0.1 dpa per 1000 appm He[2], the primary beam must produce the bulk of the damage for doses on the order of ~1-50 dpa. This dose range will be most useful for comparison with the results of the fission and 14 MeV neutron irradiation experiments currently planned. We have selected 28 MeV silicon ions for the primary beam based on the following considerations:

1. Theoretical calculations[3,4] indicate that differences in primary recoil energy spectra over a wide range of incident ion masses and energies are small.

2. The calculated root mean square fluctuation in projected range (straggle) is small (~0.26 μm) and the permeability (solubility and diffusivity) of silicon in stainless steel is small over the temperature range of interest. Hence, data can be taken without concern about doping effects from the implanted silicon. Experience gained in other radiation damage experiments in our laboratories has indicated that silicon doping effects in stainless steel targets bombarded at 500-750°C can be avoided if data are taken at depths at least three standard deviations away from the projected range (R_p) of the silicon ions (assumes a gaussian concentration profile).

3. Adequate beam Currents of silicon ions are available.

4. Tailoring of the helium concentration profile to match the damage energy curve for 28 MeV silicon ions could be achieved at the High Energy Ion Bombardment Simulation (HEIBS) facility. This tailoring permits data to be taken at constant appm He/dpa ratio over a depth of several microns.

Figure 4 shows the calculated damage energy profile for the 28 MeV Si^{+6} ions in 316SS and schematically depicts the concentration profiles for the implanted helium and silicon ions. The calculations were

performed using a modified version[5] of the E-DEP-1 code. The modifications described in reference (5) permit more accurate values of the electronic stopping power to be used in the calculations. From Fig. 4 and the preceding discussion it can be concluded that data can be obtained from a region extending approximately 3.5 μm from the as bombarded surface.

F. Design of a Residual Gas Analyzer System Compatible with Dual-fon Beam Bombardment Requirements

Some refractory metals which appear to have useful characteristics for fusion applications unfortunately act as "getters" at operating temperatures of interest. Any radiation damage study on such materials has to take this into account. In selecting reactive/refractory metals for various fusion reactor applications, it will be important to know and understand the impact of the vacuum conditions on the microstructural changes resulting from ion bombardment at elevated temperatures.

One can approach this problem by settling for nothing but ultra-high vacuum ($<10^{-9}$ torr) around the bombarded samples. At the present time this would present severe problems for doing dual beam experiments in our facility. A compromise approach is to settle for a vacuum of about 10^{-7} torr and attempt to measure the species of atoms and molecules near the bombarded surface. In fact, we believe that at this stage the latter scheme is a much more practical and fruitful one to pursue.

Having decided on the residual gas analysis approach we first consulted with acknowledged experts in the field. Figure 5, which incorporates many of their suggestions, shows the planned geometry for implementing the residual gas analysis and the additional pumping to make such an arrangement workable. Care must be taken that the ion-beam measurements on our samples are not interfered with by electrons from the ionizer in the Q.M.S. (Quadrupole Mass Spectrometer). An isolation scheme, a pair of overlapping apertures, and a shutter have been designed

for this purpose. The following specifications on the Q.M.S. were felt to be necessary requirements:

1. Mass Resolution: Capable of mass resolving fractional masses. Guaranteed to show 20% valley resolution between ions separated by 0.037 mass units or greater at masses up to 40 amu.

2. Mass Ranges: 0 to 64 amu at a frequency of 5.1 MHz and 1 to 500 amu at a frequency of 2.2 MHz.

3. Quadrupole: Dimensions of rods 3/8 x 9 inches with suitable field separation mechanism to achieve resolutions.

4. Sensitivity: 1 mA/Torr N_2 operating at 5.1 MHz before electron multiplication.

5. Pumping System: Turbomolecular pump with ultimate vacuum on low 10^{-7} torr range on blank off.

At present, the Q.M.S. and electronics are under construction at Extranuclear Laboratories, Inc. The new isolation sample chamber and furnaces are being built in our workshops. The present dual ion bombardment arrangement has already undergone major modifications to allow a rapid shift over to our new system as soon as the components are finished and have undergone acceptance tests.

G. Sequential and Simultaneous Ion Bombardment of 20% Cold Worked 316SS

The problems of designing reactor experiments requiring spectral tailoring to achieve constant appm helium/dpa ratios and pre-implanting helium into materials which will not experience sufficient helium generation by transmutation reactions are substantial. Charged particle

irradiation experiments will hopefully be able to provide some insight into the effects of helium implantation technique on microstructural evolution and on the need for spectral tailoring.

At present, two ion accelerators are being used to either sequentially or simultaneously implant helium ions and produce atomic displacement damage with 28 MeV Si^{+6} ions in 20% cold worked 316SS. In the sequentially bombarded targets, helium has been pre-implanted at temperaturesin the range 600°C to 750°C. The helium was distributed over a depth of several microns in the target by "chopping" a beam of 2 MeV helium ions with Al degrader foils of varying thickness. The helium concentration profile was also "tailored" to closely match the damage energy profile from the 28 MeV silicon ions. This resulted in a damage region extending from a depth of ~0.5 μm to 3 μm in the target over which the helium/dpa ratio was nearly constant. Bombardment with silicon ions has been conducted at the same temperature as the helium pre-injection. Simultaneous bombardment of companion targets with helium and silicon ions has been performed at temperatures identical to those used for the sequentially bombarded targets. Samples were bombarded to peak damage levels of ~30-40 dpa at each temperature. Calculated atomic displacement rates varied from ~6.4 x 10^{-5} dpa·sec^{-1} at the surface to ~1.2 x 10^{-3} dpa·sec^{-1} at the peak damage region. The appm helium/dpa ratio was maintained constant throughout these experiments at a value of ~11. Following bombardment the targets are being sectioned to various depths corresponding to different damage rates and fluences along the damage energy profile for the silicon ions. To avoid surface proximity and excess silicon effects, data are being taken from a 1.0 to 3.0 μm deep region.

TEM observations have revealed marked differences in microstructure depending on the helium implantation technique and ion bombardment temperature. In general, simultaneous helium implantation has resulted in void number densities approximately an order of magnitude larger and average void diameters ~5 times smaller than hot pre-implantation over

the entire temperature range stuaied. At a temperature of ~600°C, hot pre-injection of helium produced ~10^{14} voids/cm^3 but voids were no longer observed in the simultaneously implanted targets. Void sizes and no. densities varied by almost an order of magnitude in different areas of the same foil in the hot pre-implanted samples bombarded at temperatures above ~700°C, apparently as a result of partial recrystallization. No recrystallization (but some recovery) was observed in the simultaneously implanted targets at bombardment temperatures up to 750°C. For both helium implantation conditions voids formed mainly in dislocation cell interiors with few bubbles/voids associated with the dense dislocation tangles comprising the cell walls. Heterogeneous void formation on needle-shaped precipitates, but seldom on grain boundary carbides, were common features of both implantation techniques at bombardment temperatures above ~700°C.

The results suggest that the rate and temperature at which helium is implanted can strongly influence the nucleation and growth of voids, and microstructural stability of 20% CW 31655.

VI. REFERENCES

1. E. E. Bloom, F. W. Wiffen, P. J. Maziasz, and J. O. Stiegler, Nucl. Technology 31, P. 115 (1976).

2. D. J. Mazey and R. S. Nelson, "Radiation Effects and Tritium Technology for Fusion Reactors," USERDA Conf. 750989, Vol. I, P. 240 (1975).

3. A. D. Marwick, J. Nucl. Mater. 56, P. 355 (1975).

4. J. A. Spitznagel, R. M. More, W. J. Choyke and F. J. Venskytis, Trans. ANS, 26, P. 181 (1977).

5. R. M. More and F. J. Venskvtis. "Comparison of Range and Range Straggle Calculations," Accepted for publication in Radiation Effects Journal (1977).

VII. FUTURE WORK

The next step in assessing the effects of helium implantation techniques will be to expand the temperature range of the hot pre-implantation and simultaneous helium implantation experiments in 20% cold worked 316 SS in an attempt to map out the temperature and fluence dependence of the microstructural evolution at low doses (<20 dpa).

VIII. PUBLICATIONS

A paper entitled "Microstructural Effects of Hot Pre-Implantation and Simultaneous Implantation of Helium in Ion Bombarded 316 SS" has been accepted for presentation and possible publication for the 9th ASTM International Symposium on the Effects of Radiation on Structural Materials.

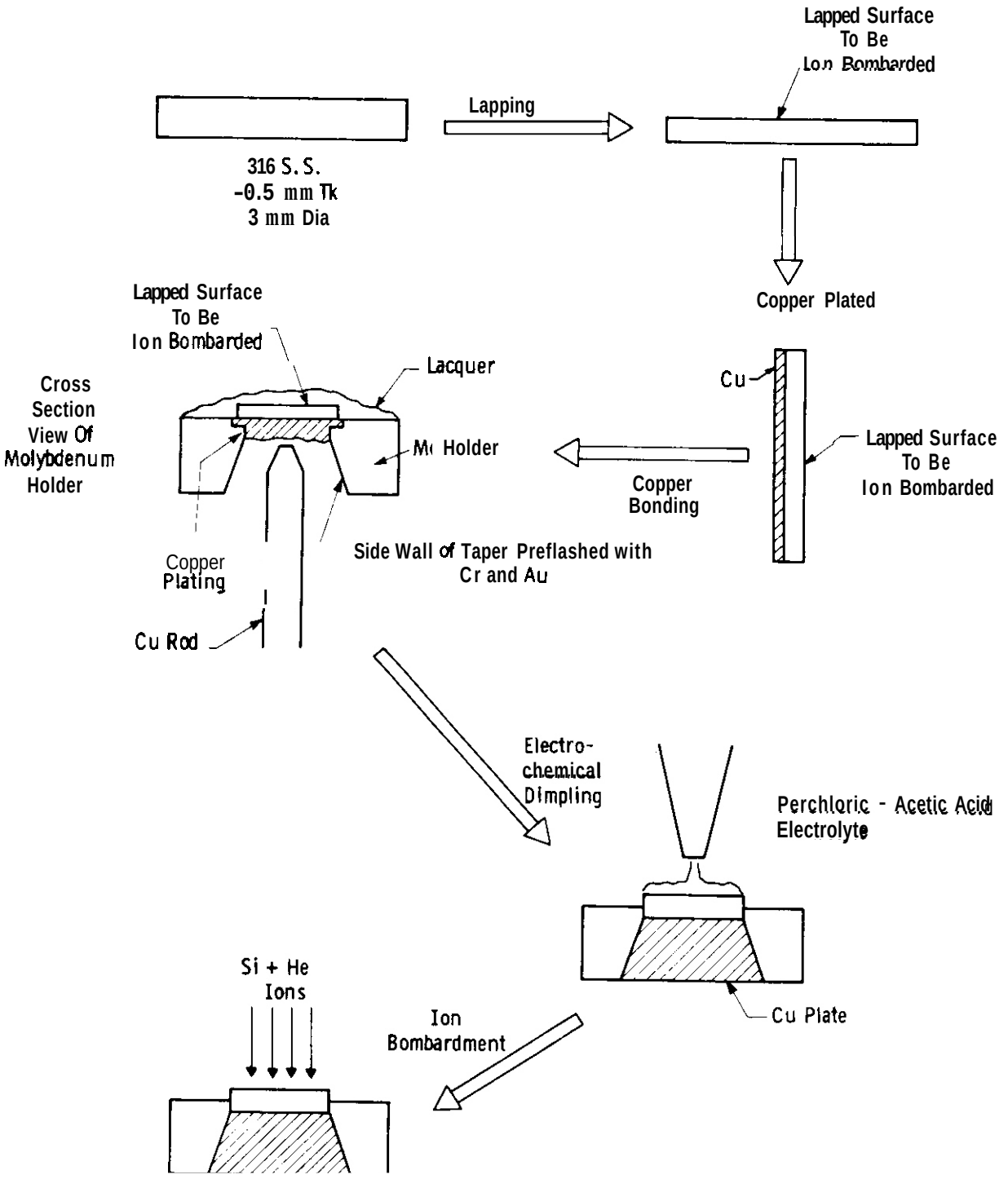

FIGURE 1. Schematic Depicting Sequence of Operations in Preparing 316 SS for Dual-Ion Bombardment.

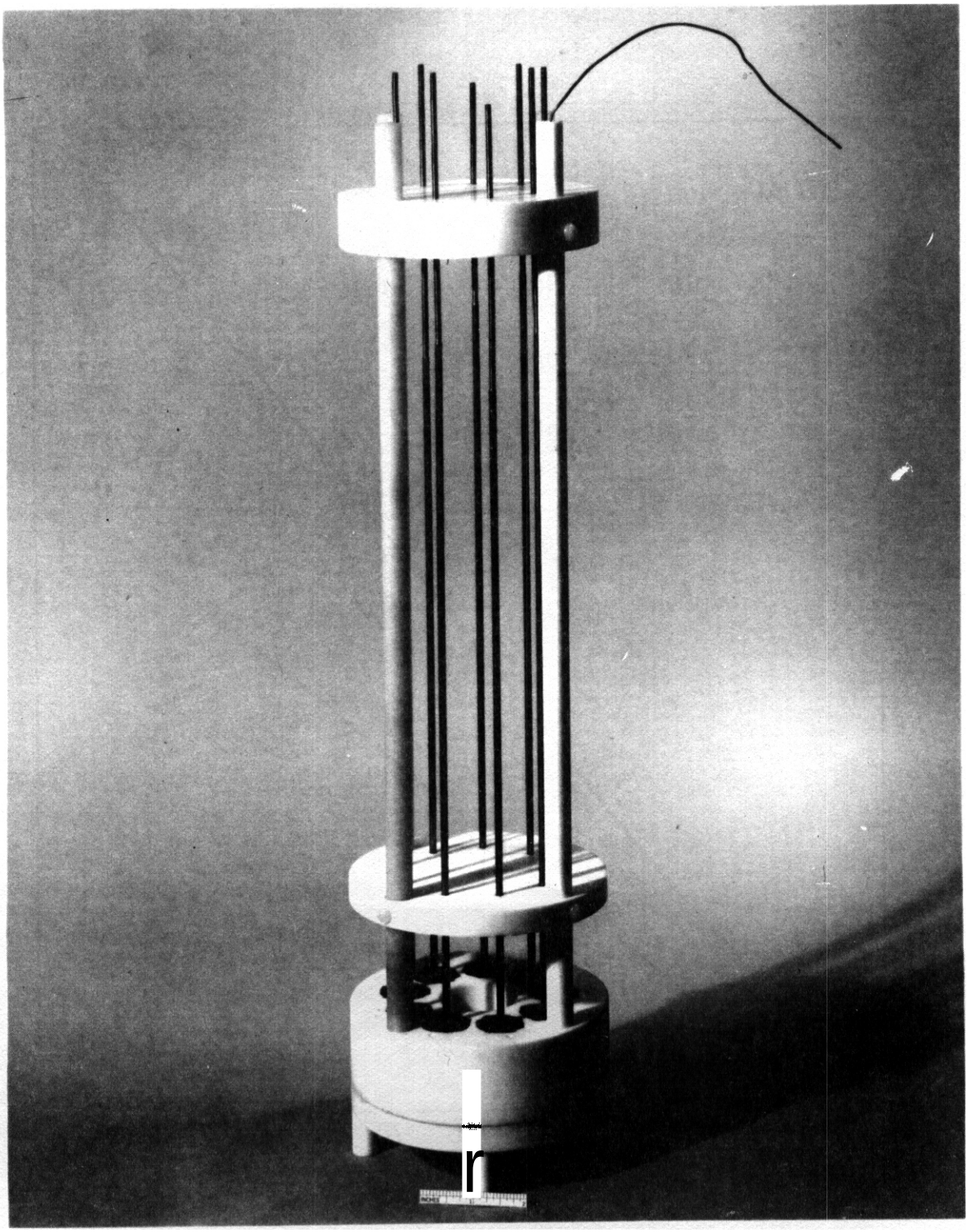

FIGURE 2. **Apparatus Designed for Copper Plating 316 SS/Mo Target Assemblies to Obtain Maximum Thermal Contact Prior to Dual-Ion Bombardment.**

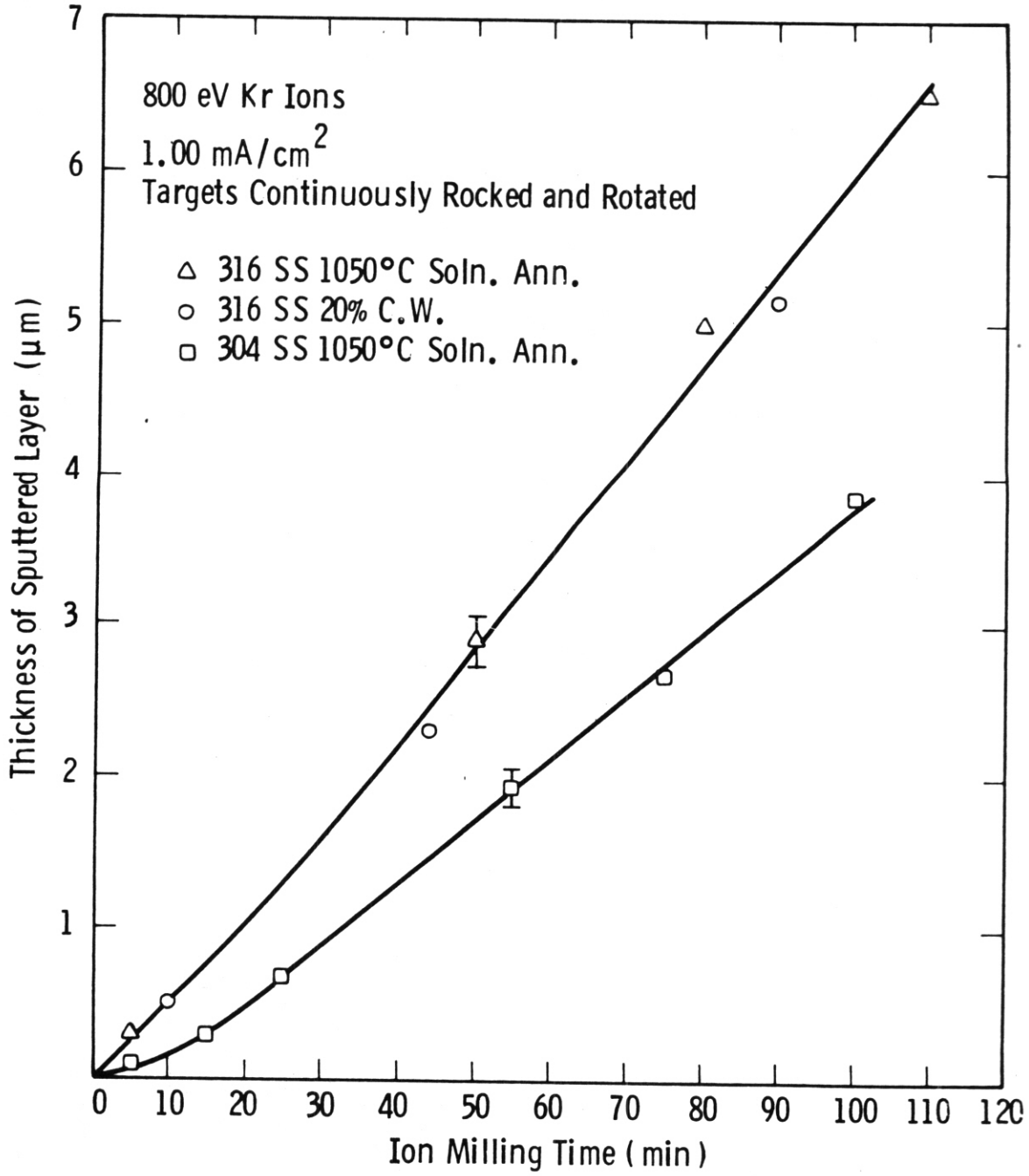

FIGURE 3. Calibration Curves for Ion Milling of 316 SS and 304 SS Targets.

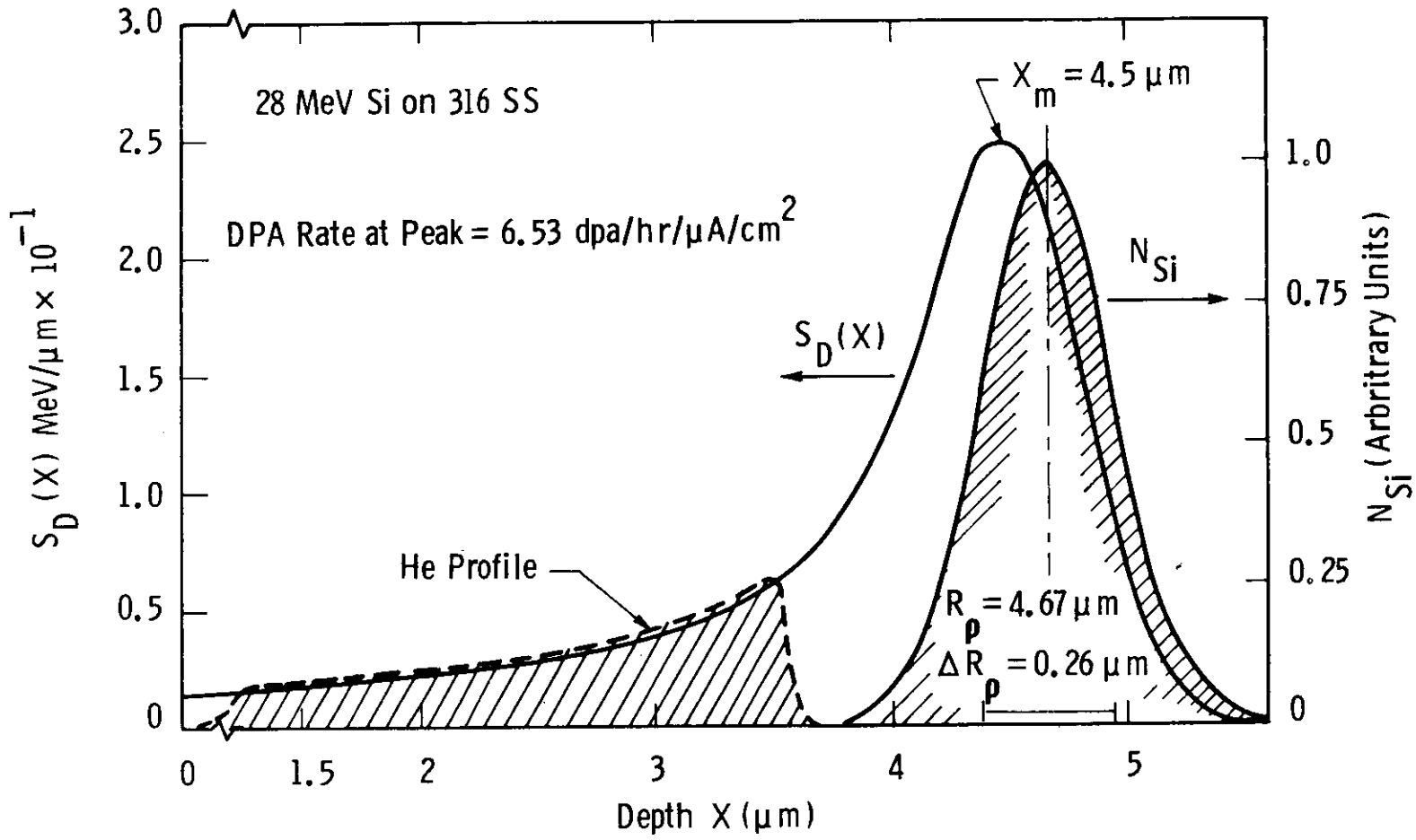

FIGURE 4. Calculated Damage Energy Profile for 28 MeV Si^{+6} Ions in 316 SS and Schematic Concentration Profiles for Implanted Helium and Silicon.

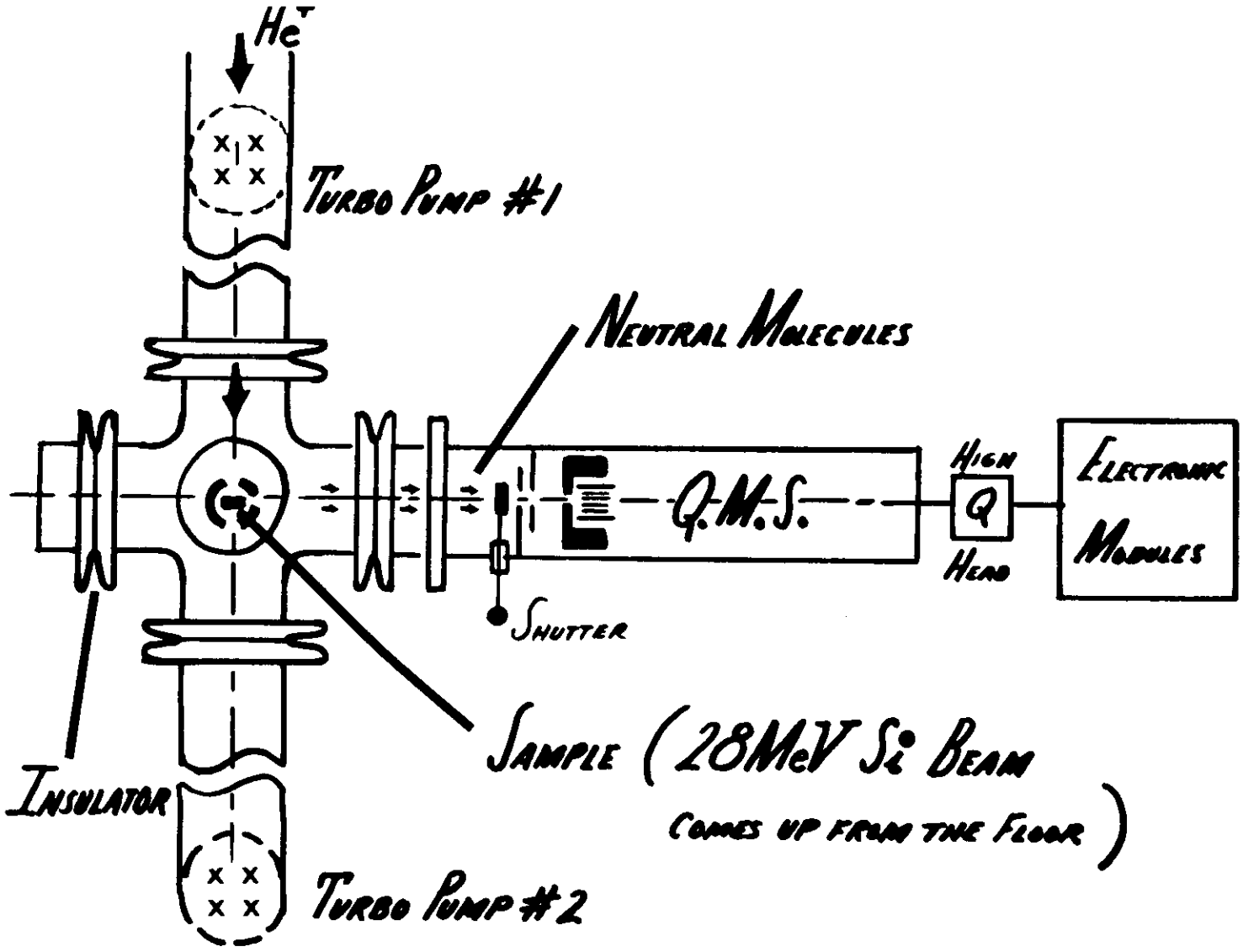

FIGURE 5. Proposed Scheme for a Residual Gas Analysis System Compatible with Dual-Ion Beam Bombardment Requirements.

DISTRIBUTION FUR MFE QUARTERLY REPORTS

UC-20 (117)
UC-20c (78)
APPROVED SPECIAL DISTRIBUTION (48)

Argonne National Laboratory (5)
9700 South Cass Ave.
Argonne, Illinois 60439

L. R. Greenwood
S. D. Harkness
V. H. Maroni
A. Taylor
H. Wiedersich

Atomics International (1)
Component Engineering and Technology Division
North American Rockwell
8900 DeSoto Ave.
Canoga Park, California 91304

D. Kramer

Battelle-Northwest (5)
P. O. Box 999
Richland, Washington 99352

J. L. Brimhall
T. Chikalla
A. B. Johnson
L. C. Schmid
D. Styris

Brookhaven National Laboratory (1)
Associated Universities
Upton, New York 11973

Chairman, Department of Nuclear Energy

Columbia University (1)
Plasma Physics Laboratory
New York, New York 10027

R. A. Gross

Department of Energy (7)
Washington, D.C. 20545

Assistant Director for Materials Technology, RRT
N. A. Davies
J. F. Decker
P. B. Hemmig
K. G. Moses
R. E. Price
F. T. Scott

General Atomic Company (3)
P. O. Box 81608
San Diego, California 92138

C. Baker
G. R. Hopkins
L. Rovner

Lawrence Livermore Laboratory (2)
University of California
P. O. Box 808
Livermore, California 94550

M. W. Guinan
C. M. Logan

Los Alamos Scientific Laboratory (3)
University of California
P. O. Box 1663
Los Alamos, New Mexico 87544

D. J. Dudziak
C. R. Emigh
W. Green

Massachusetts Institute of Technology (1)
Cambridge, Massachusetts 02139

L. Lidsky, Department of Nuclear Engineering

McDonnell-Douglas Astronautics (1)
P. O. Box 516
St. Louis, Missouri 63166

D. Kummer

Mound Laboratory (1)
P. O. Box 32
Miamisburg, Ohio 45342

Manager, Technology Applications and Development

NAVAL RESEARCH LABORATORY (1)
Metallurgy Division, Code 6390
Washington, D.C. 20375

I. Manning

North Carolina State University (1)
Department of Nuclear Engineering
Raleigh, North Carolina 26707

J. R. Beeler, Jr.

Oak Ridge National Laboratory (6)
P. O. Box Y
Oak Ridge, Tennessee 37830

Director, Thermonuclear Division, Bldg. 9201-2
R. J. Colchin, Bldg. 9201-2
W. R. Martin, Bldg. 4500 S
F. G. Perey
M. Roberts, Bldg. 9204-1
C. Weisbin

Plasma Physics Laboratory (3)
Princeton University
Forrestal Campus
Box 451
Princeton, New Jersey 08540

C. Osgood
W. Price
K. Wakefield

Sandia Laboratories (2)
Albuquerque, New Mexico 87115

F. L. Vook (2)

Sandia Laboratories (2)
Livermore, California 94550

W. Bauer (2)

University of Michigan (1)
Nuclear Engineering Department
College of Engineering
Ann Arbor, Michigan 48105

T. Kammash

Westinghouse Electric Corporation (1)
Researcn and Development Center
Beulah Road
Pittsburgh, Pennsylvania 15234

H. R. Holland